Diagnostic Techniques And Instrument Concepts For Probing Transition Region And Coronal Magnetic Fields

A Thesis
Submitted for the Degree of
Doctor of Philosophy (Technology)

Submitted by
RAVEENA KHAN

Department of Applied Optics & Photonics
University of Calcutta

2024

To my family

"There is only one way to learn. It's through action. Everything you need to know you have learned through your journey." — **Paulo Coelho, The Alchemist**

Abstract

Magnetic fields are the primary driver of the plasma thermodynamics in the upper solar atmosphere, especially in the transition region (TR) and the corona. These magnetic fields hold the key to long standing questions in solar physics, such as the problem of coronal heating, the acceleration source of the solar wind, and various eruptive events, thereby influencing the space weather dynamics. However, the lack of vector magnetic field measurements in the TR-corona, has limited our understanding of these physical processes. In this context, extreme-ultraviolet (EUV) and far-ultraviolet (FUV) spectropolarimetry is a potential measurement technique to quantify the TR and coronal magnetic field vector. This thesis is dedicated to finding new diagnostics of the TR and coronal magnetic field vector, exploring suitable instrument concepts and characterizing the instrument prototype in the laboratory as a proof of concept.

Bommier et al. (1981) proposed a method (called the *differential* Hanle effect) to obtain the vector magnetic field information, which utilizes a minimum of two permitted lines with different Hanle sensitivity. This method has been successfully applied to derive the vector magnetic field in prominences, and was further extended to obtain empirical information on the TR fields. The same method can also be used to infer the coronal magnetic fields, prior to which it is necessary that combination of EUV and FUV lines exhibiting varied Hanle sensitivity to the coronal magnetic fields are identified so that any ambiguity can be removed from the derived magnetic field solution. Therefore, in the first study, we identified potential Hanle sensitive lines in the FUV and EUV spectral ranges which exhibit line-formation temperatures typical of the TR and corona. Several EUV lines, with the critical Hanle field ranging from a few milligauss to 200 gauss, were identified in the wavelength range of 100 to 1600 Å.

EUV lines enable both off-limb and on-disk measurements, unlike at visible and IR wavelengths where only coronagraphic (off-limb) observations are possible due to the extremely bright solar disk. On-disk measurements are important to understand the magnetic field stratification in the solar atmosphere. However, there is no spectropolarimeter yet in these spectral ranges to infer the vector magnetic field in the upper atmospheric layers of the Sun. Since transmission optics is not feasible in these wavelengths, several configurations of EUV polarimeter based on highly reflective and

polarizing coatings are explored in the thesis. On the contrary, it is essential to estimate the polarization signals and the signal-to-noise ratio (SNR) required to measure such signals in the wavelength range considered for the instrument design. Hence, the next project of the thesis involved modeling and synthesizing the polarization maps of one of the identified EUV lines, i.e., Ne VIII 770 Å, by utilizing magnetohydrodynamic (MHD) simulation data cubes.

Furthermore, our investigation of various polarimeter configurations revealed that a 3-mirror-based design, using barium fluoride coated mirrors, exhibits enhanced polarizing power and higher throughput in the wavelength range of 740 to 800 Å. As part of our efforts, an EUV spectropolarimeter has been designed using ZEMAX targeting the same wavelength range, with Ne VIII 770 Å as the central wavelength. From the previous study of Ne VIII 770 Å (one of the brightest EUV lines), the Stokes L/I (where $L = \sqrt{Q^2 + U^2}$) is estimated to be in the orders of 1×10^{-4} at the solar limb region. Therefore, detection of polarization sensitivity in these levels is an essential requirement which has driven the design of the instrument. Simultaneously, an in-house prototype of the 3-mirror polarimeter has been developed, and its preliminary testing has been conducted in the laboratory. Due to lack of facilities for fabrication and testing in the EUV, we conducted the initial characterization at a visible wavelength of 700 nm.

Contents

List of Publications

Refereed Journal Articles (related to this thesis)

1. Spectral Lines in FUV and EUV for Diagnosing Coronal Magnetic Field
   Raveena Khan, K. Nagaraju, 2022, **Solar Physics**, 297, 96.

2. Extreme-ultraviolet Polarimetric Diagnostics of the Solar Corona: The Hanle Effect of Ne VIII 770 Å
   Raveena Khan, Sarah E. Gibson, Roberto Casini, and K. Nagaraju, 2024, **The Astrophysical Journal**, 971, 27.

3. Design requirements of a Spectropolarimeter for solar Extreme-ultraviolet Observations and characterization of K-mirror based on Brewster's angle
   Raveena Khan, Radhika Dharmadhikari, Harsh Mathur, K. Nagaraju, Sinchana R. Jain, D.V.S. Phanindra, and K. Sagayanathan, **Applied Optics**, (under revision).

Conference Proceedings

1. Design concepts of EUV polarimeter
   Raveena Khan, K. Nagaraju and DVS Phanindra, 2023, **SPIE Proceedings, Optics for EUV, X-ray, and Gamma-ray astronomy** XI, Vol. 12679, pp. 161–167.

Presentations

Oral

1. **UV polarimetry - A probe to measure the coronal magnetic field vector** at the Foundation Day Symposium of the Indian Institute of Astrophysics from 31 March – 01 April, 2022.

2. **Design concepts of EUV polarimeter** at the SPIE Optics & Photonics Conference, San Diego, USA from 20 – 24 August, 2023.

Posters

1. **Potential UV spectral lines for coronal magnetic field measurements** at the 40th Meeting of the Astronomical Society of India (online) from 25 – 29 March, 2022.

2. **EUV polarimeter: To explore the unchartered emissions of the Sun** at the NASA's "Living with a Star" Heliophysics Summer School, Boulder, USA from 07 – 11 August, 2023.

3. **FORWARD modeling of Ne VIII line as a coronal magnetic field diagnostic** at the 42nd Meeting of the Astronomical Society of India hosted jointly by IISC, ISRO and JNP, Bengaluru, India from 31 January – 04 February, 2024.

4. **Optical design of an extreme-ultraviolet (EUV) spectropolarimeter for coronal observations of the Sun** at the National Space Science Symposium, Goa from 26 February – 01 March, 2024

List of Figures

List of Tables

List of Abbreviations

AR Active Region

CH Coronal Hole

ChroMag Chromospheric and Prominence Magnetometer

CME Coronal Mass Ejection

CMOS Complementary Metal-Oxide Semiconductor

COMP COronal Multi-channel Polarimeter

COSMO COronal Solar Magnetism Observatory

CR Carrington Rotation

DKIST Daniel K. Inouye Solar Telescope

EIS Extreme-ultraviolet Imaging Spectrometer

ESA European Space Agency

EUNIS Extreme Ultraviolet Normal-Incidence Spectrograph

EUV Extreme UltraViolet

EUVI Extreme UltraViolet Imager

FOV Field of view

FUV Far UltraViolet

FWHM Full Width at Half Maximum

GOES Geostationary Operational Environmental Satellite

GPS Global Positioning System

IR InfraRed

KCor K-Coronagraph

L1 Sun–Earth Lagrange point 1

LC Large Coronagraph

LOS Line Of Sight

LSF Line Spread Function

LUVOIR Large UltraViolet Optical InfraRed surveyor

MAS Magnetohydrodynamic Algorithm outside a Sphere

MCDHF MultiConfiguration Dirac-Hartree-Fock

MHD Magnetohydrodynamics

MIT Magnetic-field Induced Transition

NASA National Aeronautics and Space Administration

PCIDAQ Peripheral Component Interconnect Data AcQuisition

PFSS Potential Field Source Surface

POS Plane Of Sky

PSI Predictive Science Incorporation

QS Quiet Sun

SC Solar Cycle

SOHO SOlar and Heliospheric Observatory

SUMER Solar Ultraviolet Measurements of Emitted Radiation

SNR Signal to Noise Ratio

TR Transition region

UCOMP Upgraded COronal Multi-channel Polarimeter

VELC Visible Emission Line Coronagraph

Chapter 1
Introduction

"Wisdom is to live in tune with the mode of the changing world." — Thiruvalluvar

The Sun has one of the most complex magnetic systems, but at the same time it is also the most accessible star for studying and modeling through spatially resolved observations from both space-based and ground-based solar telescopes. Its proximity, at just 149.6 million kilometers away, makes the Sun a comprehensive reference for understanding the luminosity, radius, temperature, and other characteristics of stars throughout the universe. As the primary source of light and heat for Earth, the Sun plays a crucial role in driving the complex climate dynamics of our planetary system.

The Sun is composed of several layers, from its interior to its upper atmosphere (Figure 1.1). The visible surface of the Sun, known as the photosphere, has an average temperature of approximately 5700 K. There are certain locations on the photosphere where the magnetic field is concentrated and the temperature drops to around 3000-4000 K. Such regions appear dark, known as sunspots, as shown in Figures 1.1 and 1.3. Above the photosphere lies the chromosphere, where temperature reaches about 20,000 K and different features that could be observed in this layer are plages and spicules. Beyond the chromosphere is a thin transition region where the temperature rapidly increases to 10^6 K and the electron density sharply decreases from 10^{11} cm^{-3} to 10^9 cm^{-3}. This abrupt change in temperature and density is crucial for understanding the coronal heating problem. Several jet-like features, including transition region (TR) jets (Tian *et al.*, 2014), are observed in this region. Following the transition region is the extensive and outermost layer called the corona (corona means "crown"), where temperature exceeds 10^6 K. The corona exhibits various features such as streamers, coronal loops and coronal holes, observable across different wavelengths. During a total solar eclipse, the crown-like shape of the corona is highly conspicuous from Earth.

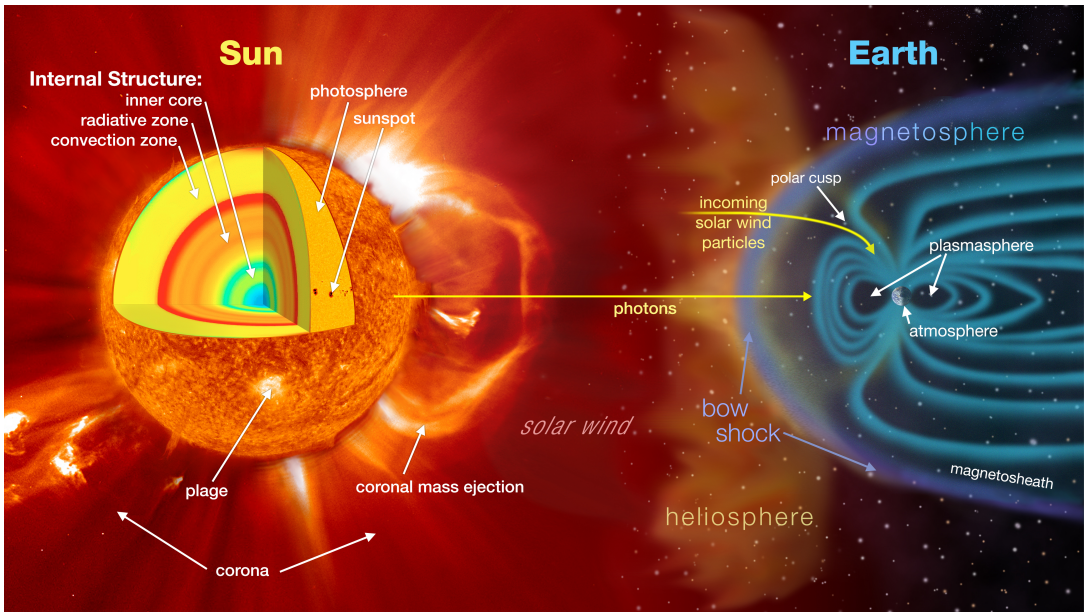

Figure 1.1: Interaction between the Sun and the Earth and its effects on the geospace weather (Courtesy: https://svs.gsfc.nasa.gov/30481).

1.1 Significance of Upper Solar Atmosphere and its magnetism

The magnetism of the upper atmospheric layers of the Sun, especially the transition region (TR) and the corona, is a key ingredient to understand the various fundamental plasma processes occurring in these layers. Some of these processes include the coronal heating, the acceleration of energetic particles, and the formation and evolution of coronal features such as coronal loops and streamers, along with their thermal and magnetohydrodynamic (MHD) characteristics. The dominance of the magnetic field in these layers is due to the rapid decrease in plasma β, which is defined as the ratio of kinetic pressure to magnetic pressure, from the photosphere to the corona. With low plasma β, the equilibrium field becomes force-free in the TR and corona, and magnetic pressure dominates over gas pressure (Priest and Hood, 1991). This magnetic dominance is crucial for the stability and dynamics of the solar atmosphere, influencing events from small-scale magnetic reconnection events to large-scale coronal mass ejections (CMEs).

The Sun is currently undergoing the phase of solar maxima and therefore dark regions with strong magnetic fields in the order of kilogauss, called sunspots, are very prominent on the surface of the Sun. Giant explosions of energy and particles, such as solar flares and CMEs, are commonly detected during this phase. These highly energetic particles interact with Earth's outer atmosphere, resulting in the formation of beautiful northern lights, also known as aurora borealis, as pictured in Figure

Figure 1.2: *Top panel:* Aurora borealis captured over the Eielson Air Force Base, Bear Lake, Alaska on January 18, 2005 (Courtesy: Wikipedia). *Bottom panel:* Red auroral arc captured from the Tashi Choeling Gompa nunnery in Hanle, Ladakh on May 10, 2024 (Image credit: Wangchuk Namgyal, Stanzin Norlha and Stanzin Norboo)*.

1.2. Usually, high-latitude locations, like Norway and Iceland, witness these aurorae. However, there was a rare sighting of red auroral arc on the night of May 10, 2024 at Hanle, Ladakh, as shown in the bottom panel* of Figure 1.2. This phenomenon was triggered by an extreme solar flare from the active sunspot region AR 13664A. A similar aurora was visible at the Indian Astronomical Observatory in Hanle around 23 April 2023, caused by a powerful CME propagating towards Earth. These energetic events are strongly driven by the TR and coronal magnetic fields, which also affect the space weather (Figure 1.1) and can interfere with satellite electronics, radio communications, global positioning system (GPS) signals, spacecraft orbits, and

*https://nature.com/articles/d44151-024-00068-w?utm_campaign=engagement&utm_content=1715785972&utm_medium=social&utm_source=twitter&s=03

even electrical power grids on Earth. Such severe consequences make it extremely important to study and continuously monitor the Sun.

Routine measurements of the magnetic field vector and the study of its dynamic evolution in the solar atmosphere are highly emphasized to understand the exact role it plays in driving the energetic solar events. Moreover, understanding the interaction between the coronal magnetic fields and the solar wind provides insights into the behavior of other stellar atmospheres and the effect of their magnetic fields on planetary environments.

1.2 Brief history on measurements of magnetic field at the upper solar atmosphere

The first attempt to predict the TR and coronal magnetic fields were based on the extrapolation of the observed photospheric magnetic fields. In the recent years, significant progress has been witnessed in the so-called potential field source surface (PFSS) models, originally proposed by Altschuler and Newkirk (1969) and Schatten, Wilcox, and Ness (1969). More sophisticated models, known as magnetohydrodyanmic (MHD) models (Mikić *et al.*, 1999; Lionello, Linker, and Mikić, 2001), have been developed and continuously improved to better comprehend the physics of the magnetized coronal plasma. While our understanding of the TR and coronal magnetic fields has greatly enhanced over the last couple of decades with the help of these powerful models, these approaches are, however, limited due to absence of routine magnetic field measurements in the TR and corona (Mackay and Yeates, 2012; Wiegelmann, Petrie, and Riley, 2017, and references therein). Regular observations of the vector magnetic fields are required not only in the strong field regions, but also in the weak field ones, so that more constraints can be imposed on the input data of bipole emergences which drive these models.

The technique of microwave gyroresonance magnetometry has been used to investigate magnetic field strength (in the order of a few hundred gauss) in the lower corona over active regions (Nitta *et al.*, 1991; Schmelz *et al.*, 1994; Gary and Hurford, 1994; Bogod and Yasnov, 2016). Faraday rotation measurements of the polarized emission from radio sources have been used to derive the mean coronal field strength in the range of several tens of milligauss at and above 5 $R_\odot$ (Patzold *et al.*, 1987; Sakurai and Spangler, 1994; Ingleby, Spangler, and Whiting, 2007; Kooi *et al.*, 2021). Gopalswamy *et al.* (2012) measured coronal field strength (1.3 to 1.5 G) over the distance of 1.2 to 1.5 $R_\odot$ using extreme-ultraviolet (EUV) observations of a CME flux rope and radio dynamic spectra of the associated type II radio burst in tandem. The spectroscopic observations of standing slow-mode MHD waves captured by the Solar Ultraviolet Measurements of Emitted Radiation (SUMER), aboard SOlar and Heliospheric Observatory (SOHO) satellite, were analyzed to determine the magnetic field strengths

of 12 to 51 G in the coronal loops (Wang, Innes, and Qiu, 2007). Recently, Yang *et al.* (2020a,b) applied the technique of magnetoseismology to the transverse MHD waves observed with the Coronal Multi-channel Polarimeter (CoMP; Tomczyk *et al.* (2008)) (Liu *et al.*, 2015; Tomczyk *et al.*, 2007) and provided the synoptic maps of the plane-of-sky (POS) component of the coronal magnetic field. Another recent spectroscopic technique, the so-called Magnetic-field Induced Transition (MIT; Grumer *et al.*, 2014), has been demonstrated to explain the potential of MIT lines in the measurement of coronal magnetic field (Li *et al.*, 2015, 2016; Landi *et al.*, 2020, 2021; Li *et al.*, 2021). More recently, Boe, Habbal, and Druckmüller (2020) quantified the magnetic field topology of the solar corona using white-light observations during total solar eclipses spanning over two solar cycles.

At the optical, infrared (IR) and UV spectral range, the Zeeman and the Hanle effects have been utilized to derive the TR and coronal magnetic fields. Theoretical studies have been carried out to model and calculate the linear polarization signals produced by scattering processes in the hydrogen Lyman-α line at 1215.67 Å, and interpret its polarization sensitivity to the TR magnetic fields via the Hanle effect (Trujillo Bueno, Štěpán, and Casini, 2011; Trujillo Bueno, Štěpán, and Belluzzi, 2012; Štěpán *et al.*, 2012). Similarly, Zhao *et al.* (2019, 2021) examined the linear polarization of Lyman-α in the presence of both the Hanle effect and other symmetry breaking processes. Raouafi *et al.* (2016) and Hebbur Dayananda *et al.* (2021) have used 3D coronal MHD models to investigate the linear polarization signals in UV and IR lines for probing the magnetism at the off-limb corona. All these theoretical predictions emphasize on the measurement and interpretation of the polarization induced by certain physical mechanisms in spectral lines which can help in quantifying the vector magnetic field in the TR and corona.

However, there have been very few polarimetric observations aimed at determining the magnetic fields in these solar atmospheric layers. Lin et al. (2000, 2004) conducted pioneering work by measuring the line-of-sight (LOS) component of the coronal magnetic field. They utilized observations of the Zeeman splitting in the Fe XIII line at 10747 Å and inferred field strengths of 4 to 33 G at heights of 0.10 to 0.15 $R_\odot$ above active regions. Raouafi et al. (2002) made a significant contribution by attempting, for the first time, to measure the coronal magnetic field using the linear polarization measurement of the O VI line at 1032 Å due to the Hanle effect. They derived a field strength of about 3 G above a coronal hole, demonstrating the potential of the Hanle effect in probing coronal magnetic fields in regions with weak magnetic fields. The Chromospheric Lyman-Alpha Spectro-Polarimeter (CLASP) has also made notable advancements in this field. The spectropolarimetric observations by CLASP have provided a better understanding of the geometrical complexity and dynamics of the upper chromosphere and TR of the Sun (Kano *et al.*, 2017). These observations have been instrumental in revealing the intricate magnetic structures and their evo-

lution in these layers, contributing to our overall knowledge of solar magnetic fields. Despite these advancements, the scarcity of routine polarimetric observations limits our understanding of the magnetic phenomena occurring in the solar atmosphere, and demands for future missions and instruments addressing this gap.

1.3 Physical mechanisms behind spectral line polarization

The state of polarization of an electromagnetic radiation beam can be conveniently characterized by four observables, namely Stokes parameters (I, Q, U, V), which can be measured by telescopes equipped with a polarimeter, which is an instrument designed to analyze the polarization state of light. Stokes I represents the total intensity of the beam, providing a measure of the overall brightness. Stokes Q represents the intensity difference between linear polarization along the principal axes (i.e., vertical and horizontal), and Stokes U represents the intensity difference between linear polarization at $+45°$ and $-45°$ to the principal axes. Stokes Q, U together provide a complete description of the linear polarization state. Stokes V represents the intensity difference between right-handed and left-handed circular polarization, offering insights into the circular polarization component of the light (Born and Wolf, 1999). It is important to note that the reference axis must be chosen first for defining the Stokes Q and U parameters. The reference axis is usually selected as the direction where $Q > 0$ in the plane perpendicular to the direction of propagation.

There are various physical mechanisms that can either induce or modify the polarization signatures in the spectral lines originating from different layers of the solar atmosphere. By measuring and interpreting the polarization introduced by these mechanisms in the spectral line radiation, quantitative information on both the strength and orientation of the ambient magnetic field can be derived.

1.3.1 The Zeeman effect

The Zeeman effect refers to the splitting of the energy levels in the presence of external magnetic field which produces characteristic polarization depending on the orientation of vector magnetic field with respect to the observer's LOS. This effect was first discovered by the Dutch physicist Prof. Pieter Zeeman in 1896 when he placed an oxy-hydrogen flame between the poles of an electromagnet and introduced a filament of asbestos soaked in common salt into the flame (Zeeman, 1897). When the electromagnet was switched on, he observed that the two D-lines of the sodium spectrum were clearly widened. Zeeman communicated this idea to Prof. H.A. Lorentz, who developed a theory of electromagnetic phenomena, which explained that the light emitted from the edges of the widened lines would be circularly polarized (plane polarized) when the observer's LOS is parallel (perpendicular) to the lines of force. Thus, it was

the discovery of the *Zeeman effect* for which he won the Nobel prize in Physics along with Prof. Lorentz in 1902.

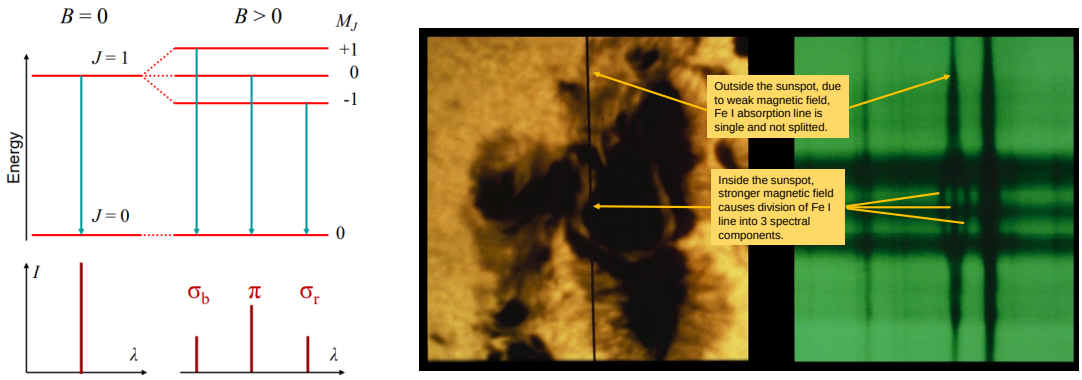

(a) (b)

Figure 1.3: Left image (a) illustrates the Zeeman splitting in form of different energy levels and the allowed transitions between them. Right image (b): The left panel shows a sunspot in white light with the vertical black line locating the slit for the spectrograph which took the spectrum shown in the right panel. The division of Fe I line, at 5250 Å, into three components ($\Delta M = 0$ transition forms π, while $\Delta M = \pm 1$ transitions form σ_b, σ_r components) is a clear demonstration of the Zeeman effect. *Adapted from* https://noirlab.edu/public/images/noao-6031/.

The Zeeman effect was first studied on the Sun in 1908 by an American astrophysicist, Prof. George Ellery Hale, who analyzed the sunspot spectrum for evidences of line doublets and line broadening, and explained its difference from the ordinary solar spectrum. Such doublets were first observed by Professors Young and T. Reed in 1892, and later observed again by Prof. Walter M. Mitchell who described these doublets as "reversals" (Mitchell, 1904). But a detailed explanation of the occurrence of these line doublets in the sunspot spectra was given by Prof. Hale which led to the discovery of the existence of strong magnetic fields on the Sun (Hale, 1908). Gradually, this effect has formed the basis of development of vector magnetograms to reliably determine the magnetic field in the photosphere and the chromosphere (Stenflo, 2017, and references therein).

In the presence of a suitable magnetic field, each energy level with total angular momentum J splits into $(2J + 1)$ sublevels, the splitting being proportional to the level's Landé factor, g_J, and to the field strength, B (expressed in gauss). This level splitting can be represented in the form of different energy levels as shown in Figure 1.3(a). Therefore, a spectral line transition between a lower level (J_l, g_l) and an upper level (J_u, g_u) consists of several spectral components. In particular, a line transition between $J_l = 0$ and $J_u = 1$ levels has three components: one π component (corresponding to $\Delta M = 0$), one σ_r (corresponding to $\Delta M = -1$), and one σ_b

component (corresponding to $\Delta M = +1$). An example of such wavelength shifts due to the Zeeman effect is shown in Figure 1.3(b) where the Fe I line at 5250 Å splits into three components in the strong-field sunspot region.

1.3.2 Anisotropic radiation pumping

The amplitude of Zeeman polarization signals in the upper solar atmosphere (TR and corona) is very weak because the Zeeman splitting is only a small fraction of the spectral line-width. Stokes V amplitude (due to longitudinal Zeeman effect) scales with the ratio, R, between the Zeeman splitting and the Doppler line-width, whereas Stokes Q and U (produced by the transverse Zeeman effect) scale with R^2. Here, $R \propto \lambda B/\sqrt{T}$, with λ being the spectral line wavelength in Å, B the magnetic field strength in G and T the kinetic temperature in K (see Landi Degl'Innocenti and Landolfi (2004)). Owing to the dependence on wavelength and temperature, this ratio is very small for the spectral lines originating from the weakly magnetized plasma of the TR and corona with temperatures exceeding 10^5 K.

Nevertheless, there is another mechanism which can introduce spectral line polarization in the solar atmosphere. The anisotropic illumination of a gas of atoms induces atomic-level polarization (i.e., atomic alignment and atomic orientation and, moreover, quantum coherences may appear between the magnetic sublevels of each J-level or, among the sublevels belonging to different J-levels) as illustrated in Figure 1.4. Atomic alignment refers to the condition when the Zeeman substates of levels with $J \geq 1$ are unevenly populated, such that the total population of substates with different values of $|M|$ are different. Atomic orientation refers to the condition when, for a given value of $|M|$, the substates labeled as -M and +M have unequal populations. Hence, the absorption of anisotropic radiation can generate linear polarization in the spectral line emission considered (Trujillo Bueno, 2001) without the presence of a magnetic field, provided the depolarizing collisional rates are sufficiently low.

1.3.3 The Hanle effect

The Hanle effect produces a modification of the atomic-level polarization (and of the emergent Stokes Q and U profiles of the spectral line radiation) due to the local magnetic field inclined with respect to the symmetry axis of the pumping radiation field. The emergent linear polarization is sensitive to magnetic field strengths approximately between $0.1B_H$ and $5B_H$ (Trujillo Bueno, 2014), where $B_H = 1.137 \times 10^{-7}/(\tau_{life} g_J)$ with τ_{life} and g_J being, respectively, the lifetime (in seconds) and the Landé factor of either the upper or the lower level of the line transition considered. B_H is termed as the *critical* Hanle field (measured in gauss) for which the Zeeman splitting is comparable with the natural width of the energy level under consideration, such that it is sufficient to create a measurable change in the atomic-level polarization. Above the limit of $5B_H$, the magnetic sublevels are well separated and therefore, the quantum

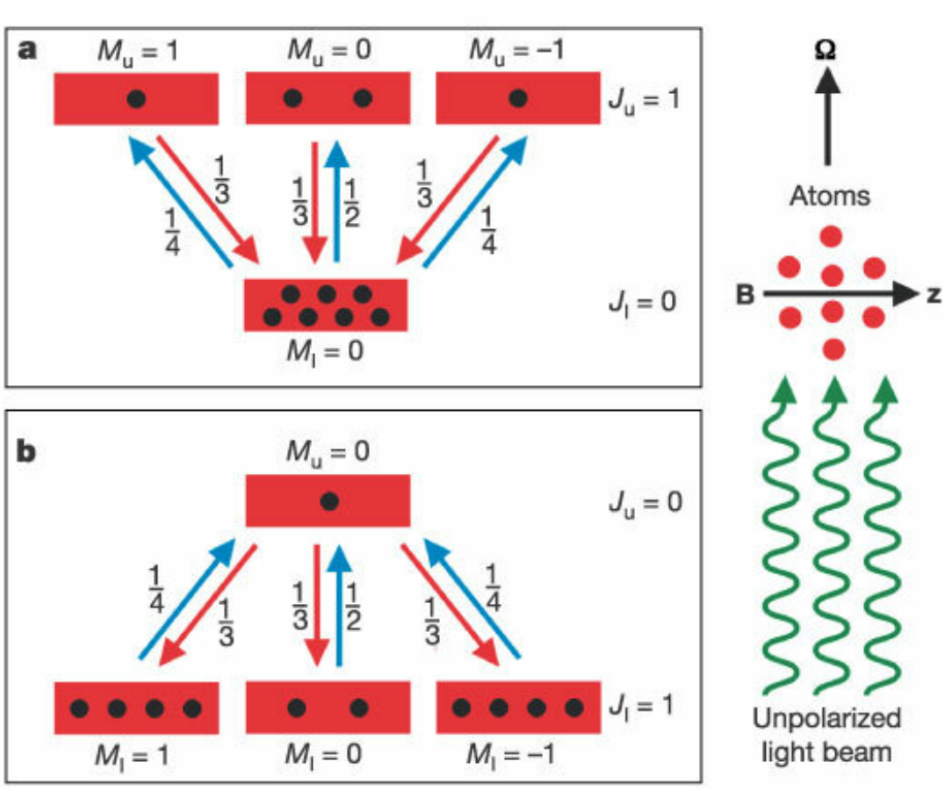

Figure 1.4: Graphical representation of anisotropic radiation pumping and the Hanle effect. Image credit: Trujillo Bueno *et al.* (2002).

coherence between them gets nullified due to which the (Hanle regime) linear polarization is no longer sensitive to the field strengths, but only to the field orientation in the POS (also called the field azimuth). This regime of the Hanle effect is defined as the *saturated* Hanle regime. This saturation occurs because the Larmor precession frequency of the atoms or ions in the magnetic field becomes much larger than the inverse of the lifetime (τ_{life}) of the excited state. By estimating B_H for several spectral lines originating from weak magnetic field regions, it can be theoretically established whether the Hanle effect is capable of diagnosing these weak magnetic fields, where the Zeeman effect is not practically useful as a stand-alone technique. This makes the Hanle effect a powerful tool for probing magnetic fields in various astrophysical environments, particularly in regions where the magnetic field strength is below the detection threshold of the Zeeman effect.

1.4 Motivation

The lack of vector magnetic field measurements in the upper solar atmosphere, i.e., the TR and the corona, has limited our understanding of the physical processes occurring in these layers, such as the million-degree energization of the solar corona,

the solar wind acceleration, the formation and evolution of eruptive events (for e.g., solar flares and CMEs), which affect the near-Earth space weather. Spectropolarimetry is a potential measurement technique to quantify the TR and coronal magnetic field vector because the magnetic field information of these layers remains embedded in the emergent spectral line profiles. Hitherto, from the measurements of circular polarization (Stokes V/I) of the IR line Fe XIII at 10747 Å due to the longitudinal Zeeman effect, Lin et al. (2000, 2004) have inferred coronal magnetic field strengths of about 4 to 33 G above active regions. However, the Stokes V signal is very weak ($\sim 10^{-4}$) and difficult to measure on a daily basis. Owing to the wavelength scaling of Stokes V/I signal, its amplitude is even smaller at FUV and EUV wavelengths. Moreover, the linear polarization signal of forbidden lines, such as Fe XIII at 10747 Å, can constrain only the field azimuth (Casini and Judge, 1999) through the saturated Hanle effect.

For permitted lines, such as O VI at 1032 Å, which fall within the regime of the unsaturated Hanle effect for the field strengths expected in the TR and corona, the linear polarization is, in theory, sensitive to both the field strength and the field direction. Therefore, the unsaturated Hanle effect offers a clear advantage as the vector field diagnostic of the TR and corona. A single spectropolarimetric observation of the linear polarization of O VI at 1032 Å, which was performed by rotating the SOHO satellite, helped in deriving the coronal magnetic field by exploiting the instrumental polarization and employing the Hanle effect (Raouafi, Lemaire, and Sahal-Bréchot, 1999; Raouafi, Sahal-Bréchot, and Lemaire, 2002; Raouafi *et al.*, 2002). Such an impromptu and unoptimized measurement of resonance line polarization demonstrates that UV spectropolarimeters onboard space telescopes are capable of providing critical magnetic field measurements in the TR and corona. Further, EUV and FUV lines enable both off-limb and on-disk measurements, unlike at visible and IR wavelengths where only coronagraphic (off-limb) observations are possible. On-disk measurements are important to understand the magnetic field stratification in the solar atmosphere.

Bommier, Sahal-Bréchot, and Leroy (1981) proposed a method (the so-called *differential* Hanle effect) which utilizes a minimum of two resonance lines with different Hanle sensitivity to obtain the vector magnetic field information. This method has successfully been applied to derive the vector magnetic field in prominences (House and Smartt, 1982; Bommier, Leroy, and Sahal-Bréchot, 2021), and has also been extended to obtain empirical information on the TR fields (Trujillo Bueno, Štěpán, and Belluzzi, 2012). In a similar way, the differential Hanle diagnostic method can be used to study the coronal fields, prior to which it is necessary that combination of EUV and FUV lines exhibiting varied Hanle sensitivity to the TR and coronal magnetic fields are identified so that any redundancy can be removed from the derived magnetic field solution.

Being motivated by the previous findings, our first project involved the identifi-

cation of potential Hanle sensitive lines in the FUV and EUV spectral ranges which exhibit line-formation temperatures typical of the TR-corona (Khan and Nagaraju, 2022). During this project, it was found that the spectral atlas of the solar corona (Curdt, Landi, and Feldman, 2004) comprises a rich treasure of bright FUV and EUV emission lines between 670 Å and 1609 Å. Among them, several EUV lines were identified with the critical Hanle field ranging from a few milligauss to 200 gauss.

However, there is no spectropolarimeter yet in these spectral ranges to infer the vector magnetic field in the upper atmospheric layers of the Sun. Since transmission optics is not feasible in these wavelengths, due to complete absorption by any known material, highly reflective and polarizing coatings are required whose optical properties should be well known. As a result, several configurations of EUV polarimeter with suitable coatings were explored in another project, in terms of their throughput and polarizing power (Khan, Nagaraju, and Phanindra, 2023).

On the contrary, it is essential to estimate the polarization signals and the signal-to-noise ratio (SNR) required to measure such signals in the wavelength range considered for the instrument design. Hence, the next project of the thesis involved modeling and synthesizing the polarization maps of one of the identified EUV lines, i.e., Ne VIII 770 Å, by utilizing magnetohydrodynamic (MHD) simulation data cubes (Khan *et al.*, 2024). A fairly recent work by Raouafi *et al.* (2016) used a three-dimensional MHD model to derive the Hanle regime polarization signals at the solar corona (off-limb) in the FUV (H I Lyman-α) and the IR (He I 10830 Å) lines. Hebbur Dayananda *et al.* (2021) utilized 3D coronal MHD models to investigate the linear polarization signals in the FUV (H I Ly-α at 1215 Å) and the EUV (He II Ly-α at 304 Å) lines within 0.5 $R_\odot$ above the Sun's visible limb. All these diagnostics considered a coronagraph instrument to detect the off-limb coronal signal and its polarization unhindered by the disk radiation. This is the first time when we have utilized MHD models to estimate the polarization signals of EUV coronal emission lines observed directly on the disk of the Sun. By analyzing the Stokes parameters, we estimated that the Stokes L/I (where $L = \sqrt{Q^2 + U^2}$) of Ne VIII 770 Å (one of the brightest EUV lines) reaches orders of around 1×10^{-4} at the solar limb region.

Furthermore, our investigation of various polarimeter configurations (Khan, Nagaraju, and Phanindra, 2023) revealed that a 3-mirror-based design, using barium fluoride coated mirrors, exhibits enhanced polarizing power and higher throughput in the wavelength range of 740 to 800 Å. As part of our efforts, an EUV spectropolarimeter has been designed using ZEMAX targeting the same wavelength range, with Ne VIII 770 Å as the central wavelength. Since the polarization signals are in the orders of 1×10^{-4}, detection of polarization sensitivity in these levels is an essential requirement which has driven the design of the instrument. Simultaneously, an in-house prototype of the 3-mirror polarimeter has been developed, and its preliminary testing has been conducted in the laboratory at visible wavelength (Khan *et al.*, under review).

1.5 Outline of the Thesis

This thesis aims at finding new diagnostics of probing the weak magnetic fields at the TR and corona. It also encompasses the study of suitable coating materials and the development of a suitable instrument for preliminary testing in the laboratory. This thesis is structured as follows: In Chapter 2, we have identified a list of potential Hanle sensitive lines in the EUV spectral range which can be used for probing the weak magnetic fields of the TR and corona. Few Hanle saturated lines in FUV have also been explored with the intent of constraining the LOS component of the magnetic field due to longitudinal Zeeman effect. Chapter 3 describes the synthesis of polarization maps at Ne VIII 770 Å to study the variation of its polarization signatures during different phases of the solar cycle. This study also helped us to determine the expected Hanle polarization signals which drives the design of a suitable instrument. In Chapter 4, the design of an EUV spectropolarimeter using ZEMAX has been presented based on reflective components. Various possibilities of achieving the required SNR and polarization sensitivity levels, along with the associated limitations, have been explored in this chapter. Chapter 5 discusses the development and characterization of a prototype polarimeter based on reflective aluminium mirrors. The preliminary testing has been done at the visible wavelength of 700 nm. Finally Chapter 6 summarizes the thesis by outlining the conclusions drawn from all the studies presented. This chapter also highlights the novel aspects of these studies and discusses the future prospects.

Chapter 2
Identification of Hanle sensitive lines in EUV and FUV

Spectral lines in FUV and EUV for diagnosing coronal magnetic field
Raveena Khan, K. Nagaraju, 2022, **Solar Physics**, 297, 96.

2.1 Introduction

When an atom in the corona or the transition region is illuminated by the incoming anisotropic radiation from the underlying atmospheric layers of the Sun, in the absence of magnetic field, the scattered radiation from the atom is linearly polarized in a direction perpendicular to the scattering plane, and the degree of polarization depends on the scattering geometry, the height of the atom from the origin of the incident radiation and also on the polarizability coefficient of the atomic levels of the line transition considered. In the presence of a weak magnetic field, such that the Larmor frequency (directly related to magnetic field strength B as $\omega_B = \frac{\mu_B}{\hbar} B, \mu_B$ is Bohr magneton and $\hbar$ is the reduced Planck constant) is comparable to the Einstein-A coefficient of the upper level of the atomic transition considered, there is modification in the degree and orientation of the observed linear polarization which depends on the strength and direction of the local magnetic field vector. This effect is referred to as the *critical* Hanle effect (Mitchell, Zemansky, and Keenan, 1934; Raouafi, 2002; Landi Degl'Innocenti and Landolfi, 2004). If the magnetic field is stronger such that the Larmor frequency is much higher than the lifetime of the excited state, the change in the degree and orientation of the linear polarization depends only on the direction of the magnetic field vector, but not on its strength. This regime is described as the saturated Hanle effect (House, 1977; Casini and Judge, 1999; Lin, Penn, and Tomczyk, 2000).

At the photosphere, routine magnetic field measurements are being performed with both high and moderate spatial resolution (Lagg *et al.*, 2017) and quite recently, sig-

nificant progress has been made with chromospheric magnetic field measurements as well (Trujillo Bueno, 2014; Lagg *et al.*, 2017; Ishikawa *et al.*, 2021). On the other hand, magnetic field measurements at the TR and corona are still sporadic. Confirmed detection of Stokes V signal through Zeeman effect in the forbidden line due to Fe XIII at 10747 Å was reported by Lin, Penn, and Tomczyk (2000) and Lin, Kuhn, and Coulter (2004). Raouafi, Lemaire, and Sahal-Bréchot (1999) reported the linear polarization signal in O VI at 1032 Å which was derived by exploiting the instrumental polarization of the Solar and Heliospheric Observatory (SOHO)/Solar Ultraviolet Measurements of Emitted Radiation (SUMER) spectrometer. Raouafi, Lemaire, and Sahal-Bréchot (1999); Raouafi *et al.* (2002); Raouafi, Sahal-Bréchot, and Lemaire (2002) interpreted this signal in terms of Hanle effect and deduced a field strength of ≈ 3 G at 0.3 $R_\odot$ above a coronal hole. The Upgraded Coronal Multi-channel Polarimeter (UCOMP) produces full Stokes spectropolarimetric measurements in coronal emission lines ranging from 5303 Å to 10798 Å and, chromospheric lines due to H I at 6563 Å and He I at 10830 Å (Tomczyk *et al.*, 2022; Landi, Habbal, and Tomczyk, 2016). The Daniel K. Inouye Solar Telescope (DKIST) is routinely providing high resolution and high precision spectropolarimetric observations over the wavelength range of 3800 to 50,000 Å (Rast *et al.*, 2021; Harrington *et al.*, 2023). Visible Emission Line Coronagraph (VELC) onboard ADITYA-L1, a space based observatory which is recently launched in September 2023, is expected to produce spectropolarimetric observations of corona in Fe XIII 10747 Å line (Nagaraju *et al.*, 2021; Narra *et al.*, 2023). Another upcoming ground-based facility is the COronal Solar Magnetism Observatory (COSMO) which will comprise of the Large Coronagraph (LC), the K-coronagraph (K-cor) and the Chromospheric and Prominence Magnetometer (ChroMag) for the measurement of magnetic fields and thermodynamic conditions in the chromosphere and corona (Hou, de Wijn, and Tomczyk, 2013; Tomczyk *et al.*, 2016).

Understanding the fundamental physical processes occurring in the upper solar atmosphere requires accurate knowledge about vector magnetic field simultaneously at multiple heights. The magnetic field measurements reported above exhibit several limitations in inferring the vector magnetic field in the TR and corona. The linear polarization signal of magnetic-dipole transition (forbidden) lines is practically insensitive to TR and coronal field strengths (with Larmor frequency being much greater than lifetime of the upper level of transition), and can only constrain the field orientation in the plane perpendicular to LOS (House, 1977; Casini and Judge, 1999) through the saturated Hanle effect. The electric-dipole transition (permitted) lines, on the other hand, exhibit linear polarization signal which is, in theory, sensitive to the full vector magnetic field (due to Larmor frequency being comparable to upper level lifetime). Nevertheless, the LOS component of the field produces circular polarization through longitudinal Zeeman effect in case of both permitted and forbidden lines; however, the circularly polarized signal (Stokes V/I) induced by the coronal

magnetic field is very weak. The measurements by Lin, Kuhn, and Coulter (2004) have shown that the Stokes V/I signal in Fe XIII at 10747 Å is close to 10^{-4} for a LOS field strength of a few gauss. This signal is even weaker (explained in Section 2.3.1) at shorter wavelengths, such as far-ultraviolet (FUV) and extreme-ultraviolet (EUV), in the orders of 10^{-4} and 10^{-5}, respectively, for a line with comparable effective Landé factor and line steepness (i.e. $\frac{dI}{d\lambda}$). Meanwhile, Zhao *et al.* (2019) have estimated the Hanle polarization signal to be atleast 100 times stronger than the Zeeman polarization signal. Therefore, the critical Hanle effect offers a clear advantage to be used as a full vector magnetic field diagnostic.

Furthermore, Bommier, Sahal-Bréchot, and Leroy (1981) proposed a method which utilises a minimum of two permitted lines with different Hanle sensitivity to obtain the vector magnetic field information. This method has successfully been applied to derive the vector magnetic field in prominences (Leroy, 1977; Bommier *et al.*, 1994; Bommier, Leroy, and Sahal-Bréchot, 2021) and has also been extended to obtain empirical information on the TR fields (Trujillo Bueno, Štěpán, and Belluzzi, 2012). In principle, this method can be utilized to study the coronal fields as well. However, it is important to identify such amalgamation of spectral lines originating from high plasma temperatures of the TR and corona, which are well suited for diagnosing the magnetic fields in these layers.

2.2 Instruments and Data

In this analysis, we have utilized spectroscopic data from three different space-based missions. One is the EUV Imaging Spectrometer (EIS; Culhane, 2007), onboard the Hinode spacecraft, which is designed to observe in two wavelength ranges (SW: 166 – 212 Å; LW: 245 – 291 Å). These wavelength bands consist of several emission lines from highly ionised species ranging from 4.7 to 7.3 in the logarithmic scale of temperature ($\log_{10}$(T)). Another is a sounding rocket instrument, named the Extreme Ultraviolet Normal Incidence Spectrograph (EUNIS), which observed a coronal bright point around 18:12 UT on 2006 April 12. A brief description of the instrument has been provided by Brosius, Rabin, and Thomas (2007). The EUV spectra obtained by EUNIS covers first-order wavelengths from 300 to 370 Å over a temperature range of 5.2 to 6.4 in $\log_{10}$(T) (Brosius *et al.*, 2008). The third instrument is SUMER which is a high-resolution telescope and spectrograph, onboard the Solar and Heliospheric Observatory (SOHO), which observed the Sun over the wavelength range from 470 to 1609 Å (Curdt and Landi, 2001; Curdt, Landi, and Feldman, 2004).

2.3 Formulation and Methodology

The essence of Hanle effect in diagnosing the magnetic field is the modification of scattering polarization (i.e., linear polarization) in spectral lines and rotation of plane of polarization in the presence of external magnetic field. Such an effect is observed when the splitting of energy levels of a given spectral line due to external magnetic field is comparable to their natural line-width. This implies that the Hanle effect is most effective when (Bommier, Sahal-Bréchot, and Leroy, 1981)

$$g_u \omega_B \tau = 1, \tag{2.1}$$

where g_u is the Landé factor of the upper atomic level; ω_B is the Larmor frequency and τ is the lifetime of the upper energy level, which is equivalent to the reciprocal of summation over the Einstein A coefficients, assuming that radiation and collision induced transitions are negligible with respect to the spontaneous radiative de-excitation. When Eq. 2.1 is satisfied, the corresponding field strength is called the critical field (B_H). Bommier, Sahal-Bréchot, and Leroy (1981) have defined the domain of Hanle sensitivity as

$$0.1 \leq g_u \omega_B \tau \leq 10 \tag{2.2}$$

based on the uncertainty analysis of vector field determination. In the lower limit, the relative error on field strength is small but uncertainty in determining the field direction is large. In the upper limit, it is the vice-versa. The condition 2.2 is further restricted to the domain (Trujillo Bueno, 2014)

$$0.1 \leq g_u \omega_B \tau \leq 5 \tag{2.3}$$

which is used for the selection of suitable spectral lines with varied Hanle sensitivity, as shown in Table 2.1.

Given the expected field strength in the TR and corona, permitted lines are mostly in the Hanle regime due to their shorter lifetimes (in the order of 10^{-8} s). On the other hand, magnetic sub-levels of the forbidden lines are well separated (i.e., $g_u \omega_B \tau \gg 5$, which breaks the condition 2.3). As a consequence, only the LOS field strength through circular polarization (Harvey, 1969) and the field azimuth through Hanle regime linear polarization (Querfeld and Smartt, 1984; Arnaud and Newkirk, 1987) can be determined by utilizing these lines. This is because the linear polarization produced by the transverse Zeeman effect is below the detection level of current observational capabilities for magnetic fields of a few gauss. Therefore, Stokes Q and U, in case of the forbidden lines, are completely dominated by the residual atomic alignment*

*Atomic alignment is defined as the differential pumping of the atomic states, with magnetic quantum numbers $|M|$, due to anisotropic illumination of the atoms.

which does not depend on the field strength (the so-called saturated Hanle effect: [†] Sahal-Bréchot (1977)). In the upcoming sections, we have discussed and estimated various parameters required for selecting the Hanle sensitive lines which are suitable to probe the weak magnetic fields of the TR and corona.

2.3.1 Stokes V/I estimation

The Zeeman effect is caused by the splitting of the energy levels in the presence of external magnetic field which produces characteristic polarization depending on the orientation of vector magnetic field with respect to the observer's LOS. Under the weak field approximation (Landi Degl'Innocenti and Landolfi, 2004), the relation between Stokes V/I and the longitudinal magnetic field ($B_{\parallel}$) is given by

$$\frac{V(\lambda)}{I(\lambda)} = -4.67 \times 10^{-13}\ \overline{g}\lambda^2 B_{\parallel} \frac{1}{I(\lambda)} \frac{dI(\lambda)}{d\lambda}, \tag{2.4}$$

where $\frac{dI(\lambda)}{d\lambda}$ is the intensity derivative with respect to wavelength, and $\overline{g}$ is the effective Landé factor. Due to the dependence of Stokes V amplitude on $\overline{g}$, λ and $\frac{dI(\lambda)}{d\lambda}$, which usually differ from one spectral line to the other, it is useful to estimate the Stokes V sensitivity of the spectral lines in UV so that this information may be combined with the Hanle measurements to infer the vector magnetic field. For this study, the spectroscopic observations from the SUMER spectrometer (Curdt and Landi, 2001; Curdt, Landi, and Feldman, 2004) have been used and relevant data was downloaded from https://sdac.virtualsolar.org.

Before estimating the intensity derivative, the spectral profiles corresponding to a given spectral line are fitted with Gaussian function. The derivatives of intensity with respect to wavelength are calculated and normalized to the local intensity of each Gaussian fitted profile. Then the mean of the derivative values (absolute and normalized) at half-maxima of both the blue and the red wings is obtained. Using the mean derivative value in Eq. 2.4, the Stokes V/I amplitude is estimated for each Gaussian fitted profile along the spatial axis. Finally, the mean Stokes V/I amplitude is calculated for a given spectral line. The standard deviation of the Stokes V/I amplitude is also estimated relative to its mean value over the fitted spectral profiles. In the above analysis, the Stokes V/I amplitude increases by 1.3 (for detector A) and 1.1 (for detector B) when the Stokes I profiles are corrected for the instrumental broadening. This implies that there is no significant change in the Stokes V/I amplitudes due to instrumental broadening effect and therefore while calculating Stokes V/I, it can safely be unaccounted for.

Figure 2.1 shows the sample mean intensity profiles of a forbidden line in FUV

[†]In the saturation limit of the Hanle effect, all the quantum level coherence is destroyed, while only the population imbalance due to the anisotropic radiation remains, which is insensitive to the field strength.

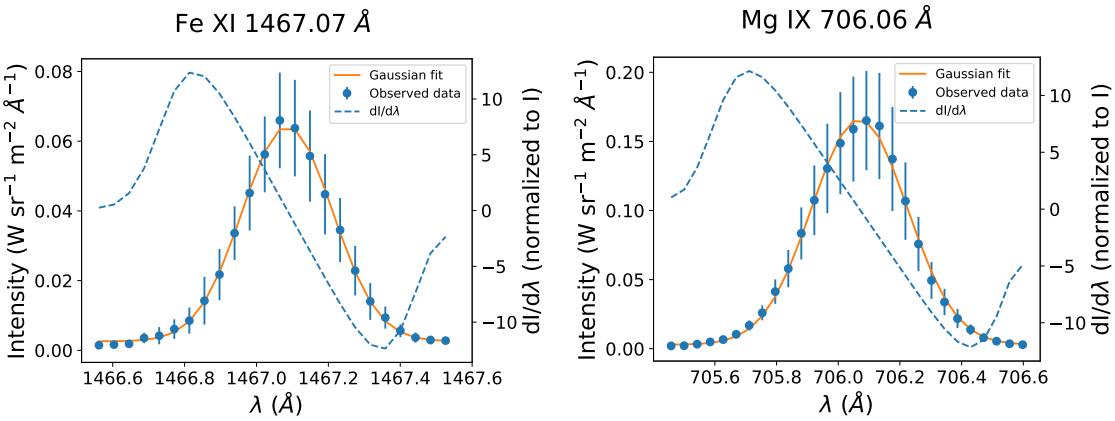

Figure 2.1: Sample intensity profiles of Fe XI at 1467 Å (left panel), and Mg IX at 706 Å (right panel) are shown along with their corresponding derivative plots. The solid orange curves are the Gaussian fit to the observed blue data points (the filled circles). The error bars correspond to the dispersion in intensity values across the spatial pixels over which the spectral profiles are averaged. The dotted curves are the derivatives of the fitted Gaussian curves normalized to the local intensities.

due to Fe XI at 1467 Å (left panel) and a permitted line in EUV due to Mg IX at 706 Å (right panel) along with their corresponding mean intensity derivatives (the dotted curves). The error bars correspond to the dispersion in intensity values across 24 spatial pixels over which the spectral profiles are averaged. For a LOS field of 10 G, the Stokes V/I amplitudes for Fe XI at 1467 Å and for Mg IX at 706 Å (both having $\overline{g}$ as 1.5, see Table 2.1) are estimated as 1.34×10^{-4} and 2.6×10^{-5}, respectively.

2.3.2 Transition probability

The lifetime of the upper energy level is equal to the reciprocal of sum over the Einstein A coefficients, i.e. $\tau = \frac{1}{\sum_j A_{kj}}$. Transition probability or the Einstein A coefficient ($A = \sum_j \mathrm{A}_{kj}$) is the total rate of all spontaneous radiative transitions from the upper level (k) to all the lower levels to which the level k can de-excite. These coefficients help in determining the range of magnetic field strength to which the spectral lines are sensitive in the Hanle regime (cf. Eqs. 2.1 and 2.2). Besides, they are also important for the visibility of the spectral lines in the solar corona. The A values are obtained from current version 10.0 of the CHIANTI atomic database (Dere *et al.*, 1997; Del Zanna *et al.*, 2021) and are listed in the sixth column of Table 2.1.

2.3.3 Landé factors

In light elements, the electrostatic interaction dominates over the spin-orbit coupling such that the orbital angular momenta of the individual electrons get coupled to give a total orbital angular momentum $\vec{L}$, while the spins of the electrons get coupled to

give a total spin $\vec{S}$. This is referred to as Russell-Saunders or LS coupling. However, for heavier atoms with larger nuclear charge, the spin-orbit interactions are stronger leading to jj coupling. A more general and practical case exists in certain atoms, particularly mid-weight atoms and those with almost closed shells, which lie in between these two coupling limits. Such a coupling is termed as intermediate or i-coupling, in which both the electrostatic and the spin-orbit interactions may be present with a relative order of magnitude. From the selection rules described in Condon and Shortley (1935) and Drake (2006), the coupling scheme of the atomic levels associated with the dipole (electric or magnetic) transitions are identified. In case of LS coupling, the following expression is used to determine the Landé factors of individual energy levels.

$$g = \frac{3}{2} + \frac{S(S+1) - L(L+1)}{2J(J+1)} \tag{2.5}$$

where $\vec{L}$ and $\vec{S}$ are the total orbital and spin angular momentum quantum numbers, respectively; and $\vec{J}$ is the total angular momentum which is defined as $\vec{J} = \vec{L} + \vec{S}$. Eq. 2.5 holds only for LS coupling scheme which may fail in cases involving atomic or ionic lines of high excitation potential and intermediate coupling may have to be considered.

There are no lines exhibiting jj coupling in this analysis. For intermediate coupling, the Landé factors g_1 and g_2 are first estimated using formula 2.5, and then compared with the corresponding values from Verdebout *et al.* (2014). It is found that the values calculated in this work match closely with those estimated using the GRASP2K (Jönsson *et al.*, 2007) code in Verdebout *et al.* (2014). GRASP2K is a fully relativistic multiconfiguration Dirac-Hartree-Fock (MCDHF) method based atomic structure package. The Landé factors of the individual levels are listed in the seventh column of Table 2.1. The effective Landé factors are calculated using the following formula (Landi Degl'Innocenti, 1982),

$$\overline{g} = \frac{1}{2}(g_1 + g_2) + \frac{1}{4}(g_1 - g_2)[J_1(J_1+1) - J_2(J_2+1)] \ , \tag{2.6}$$

where $\vec{J_1}$ and g_1 are total angular momentum and Landé factor of the lower energy level, respectively; $\vec{J_2}$ and g_2 correspond to that of the upper energy level. All the estimated values of $\overline{g}$ factor are listed in the eighth column of Table 2.1.

2.3.4 Polarizability coefficient

The polarizability coefficient (W_2) is a scaling factor which quantifies the fraction of linear polarization produced by resonant scattering of the incoming radiation. Analytical expressions for W_2 for the allowed transitions corresponding to $\Delta J = J_2 - J_1 = 0, \pm 1$ (with $J_2 = J_1 = 0$ being forbidden) are given by (Stenflo, 1994)

Case I: When $J_2 = J_1 - 1$,

$$W_2 = \frac{(J_1 - 1)(2J_1 - 3)}{10J_1(2J_1 + 1)} \tag{2.7}$$

Case II: When $J_2 = J_1$,

$$W_2 = \frac{(2J_1 - 1)(2J_1 + 3)}{10J_1(J_1 + 1)} \tag{2.8}$$

Case III: When $J_2 = J_1 + 1$,

$$W_2 = \frac{(J_1 + 2)(2J_1 + 5)}{10(J_1 + 1)(2J_1 + 1)} \tag{2.9}$$

The calculated values of W_2 for the corresponding FUV and EUV spectral lines are listed in the tenth column of Table 2.1.

2.3.5 Line irradiance and other properties

The EIS off-limb spectra consists of spectral lines whose intensities over active region and quiet sun have been collected from Del Zanna (2012). The off-limb line intensities from 470 to 1609 Å spanning over three regions, i.e., quiet sun (QS), active region (AR) and coronal hole (CH), have been assembled from Curdt, Landi, and Feldman (2004). All the line irradiances from EIS and SUMER are available in the units of photons cm^{-2} s^{-1} $arcsec^{-2}$. But for the EUNIS on-disk observations of spectral lines from 300 to 370 Å, the given line irradiances are converted from erg cm^{-2} s^{-1} sr^{-1} to photons cm^{-2} s^{-1} $arcsec^{-2}$ (see Eq. 2.10) in order to simplify the comparison with other spectral lines (from EIS and SUMER observations) used in the present analysis. The spectral irradiances for different solar regions are listed in Table 2.1 in the units of photons $cm^{-2}s^{-1}arcsec^{-2}$.

$$1\ erg\ cm^{-2}s^{-1}sr^{-1} = 11.8324 \times 10^{-4} \times \lambda\ photons\ cm^{-2}s^{-1}arcsec^{-2}\ , \tag{2.10}$$

where λ is the wavelength (in Å) of the corresponding spectral line.

The atomic species along with their ionization state are listed in the first column and the observed wavelength in Angstrom (Å) is given in the second column. In the third, fourth and fifth column, we have listed the corresponding level configurations, the peak formation temperature (logarithmic value) of the lines, and their transition type, respectively. These line formation temperatures are obtained from Feldman *et al.* (1997); Brosius *et al.* (2008); Curdt and Landi (2001); Zanna and Mason (2005); Young *et al.* (2007); Moran (2003). Although the peak formation temperature is mentioned for most of the spectral lines in Table 2.1, it should be noted that the lines are always formed in a range of temperature, not at a single value (Feldman *et al.*,

1998; Warren and Warshall, 2002; Warren and Brooks, 2009; Saqri *et al.*, 2020). For example, any spectral line shown at $\log_{10}(T) = 6.1$ may actually be formed within a range of $\log_{10}(T) = 5.85$ to 6.3. Further, the critical Hanle field strength (B_H in G) for maximum Hanle sensitivity are listed in the ninth column.

2.4 Results and Discussion

The search for spectral lines in FUV and EUV to probe vector magnetic field has been discussed in this Chapter. The outcome of this search is summarized in a graphical representation shown in Figure 2.2. In this figure, each line is represented by a rectangular box with its length along Y-axis indicating the range of magnetic field sensitivity, due to Hanle effect as dictated by Eq. 2.3. The width of the box along X-axis is not a true representation of temperature sensitivity range, but only to indicate the peak formation temperature given in logarithmic scale. Actual temperature sensitivity extends much beyond that is indicated by the width of the box. Each box is marked by the wavelength of the spectral line along with the corresponding name of the ion and the Hanle critical magnetic field (B_H). The closed solid circles in this figure represent the FUV lines, whose locations along X and Y-axis indicate, respectively, the peak formation temperature and the assumed field strength of 10 G (at which their estimated Stokes V/I signal is in the order of 10^{-4}).

While selecting the spectral lines presented in Figure 2.2, the polarizability coefficient (W_2), line irradiance and B_H are considered. Only lines with B_H in the range 0.01 - 200 G, $W_2 > 0$ and their intensity > 1 photon cm^{-2}s^{-1}arcsec^{-2} are shown in this figure. The range of field strength chosen is directed by the magnetic field measurements reported in the literature (see for e.g., Figure 5. of Peter *et al.*, 2012 and Figure 4. of Sasikumar Raja *et al.*, 2021).

Regarding the intensity criteria, it is apparent that the spectral lines with maximum irradiance should be chosen as spectropolarimetric observations are photon starved. However, it is difficult to find spectral lines with high irradiance which are sensitive to Hanle and Zeeman effects, and cover a suitable temperature range as well. The O VI line at 1031.91 Å is a good Hanle sensitive line both in terms of number of photons and B_H. However, in order to derive vector magnetic field there is no spectral line (in close proximity) with the same peak formation temperature. Given the fact that the line formation temperature is not a delta function but has a range, this line can be used with other lines having adjacent formation temperature. For instance, this line can be used together with Ne VIII at 770.42 Å to derive vector magnetic field information. Although the number of photons in these two lines are relatively close, they are separated in their wavelengths by ≈ 260 Å and formation temperature differs by ≈ 0.3 on logarithmic scale. Similarly, Ly-α line at 1215.67 Å is sensitive to Hanle effect ($B_H = 53$ G) having extremely high line irradiance. However, there is

Table 2.1: Table showing ionization state of the atomic species, corresponding wavelength and level configuration, temperature of line formation ($\log_{10}$(T)), type of transition (TT: E1 or M1), effective Landé factor ($\overline{g}$) , critical field strength (B_H), polarizability coefficient (W_2) and line irradiances in three different solar regions. E1 and M1 refer to electric dipole and magnetic dipole transitions, respectively. $^{2S+1}L_J$ is the notation used in each atomic level configuration, where L, S and J are total orbital, spin and angular momentum quantum numbers respectively.

Ion	**λ(Å)**	**Transition (i-k)**	**$\log_{10}$(T)**	**TT**	$A(s^{-1})$	$\mathbf{g_i - g_k}$	$\overline{\mathbf{g}}$	$\mathbf{B}_H$ **(gauss)**	$\mathbf{W}_2$	**L** (ph cm^{-2}s^{-1}arcsec^{-2}) **QS**	**AR**	**CH**
Fe IX	171.073	$3s^2\ 3p^6\ {}^1S_0$ - $3s^2\ 3p^5\ 3d\ {}^1P_1$	6.11	E1	2.28×10^{11}	1 - 1	1	25817	1	140.7	265	-
Fe X	174.531	$3s^2\ 3p^5\ {}^2P_{3/2}$ - $3s^2\ 3p^4\ 3d\ {}^2D_{5/2}$	6	E1	1.86×10^{11}	1.33-1.2	1.1	17551	0.28	119.7	172.7	-
Fe X	184.537	$3s^2\ 3p^5\ {}^2P_{3/2}$ - $3s^2\ 3p^4\ 3d\ {}^2S_{1/2}$	6	E1	1.63×10^{11}	1.33 - 2	1.17	9245	0	33.6	47.9	-
Fe XII	195.119	$3s^2\ 3p^3\ {}^4S_{3/2}$ - $3s^2\ 3p^2\ 3d\ {}^4P_{5/2}$	6.1	E1	8.83×10^{10}	2 - 1.6	1.3	6249	0.28	136.2	312	-
Fe XIII	202.044	$3s^2\ 3p^2\ {}^3P_0$ - $3s^2\ 3p\ 3d\ {}^3P_1$	6.2	E1	5.33×10^{10}	1.5 - 1.5	1.5	4024	1	103.3	349.5	-
Si X	258.374	$2s^2\ 2p\ {}^2P_{3/2}$ - $2s\ 2p^2\ {}^2P_{3/2}$	6.1	E1	1.72×10^{10}	1.33-1.33	1.33	1461	0.32	44.1	66.3	-
Si X	261.056	$2s^2\ 2p\ {}^2P_{3/2}$ - $2s\ 2p^2\ {}^2P_{1/2}$	6.1	E1	1.68×10^{10}	1.33-0.67	1.5	2853	0	26.3	37.8	-
Fe XIV	264.788	$3s^2\ 3p\ {}^2P_{3/2}$ - $3s\ 3p^2\ {}^2P_{3/2}$	6.3	E1	4.26×10^{10}	1.33-1.33	1.33	3618	0.32	17.1	92.1	-
Fe XV	284.163	$3s^2\ {}^1S_0$ - $3s\ 3p\ {}^1P_1$	6.3	E1	2.11×10^{10}	1 - 1	1	2389	1	24.3	576.6	-
Si XI	303.325	$1s^2\ 2s^2\ {}^1S_0$ - $1s^2\ 2s\ 2p\ {}^1P_1$	6.2	E1	6.38×10^{9}	1 - 1	1	722	1	-	1049	-
Fe XI	308.544	$3s^2\ 3p^4\ {}^1D_2$ - $3s\ 3p^5\ {}^1P_1$	6.1	E1	8.84×10^{9}	1 - 1	1	1001	0.01	-	13	-
Fe XIII	312.174	$3s^2\ 3p^2\ {}^3P_1$ - $3s\ 3p^3\ {}^3P_1$	6.2	E1	4.07×10^{9}	1.5 - 1.5	1.5	307	0.25	-	12	-

Ion	λ(Å)	Transition (i-k)	$\log_{10}$(T)	TT	$A(s^{-1})$	$g_i - g_k$	$\overline{g}$	B_H (gauss)	W_2	L (ph cm^{-2}s^{-1}arcsec^{-2}) QS	AR	CH
Fe XIII	318.13	$3s^2\ 3p^2\ {}^1D_2$ - $3s\ 3p^3\ {}^1D_2$	6.2	E1	5.61×10^9	1 - 1	1	635	0.35	-	10.8	-
Fe XIII	320.8	$3s^2\ 3p^2\ {}^3P_2$ - $3s\ 3p^3\ {}^3P_2$	6.2	E1	3.89×10^9	1.5 - 1.5	1.5	294	0.35	-	40.4	-
Fe XV	327.033	$3s\ 3p\ {}^3P_2$ - $3p^2\ {}^1D_2$	6.3	E1	4.67×10^9	1.5 - 1	1.25	529	0.35	-	6.4	-
Cr XIII	328.268	$2p^6\ 3s^2\ {}^1S_0$ - $3s\ 3p\ {}^1P_1$	6.2	E1	1.73×10^{10}	1 - 1	1	1959	1	-	25	-
Al X	332.79	$1s^2\ 2s^2\ {}^1S_0$ - $1s^2\ 2s\ 2p\ {}^1P_1$	6.1	E1	5.74×10^9	1 - 1	1	650	1	-	35.2	-
Fe XIV	334.178	$3s^2\ 3p\ {}^2P_{1/2}$ - $3s\ 3p^2\ {}^2D_{3/2}$	6.3	E1	2.49×10^9	0.67 - 0.8	0.83	352	0.5	-	74	-
Fe XVI	335.409	$2p^6\ 3s\ {}^2S_{1/2}$ - $2p^6\ 3p\ {}^2P_{3/2}$	6.4	E1	7.87×10^9	2 - 1.33	1.17	669	0.5	-	159	-
Fe XII	338.263	$3s^2\ 3p^3\ {}^2D_{5/2}$ - $3s\ 3p^4\ {}^2D_{5/2}$	6.1	E1	3.37×10^9	1.2 - 1.2	1.2	318	0.37	-	23.8	-
Fe XI	341.113	$3s^2\ 3p^4\ {}^3P_2$ - $3s\ 3p^5\ {}^3P_1$	6.1	E1	3.28×10^9	1.5 - 1.5	1.5	248	0.01	-	25.5	-
Si IX	341.949	$2s^2\ 2p^2\ {}^3P_0$ - $2s\ 2p^3\ {}^3D_1$	6.1	E1	2.4×10^9	1.5 - 0.5	1	544	1	-	18.2	-
Fe XII	346.852	$3s^2\ 3p^3\ {}^4S_{3/2}$ - $3s\ 3p^4\ {}^4P_{1/2}$	6.1	E1	1.86×10^9	2 - 2.67	1.83	-	0	-	30.2	-
Fe XIII	348.183	$3s^2\ 3p^2\ {}^3P_0$ - $3s\ 3p^3\ {}^3D_1$	6.2	E1	1.61×10^9	1.5 - 0.5	1	365	1	-	29.3	-
Fe XII	352.106	$3s^2\ 3p^3\ {}^4S_{3/2}$ - $3s\ 3p^4\ {}^4P_{3/2}$	6.1	E1	1.64×10^9	2 - 1.73	1.87	107	0.32	-	64.8	-

Ion	λ**(Å)**	**Transition (i-k)**	$\log_{10}$**(T)**	**TT**	$A(s^{-1})$	$\mathbf{g_i - g_k}$	$\overline{\mathbf{g}}$	$\mathbf{B}_H$ **(gauss)**	$\mathbf{W}_2$	**L** (ph cm^{-2}s^{-1}arcsec^{-2}) **QS**	**AR**	**CH**
Fe XI	352.67	$3s^2\ 3p^4\ {}^3P_2$ - $3s\ 3p^5\ {}^3P_2$	6.1	E1	3.11×10^9	1.5 - 1.5	1.5	235	0.35	-	64.3	-
Fe XIV	353.829	$3s^2\ 3p\ {}^2P_{3/2}$ - $3s\ 3p^2\ {}^2D_{5/2}$	6.3	E1	1.9×10^9	1.33 - 1.2	1.1	179	0.28	-	38.6	-
Fe XI	356.519	$3s^2\ 3p^4\ {}^3P_1$ - $3s\ 3p^5\ {}^3P_1$	6.1	E1	3.28×10^9	1.5 - 1.5	1.5	248	0.25	-	10.4	-
Fe XIII	359.644	$3s^2\ 3p^2\ {}^3P_1$ - $3s\ 3p^3\ {}^3D_2$	6.2	E1	1.5×10^9	1.5 - 1.17	1	146	0.35	-	54.1	-
Fe XIII	359.839	$3s^2\ 3p^2\ {}^3P_1$ - $3s\ 3p^3\ {}^3D_1$	6.2	E1	1.61×10^9	1.5 - 0.5	1	365	0.25	-	5.3	-
Fe XVI	360.758	$2p^6\ 3s\ {}^2S_{1/2}$ - $2p^6\ 3p\ {}^2P_{1/2}$	6.4	E1	6.34×10^9	2 - 0.67	1.33	-	0	-	76.9	-
Fe XII	364.467	$3s^2\ 3p^3\ {}^4S_{3/2}$ - $3s\ 3p^4\ {}^4P_{5/2}$	6.1	E1	1.62×10^9	2 - 1.6	1.33	115	0.28	-	85.4	-
Mg IX	368.071	$1s^2\ 2s^2\ {}^1S_0$ - $1s^2\ 2s\ 2p\ {}^1P_1$	6.0	E1	5.12×10^9	1 - 1	1	580	1	-	486	-
Fe XI	369.163	$3s^2\ 3p^4\ {}^3P_1$ - $3s\ 3p^5\ {}^3P_2$	6.1	E1	3.11×10^9	1.5 - 1.5	1.5	235	0.35	-	20.5	-
Si XII	499.4	$1s^2\ 2s\ {}^2S_{1/2}$ - $1s^2\ 2p\ {}^2P_{3/2}$	6.3	E1	9.61×10^8	2 - 1.33	1.17	82	0.5	23.3	166.4	-
Si XII	520.67	$1s^2\ 2s\ {}^2S_{1/2}$ - $1s^2\ 2p\ {}^2P_{1/2}$	6.26	E1	8.48×10^8	2 - 0.67	1.33	-	0	13.3	100.9	-
Al XI	550.031	$1s^2\ 2s\ {}^2S_{1/2}$ - $1s^2\ 2p\ {}^2P_{3/2}$	6.26	E1	8.52×10^8	2 - 1.33	1.17	72	0.5	7.9	48.5	-
Ca X	557.76	$2p^6\ 3s\ {}^2S_{1/2}$ - $2p^6\ 3p\ {}^2P_{3/2}$	5.85 – 6	E1	3.77×10^9	2 - 1.33	1.17	320	0.5	9.0	19.7	5.2

Ion	λ(Å)	Transition (i-k)	$\log_{10}$(T)	TT	$A(s^{-1})$	$g_i - g_k$	$\overline{g}$	B_H (gauss)	W_2	L (ph cm^{-2}s^{-1}arcsec^{-2}) QS	AR	CH
Al XI	568.12	$1s^2\ 2s\ ^2S_{1/2}$ - $1s^2\ 2p\ ^2P_{1/2}$	6.26	E1	7.73×10^8	2 - 0.67	1.33	-	0	5.3	23.5	-
Ca X	574.01	$2p^6\ 3s\ ^2S_{1/2}$ - $2p^6\ 3p\ ^2P_{1/2}$	5.85 – 6	E1	3.47×10^9	2 - 0.67	1.33	-	0	6.0	12.2	3.2
Si XI	604.15	$2s\ 2p\ ^1P_1$ - $2p^2\ ^1D_2$	6.26	E1	1.09×10^9	1 - 1	1	123	0.35	2.5	4.1	-
Mg X	609.793	$1s^2\ 2s\ ^2S_{1/2}$ - $1s^2\ 2p\ ^2P_{3/2}$	6.04	E1	7.53×10^8	2 - 1.33	1.17	64	0.5	213	341	26
Mg X	624.94	$1s^2\ 2s\ ^2S_{1/2}$ - $1s^2\ 2p\ ^2P_{1/2}$	6	E1	7×10^8	2 - 0.67	1.33	-	0	118	346	16
Al X	637.763	$2s^2\ ^1S_0$ - $2s\ 2p\ ^3P_1$	6.15	E1	1.94×10^5	1 - 1.5*	1.5	0.01	1	3	4.9	0.18
Al X	670.053	$2s\ 2p\ ^1P_1$ – $2p^2\ ^1D_2$	6.13	E1	9.38×10^8	1 - 1	1	106	0.35	0.38	0.61	0.07
Si IX	676.503	$2s^2\ 2p^2\ ^3P_1$ - $2s\ 2p^3\ ^5S_2$	6.05	E1	6.54×10^4	1.5 - 2*	2.25	$\ll 1$	0.35	2.0	2.1	0.63
Al IX	680.318	$2s^2\ 2p\ ^2P_{1/2}$ - $2s\ 2p^2\ ^4P_{3/2}$	6.02	E1	3.75×10^4	0.67 - 1.73*	2	$\ll 1$	0.5	4.3	4.4	0.33
Na IX	681.719	$1s^2\ 2s\ ^2S_{1/2}$ - $1s^2\ 2p\ ^2P_{3/2}$	5.92	E1	6.78×10^8	2 - 1.33	1.17	58	0.5	7.6	34.6	4.9
Mg VIII	689.641	$2s\ 2p^2\ ^2P_{3/2}$ - $2p^3\ ^2D_{5/2}$	[a] 5.95	E1	4.15×10^9	1.33 - 1.2	1.1	392	0.28	0.31	0.76	0.33
Na IX	694.261	$1s^2\ 2s\ ^2S_{1/2}$ - $1s^2\ 2p\ ^2P_{1/2}$	5.92	E1	6.42×10^8	2 - 0.67	1.33	-	0	3.5	18.4	2.6

[a] Moran, 2003

* Landé factor of upper and lower energy level has been compared with Verdebout *et al.* (2014)

Ion	**λ(Å)**	**Transition (i-k)**	**$\log_{10}$(T)**	**TT**	$A(s^{-1})$	$\mathbf{g_i - g_k}$	$\overline{\mathbf{g}}$	$\mathbf{B}_H$ **(gauss)**	$\mathbf{W}_2$	**L** (ph cm^{-2}s^{-1}arcsec^{-2}) **QS**	**AR**	**CH**
Si IX	694.686	$2s^2\ 2p^2\ {}^3P_2$ - $2s\ 2p^3\ {}^5S_2$	6.05	E1	2.16×10^5	1.5 - 2*	1.75	0.01	0.35	4.1	6.7	1.5
Ar VIII	700.24	$2p^6\ 3s\ {}^2S_{1/2}$ - $2p^6\ 3p\ {}^2P_{3/2}$	5.61	E1	2.7×10^9	2 - 1.33	1.17	229	0.5	1.0	1.3	0.87
Mg IX	706.06	$1s^2\ 2s^2\ {}^1S_0$ - $1s^2\ 2s\ 2p\ {}^3P_1$	5.99	E1	9.7×10^4	1 - 1.5*	1.5	$\ll 1$	1	10.2	21.5	9.2
Ar VIII	713.801	$2p^6\ 3s\ {}^2S_{1/2}$ - $2p^6\ 3p\ {}^2P_{1/2}$	5.61	E1	2.56×10^9	2 - 0.67	1.33	-	0	0.45	0.85	0.51
Mg IX	749.552	$1s^2\ 2s\ 2p\ {}^1P_1$ - $1s^2\ 2p^2\ {}^1D_2$	5.85–6	E1	7.96×10^8	1 - 1	1	90	0.35	1.6	4.4	1.6
Mg VIII	762.66	$2s^2\ 2p\ {}^2P_{1/2}$ - $2s\ 2p^2\ {}^4P_{3/2}$	5.91	E1	1.82×10^4	0.67 - 1.73*	2	$\ll 1$	0.5	0.1	0.35	0.33
Mg VIII	769.355	$2s^2\ 2p\ {}^2P_{1/2}$ - $2s\ 2p^2\ {}^4P_{1/2}$	5.91	E1	1.38×10^5	0.67 - 2.67*	1.67	-	0	0.24	0.97	0.97
Ne VIII	770.42	$1s^2\ 2s\ {}^2S_{1/2}$ - $1s^2\ 2p\ {}^2P_{3/2}$	5.85-6	E1	5.76×10^8	2 - 1.33	1.17	49	0.5	39.5	177.9	41.4
Mg VIII	772.26	$2s^2\ 2p\ {}^2P_{3/2}$ - $2s\ 2p^2\ {}^4P_{5/2}$	5.91	E1	6.06×10^4	1.33 - 1.6*	1.8	$\ll 1$	0.28	1.3	4.8	4.1
S X	776.373	$2s^2 2p^3\ {}^4S_{3/2}$ - $2s^2\ 2p^3\ {}^2P_{3/2}$	6.14	M1	4.92×10^2	2 - 1.33*	1.66	$\ll 1$	0.32	2.3	4.1	0.14
Ne VIII	780.385	$1s^2 2s\ {}^2S_{1/2}$ - $1s^2\ 2p\ {}^2P_{1/2}$	5.85-6	E1	5.54×10^8	2 - 0.67	1.33	-	0	33.1	113.9	29.7
Mg VIII	782.362	$2s^2\ 2p\ {}^2P_{3/2}$ - $2s\ 2p^2\ {}^4P_{3/2}$	5.85-6	E1	1.82×10^4	1.33 - 1.73*	1.53	$\ll 1$	0.32	1.2	3.3	3.9
S XI	782.981	$2s^2\ 2p^2\ {}^3P_1$ - $2s^2\ 2p^2\ {}^1S_0$	6.15	M1	9.14×10^2	1.5 - 1*	1.5	-	0	1.0	2.4	-

* Landé factor of upper and lower energy level has been compared with Verdebout *et al.* (2014)

Ion	λ(Å)	Transition (i-k)	$\log_{10}$(T)	TT	$A(s^{-1})$	$g_i - g_k$	$\overline{g}$	B_H (gauss)	W_2	L (ph cm^{-2}s^{-1}arcsec^{-2}) QS	AR	CH
S X	787.557	$2s^2\ 2p^3\ {}^4S_{3/2}$ - $2s^2\ 2p^3\ {}^2P_{1/2}$	6.26	M1	1.4×10^2	2 - 0.67*	2.34	-	0	1.5	2.4	-
Mg VIII	789.409	$2s^2\ 2p\ {}^2P_{3/2}$ - $2s\ 2p^2\ {}^4P_{1/2}$	5.6	E1	1.38×10^5	1.33 - 2.67*	0.995	-	0	0.27	1.2	0.95
Na VIII	789.808	$2s^2\ {}^1S_0$ - $2s\ 2p\ {}^3P_1$	5.85-6	E1	4.51×10^4	1 - 1.5*	1.5	$\ll 1$	1	0.17	1.3	0.77
Na VIII	847.91	$2s\ 2p\ {}^1P_1$ - $2p^2\ {}^1D_2$	5.6	E1	6.66×10^8	1 - 1	1	75	0.35	0.053	-	0.16
S VIII	867.88	$2p^4\ 3s\ {}^4P_{1/2}$ - $2p^4\ 3p\ {}^4D_{3/2}$	5.85-6	E1	1.56×10^9	2.67 - 1.2	0.83	147	0.5	0.068	-	-
Si IX	950.083	$2s^2\ 2p^2\ {}^3P_1$ - $2s^2\ 2p^2\ {}^1S_0$	5.85-6	M1	2.13×10^2	1.5 - 1*	1.5	-	0	2.6	5.2	1.3
O VI	1031.912	$2s\ {}^2S_{1/2}$ - $2p\ {}^2P_{3/2}$	5.6	E1	4.16×10^8	2 - 1.33	1.17	35	0.5	124	260	74
O VI	1037.613	$2s\ {}^2S_{1/2}$ - $2p\ {}^2P_{1/2}$	5.6	E1	4.1×10^8	2 - 0.67	1.33	-	0	50.6	124	33.9
S X	1212.93	$2s^2\ 2p^3\ {}^4S_{3/2}$ - $2s^2\ 2p^3\ {}^2D_{3/2}$	6.15	M1	1.56×10^1	2 - 0.8*	1.4	$\ll 1$	0.32	9.6	15.5	0.38
H I	1215.67	$1s\ {}^2S_{1/2}$ - $2p\ {}^2P_{3/2}$	4 - 5.5	E1	6.26×10^8	2 - 1.33	1.17	53	0.5	[b]1.5×10^5	-	-
Fe XII	1242	$3s^2\ 3p^3\ {}^4S_{3/2}$ - $3s^2\ 3p^3\ {}^2P_{3/2}$	6.26	M1	5.4×10^2	2 - 1.33	1.67	$\ll 1$	0.32	30.9	47.8	0.81
Fe XII	1349.4	$3s^2\ 3p^3\ {}^4S_{3/2}$ - $3s^2\ 3p^3\ {}^2P_{1/2}$	6.15	M1	2.38×10^2	2 - 0.67	2.34	-	0	18.1	28.5	0.41
Fe XI	1467.07	$3s^2\ 3p^4\ {}^3P_1$ - $3s^2\ 3p^4\ {}^1S_0$	6.15	M1	8.87×10^2	1.5 - 1	1.5	-	0	12.5	15.5	1.5

[b] Tian *et al.*, 2009

* Landé factor of upper and lower energy level has been compared with Verdebout *et al.* (2014)

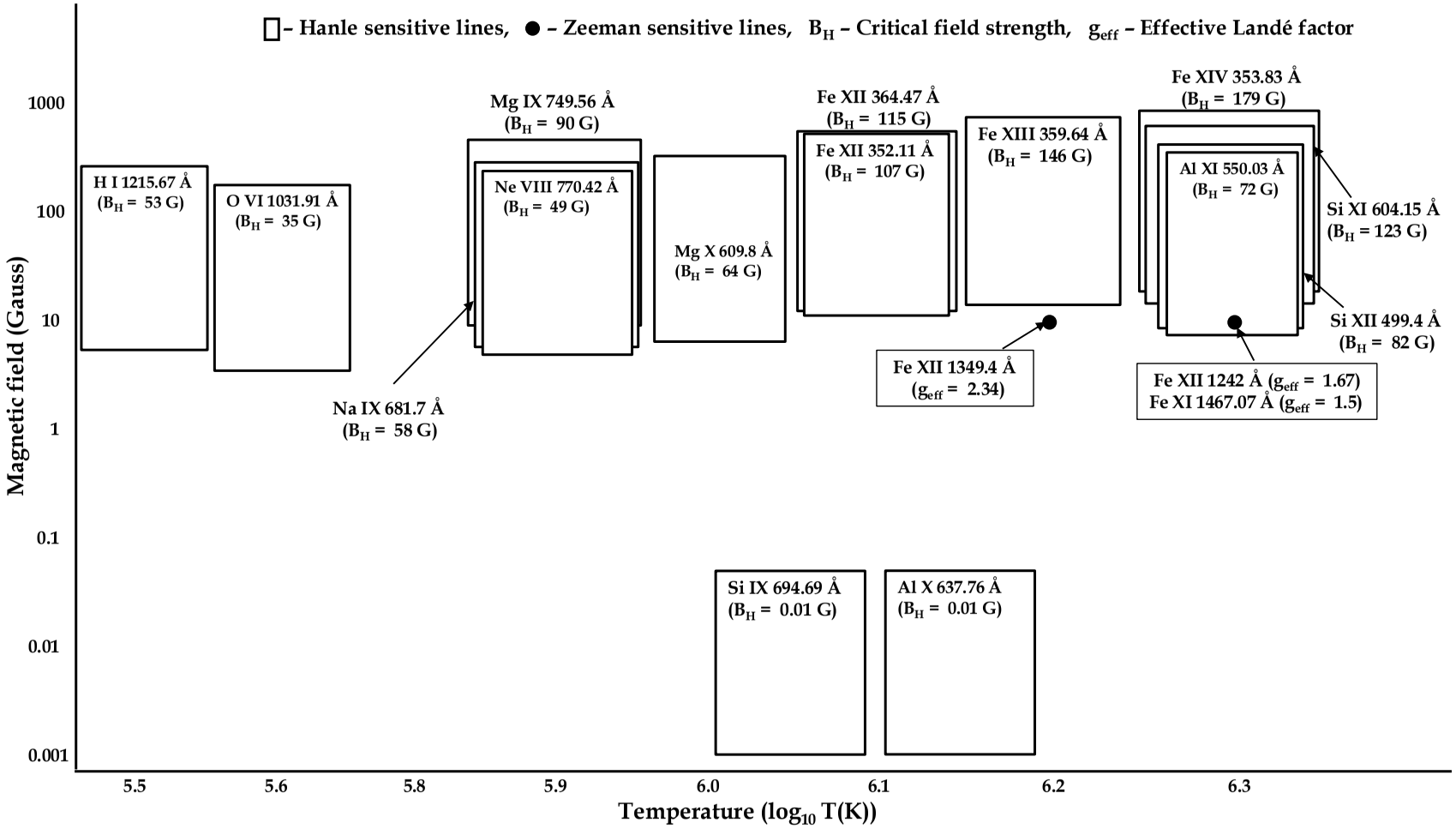

Figure 2.2: Graphical representation of magnetic sensitivity of the spectral lines in the domain of Hanle effect (cf. Eq. 2.3). The domains are shown in rectangular boxes, each of which covers an approximate temperature range along the X-axis and, magnetic field strength from $0.1B_H$ to $5B_H$ along the Y-axis (Not to be scaled). The middle of each rectangular box along the X-axis represents the peak line formation temperature. FUV spectral lines, having best estimated Stokes V signal, are shown using solid circles at a weak magnetic field strength of 10 G.

no spectral line with similar line irradiance and formation temperature to be used in association with Ly-α.

The O VI at 1037.61 Å and Ne VIII at 780.39 Å lines with $W_2 = 0$ can be used for zero polarization reference which may help in correcting for systematic artifacts. The Na IX at 681.72 Å can also be used together with Ne VIII at 770.42 Å but the number of photons is significantly less (close to a factor of 4). The combination of Ne VIII at 770.42 Å ($\log_{10}(T) = 5.9$, $B_H = 49$ G) and Mg X at 609.79 Å ($\log_{10}(T) = 6.0$, $B_H = 64$ G) is good to probe vector magnetic field from the regions of plasma with temperature in the range of $\log_{10}(T) = 5.9 - 6.0$. Both lines have good line irradiance. However, the wavelength separation is about 160 Å between these two lines. Nevertheless, there are two spectral lines, Ne VIII at 780.39 Å and Mg X at 624.94 Å, which can be used as zero polarization reference with this line combination.

Interestingly, Si IX at 694.69 Å has similar line irradiance as Na IX at 681.72 Å, but exhibit different sensitivity to Hanle effect, with $g_u\omega_B\tau = 1$ for 0.01 G and 58 G, respectively. Therefore, while Si IX 694.69 Å line is principally sensitive only to the field direction, Na IX 681.72 Å will be suited for determining the magnetic field strength.

There are several spectral lines in the wavelength range of 350 - 370 Å with $B_H = 100 - 180$ G which can be used to probe vector field from the regions with plasma temperature of $\log_{10}(T) = 6.1$ to 6.3. The greatest advantage here is that these lines are clustered within a wavelength band of about 20 Å which is beneficial in terms of instrument design and development. However, these lines have moderate number of photons compared to the lower temperature lines mentioned in the preceding paragraphs. At $\log_{10}(T) = 6.3$, there are two spectral lines which are best suited for vector magnetic field measurements, i.e., Al XI at 550 Å and Si XII at 499.4 Å, because both of these lines are close to each other in terms of wavelengths and also their B_H values which are 72 G and 82 G, respectively.

2.5 Conclusion

In this study, we have estimated the aforementioned parameters for the spectral lines in the wavelength range of 100 to 1600 Å to determine their Hanle sensitivity in the TR-coronal magnetic fields. We found that there are several permitted lines in EUV with different Hanle sensitivity in the temperature range of $\log_{10}(T) = 5.5 - 6.3$. A few FUV spectral lines were also examined in the context of providing additional constraints on the LOS component of the magnetic field vector. However, the use of FUV lines is limited by the large wavelength separation (for e.g., a passband of about 110 Å exists between 1349 Å and 1467 Å) between them. This implies that a single instrument based on the concept of Brewster's angle (as elaborated in the upcoming Chapter 4) cannot cover such a wide wavelength band due to variations in

the refractive index of the surface coating over this range.

The Hanle sensitivity of the spectral lines given in Figure 2.2 is limited to ≥ 4 G, with the exception of Si IX and Al X lines, having Hanle sensitivity from 0.001 to 0.05 G, which may be useful in probing very weak magnetic field in the milligauss range. This implies that the coronal height up to which most of the magnetic field measurements can be carried out is limited to $< 2R_{\odot}$. The impact of electron collisions becomes significant due to larger electron density at these heights. Therefore, detailed modeling of each individual line (shown in Figure 2.2) becomes important to estimate the effects of depolarizing collisions along with other symmetry breaking processes, such as non-radial solar wind, ion temperature anisotropy and presence of active regions (Fineschi *et al.*, 1993; Zhao *et al.*, 2019, 2021), on the real-time spectropolarimetric observations.

Chapter 3
FORWARD synthesis of EUV linear polarization

Extreme-ultraviolet Polarimetric Diagnostics of the Solar Corona: The Hanle Effect of Ne VIII *770 Å*
Raveena Khan, Sarah E. Gibson, Roberto Casini, K. Nagaraju, 2024, **The Astrophysical Journal**, 971, 27.

3.1 Introduction

Magnetic fields of the TR and the solar corona manifest in form of the structures of inhomogeneous and dynamic hot plasma observed in these layers. However, the formation and evolution of these structures are poorly understood, mainly due to the lack of routine measurements of the TR and coronal magnetic fields. To tackle these problems, there have been numerical modeling efforts that attempt to predict the TR and coronal magnetic structure through extrapolation from photospheric fields (Mackay and Yeates, 2012, and references therein). Observations of ubiquitous waves in the corona ('coronal seismology') have been used to provide synoptic measurements of the plane-of-sky (POS) component of the coronal magnetic field (Yang *et al.*, 2020a).

The application of the Hanle effect in the FUV and EUV spectral ranges is one of the potential methods to diagnose the weak magnetic fields of the TR and corona. Extensive theoretical studies have been performed in the FUV coronal lines, i.e., O VI 1032 Å (Sahal-Bréchot, Malinovsky, and Bommier, 1986; Trujillo Bueno, Landi Degl'Innocenti, and Belluzzi, 2017; Zhao *et al.*, 2019) and Ly-α 1215 Å (Bommier and Sahal-Brechot, 1982; Fineschi *et al.*, 1991; Hebbur Dayananda *et al.*, 2021). In Chapter 2, we have reported several electric-dipole (E1) transition lines in the UV with different sensitivity regimes to the critical Hanle effect. These lines can be exploited as potential diagnostics of the TR and coronal magnetic field vector (Fineschi *et al.*, 1993; Fineschi and Habbal, 1995).

A fairly recent work by Raouafi *et al.* (2016) used a 3D magnetohydrodynamic (MHD) model to derive the Hanle regime polarization signals in the solar corona (off-limb) in the FUV (H I Lyman-α) and the IR (He I 10830 Å) lines. Zhao *et al.* (2019, 2021) similarly examined the linear polarization of Lyman-α in the presence of both the Hanle effect and the symmetry-breaking process of Doppler dimming for 3D coronal MHD models. Hebbur Dayananda *et al.* (2021) used 3D coronal MHD models to investigate the linear polarization signals in the FUV (H I Ly-α at 1215 Å) and the EUV (He II Ly-α at 304 Å) lines within 0.5 $R_\odot$ above the Sun's visible limb. All these diagnostics assumed a coronagraph instrument to detect the off-limb coronal signal and its polarization unhindered by the disk radiation.

In the present study, we have utilized MHD simulation data cubes as inputs into the FORWARD code (Gibson *et al.*, 2016) and have synthesized the polarization maps both on-disk and off-limb. Among the Hanle sensitive lines listed in Table 2.1, Ne VIII 770 Å appears to be one of the brightest EUV lines. It has a line formation temperature of about 800,000 K and observed to be originating between the TR and the lower solar corona (Fludra *et al.*, 2021). Due to its significant polarizability and sensitivity to the Hanle effect over the expected coronal field strengths, the linear polarization of Ne VIII 770 Å has been simulated to illustrate its potential as a quantitative diagnostic of both magnetic field strength and field orientation in the POS (sometimes, also called field azimuth).

3.2 Methodology

The FORWARD SolarSoft IDL package is an extensive toolset consisting of various analytic magnetostatic equilibrium solutions, in the form of physical models and datacubes, the predictions of which can be compared with the observations. FORWARD also computes synthetic observables, such as the Stokes polarization maps produced by various scattering processes and the Hanle effect.

Predictive Science Inc. (PSI; refer to https://www.predsci.com/portal/home.php) have developed three-dimensional MAS (Magnetohydrodynamic Algorithm outside a Sphere) numerical simulations from the transition region to the inner heliosphere. The 3D MAS models provide us information of physical quantities such as magnetic field, density and temperature of the TR or coronal plasma. The second column of Figure 3.1 and the first column of Figures 3.3 and 3.4 represent the temperature and magnetic field maps of the MAS model, respectively, on the spherical "solar surface" lower boundary (circumscribed by the yellow circle) and continuing at the limb in the $X = 0$ plane out to $r = 2.0\ R_\odot$. On the disk, all the model maps are shown for a shell at 1.01 $R_\odot$ from where the LOS integrations of the observables are initiated.

The first column of Figure 3.1 represents the ion density maps of Ne VIII, a derived

quantity which has been calculated using the electron density and temperature from the MAS simulations, considering element abundances and ionization fractions of Ne VIII from the latest version 10.0 of the CHIANTI database (Dere *et al.*, 1997; Del Zanna *et al.*, 2021). On the disk, the Ne VIII ion densities are shown for the same shell at 1.01 $R_\odot$ as the temperature plots in the second column. We have shown MAS ion densities for points possessing simulation temperatures greater than 500,000 K (the base for the PSIMAS model; see Lionello, Linker, and Mikić 2001). Points with temperatures below this threshold are also excluded from the LOS integrals of intensity (column three of Figure 3.1) and linear polarization (columns two to four of Figures 3.3 and 3.4).

The MAS simulations used in this work are based on a 3D magnetohydrodynamic model which incorporates improved energy transport mechanisms such as coronal heating, radiative losses, Alfvén wave acceleration and parallel thermal conduction (Mikić *et al.*, 1999; Lionello, Linker, and Mikić, 2001). We have obtained MAS simulations for a time period of 11 years starting from the rising phase of the solar cycle 24 (SC24) until the rising phase of the solar cycle 25 (SC25). The eleven selected Carrington rotation (CR) simulations are CR2104, CR2118, CR2131, CR2144, CR2158, CR2171, CR2185, CR2198, CR2211, CR2225, and CR2238, which coincide with mid-December of each year from 2010 to 2020. We have then synthesized the LOS integrated spectro-polarimetric signals of Ne VIII 770 Å and studied the variation in the signals during the different phases of the solar cycles.

3.2.1 Polarization and Hanle sensitivity of Ne VIII

Polarization in the corona is mostly produced by the scattering of the anisotropic radiation from the underlying atmospheric layers of the Sun. In the case of atomic transitions, this anisotropic radiation induces population imbalance and quantum coherence among the atomic sublevels (mostly in the excited state), which cause the scattered radiation to be predominantly linearly polarized, even in the absence of magnetic fields. This linear polarization tends to be larger when the scattered direction is orthogonal to the direction of the incident radiation, as in the case of scattering by coronal structures off the limb (cf. Eqs (3.2) and (3.3). A simple geometry underlying the problem of radiation scattering in a magnetized plasma is shown in Figure 3.2. It tends instead to zero when the LOS approaches disk center (the case of forward scattering), unless other symmetry breaking mechanisms (such as an inclined magnetic field, or inhomogeneities of the solar radiation on the disk) introduce a preferential direction of linear polarization on the POS. When defining linear polarization, the reference axis for positive Stokes Q is taken as the radial direction from disk center through the scattering point.

The linear polarization of emission lines formed by scattering in a magnetized

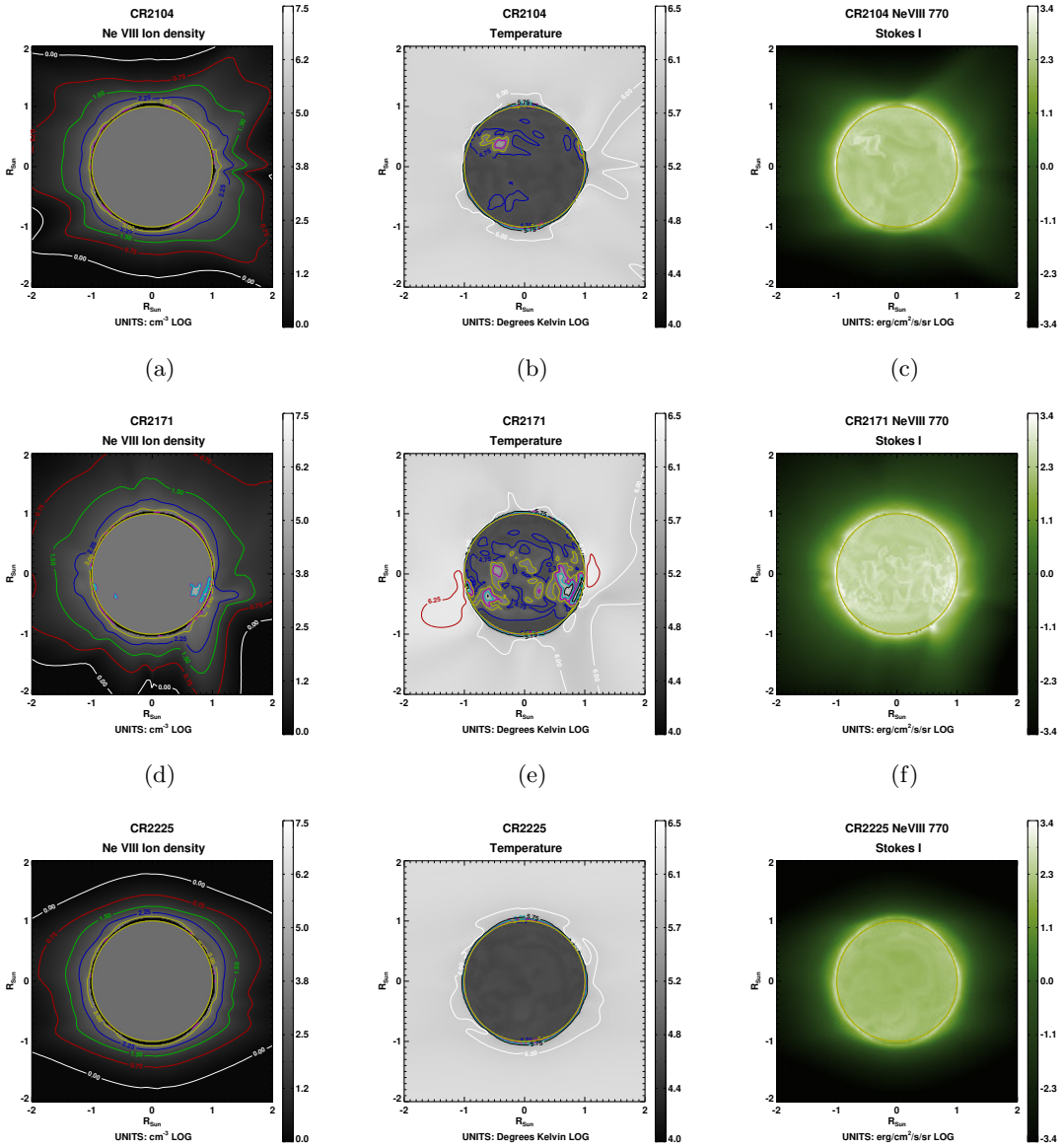

Figure 3.1: *Top row:* (a) derived Ne VIII ion density map, (b) PSIMAS model temperature map, and (c) synthesized Stokes I (LOS integrated) map during the rising phase (CR2104) of SC24. *Middle row* and *bottom row* illustrate the same maps, but during the maximum phase (CR2171) and the minimum phase (CR2225), respectively. Note that MAS coronal ion densities are not shown if simulation temperature is lower than 500,000 K at the plotted height (1.01 $R_\odot$ on the disk), and they appear grey (the color of the ion density corresponding to the assumed TR brightness below them; see Section 3.3.1). The yellow circle of radius 1 $R_\odot$ demarcates the circumference of the simulated solar surface. Contours of a particular color in a given map represent iso-curves of the depicted physical quantity shown in logarithmic scale. Note that Stokes I includes the contribution of collisional excitation to the scattered radiation.

plasma are most sensitive to the Hanle effect in the domain

$$0.1 \lesssim g_u \omega_B \tau \lesssim 10 \tag{3.1}$$

(e.g., Bommier, Sahal-Bréchot, and Leroy, 1981), where g_u is the Landé factor of the upper atomic level of the transition, ω_B is the Larmor frequency, and τ is the lifetime of the excited level. The condition $g_u \omega_B \tau = 1$ determines the so-called *critical* Hanle field strength. The resonance line Ne VIII 770 Å corresponds to the E1 transition between the two lowest atomic terms of the ion, $^2\mathrm{S}_{1/2}$ and $^2\mathrm{P}_{3/2}$. As derived in Chapter 2, the critical Hanle field (B_H) for this line is 49 gauss, and its *polarizability* coefficient is $W_2 = 0.5$ (computed using equations in Section 2.3.4).

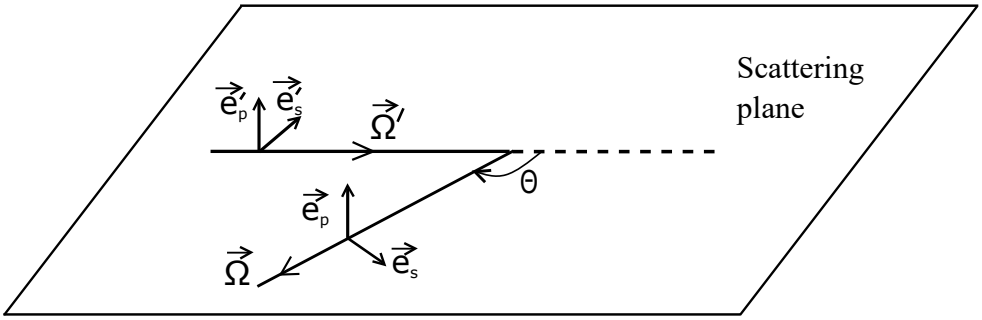

Figure 3.2: Geometry of a simple scattering event. The incident beam of unpolarized radiation propagating in $\vec{\Omega}'$ direction gets scattered in the direction $\vec{\Omega}$. The unit vectors $\vec{e_{p'}}$ and $\vec{e_p}$ perpendicular to the scattering plane $(\vec{\Omega}', \vec{\Omega})$ denote the reference direction of positive Stokes Q for the incident and the scattered beam, respectively. *Adapted from Figure 10.1 of Landi Degl'Innocenti and Landolfi 2004.*

The polarizability W_2 determines the maximum linear polarization by scattering attainable for a given transition. In fact, following Landi Degl'Innocenti and Landolfi (2004), in the absence of a magnetic field, the linear polarization produced in the scattering process depicted in Figure 3.2 is given by

$$\frac{Q}{I} = \frac{3W_2 \sin^2 \Theta}{4 - W_2 + 3W_2 \cos^2 \Theta}\,, \qquad \frac{U}{I} = 0\,, \tag{3.2}$$

and for $\Theta = 90°$, we get

$$\left(\frac{Q}{I}\right)_\mathrm{max} = \frac{3W_2}{4 - W_2}. \tag{3.3}$$

Therefore, the maximum scattering polarization for Ne VIII 770 Å (in the absence of magnetic fields) is $(Q/I)_\mathrm{max} \approx 43\%$.

3.2.2 Assumptions and Equations

In this section, we state the assumptions and equations used in calculating the line's polarized emissivity (Stokes I, Q, U). In the weak field approximation, we have considered a two-level atomic model having a lower unpolarized level* with $J_l = 1/2$ and an upper level with $J_u = 3/2$. This is a good approximation for the resonance line of Ne VIII at 770 Å. We also assume that the two-level atom is anisotropically illuminated by unpolarized and cylindrically symmetric (around the local solar vertical to the scattering ion) radiation field coming from the TR.

By considering an optically thin coronal plasma in the EUV, we have integrated the emission coefficients (i.e., equation (1) of Zhao *et al.* 2021) along the LOS to obtain the emergent signals for the Stokes parameters as

$$I_i(\mathbf{\Omega}) = \int_{LOS} \epsilon_i(\mathbf{\Omega}, s)\, ds \ , \tag{3.4}$$

where $i = 0, 1, 2$ refer to Stokes I, Q, U, respectively; s is the coordinate along the LOS; and $\mathbf{\Omega}$ is the propagation direction of the line emission. We have considered different values for the mean TR brightness that drives the radiative pumping of the Ne VIII 770 Å line, and which is responsible for the scattered radiation both on the disk and off the limb of the Sun. Evidently, this TR radiation must be added as a background intensity term to the LOS-integrated Stokes I signal given by Eq. (3.4), when observing on the disk.

We have also taken into account the contribution of collisional excitation to the Ne VIII 770 Å transition, which is responsible for a significant depolarization of the radiation emitted in the lower atmosphere, where the electron density is larger (see Figure 3.5 and caption therein).

3.3 Results and Discussion

In this section, we have considered CR maps describing three phases of the solar cycle, i.e., the rising, the maximum, and the end phase of SC24. The rest of the MAS model maps and the corresponding Stokes maps are shown in Appendix A.2. Using the MAS datacubes in FORWARD as explained in Section 3.2, we have simulated the linear polarization maps of the 770 Å resonance line, considering the presence of both magnetic fields and collisional excitation (Susino *et al.*, 2018).

Figures 3.1, 3.3 and 3.4 step through examples of the rising (*top row:* model CR2104), maximum (*middle row:* model CR2171) and minimum (*bottom row:* model CR2225) phases of SC24. The present section elucidates the changes in the following observables across the various phases of SC24:

*Unpolarized level refers to a non-degenerate level with negligible population imbalances and negligible quantum coherences between its magnetic sublevels.

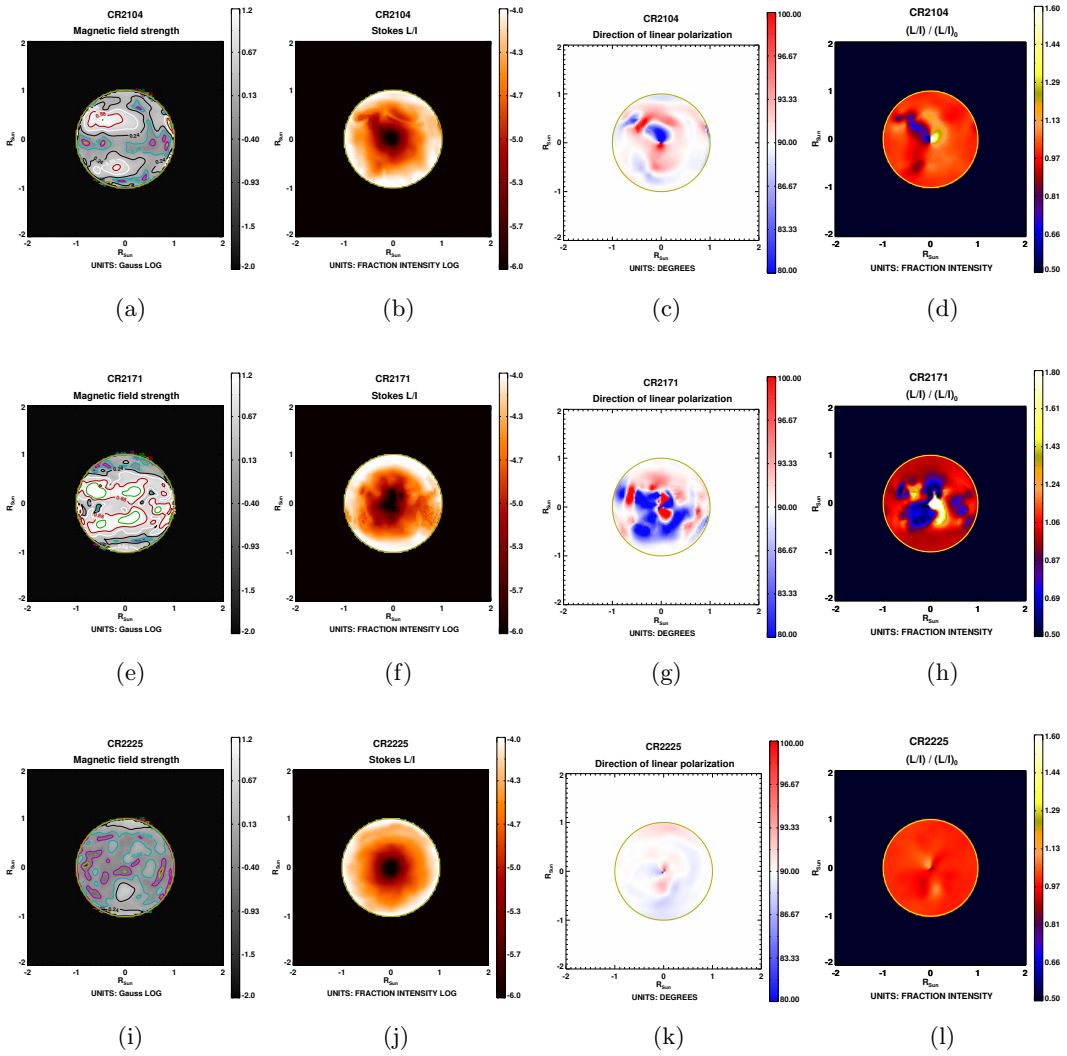

Figure 3.3: *Top row:* Rising phase (CR2104) of SC24: (a) PSIMAS model map of magnetic field, (b) LOS-integrated Stokes L/I in the presence of magnetic fields, (c) LOS-integrated linear polarization azimuth (relative to the radial direction through the point of calculation), and (d) synthesized ratio between LOS integrated L/I in presence and $(L/I)_0$ in absence of model magnetic fields. Only on-disk information within 1 $R_\odot$ is shown here. *Middle row* and *bottom row* illustrate the same maps, but during the maximum phase (CR2171) and the minimum phase (CR2225), respectively. Contours of a particular color in a given map represent iso-curves of the depicted physical quantity shown in logarithmic scale. Note that collisional excitation has been included here.

- the spectrally integrated coronal brightness, Stokes I (in $\mathrm{erg\,s^{-1}\,cm^{-2}\,sr^{-1}}$), shown in Figure 3.1 (third column);
- the degree of linear polarization, defined as $L/I = \sqrt{Q^2+U^2}/I$, shown in

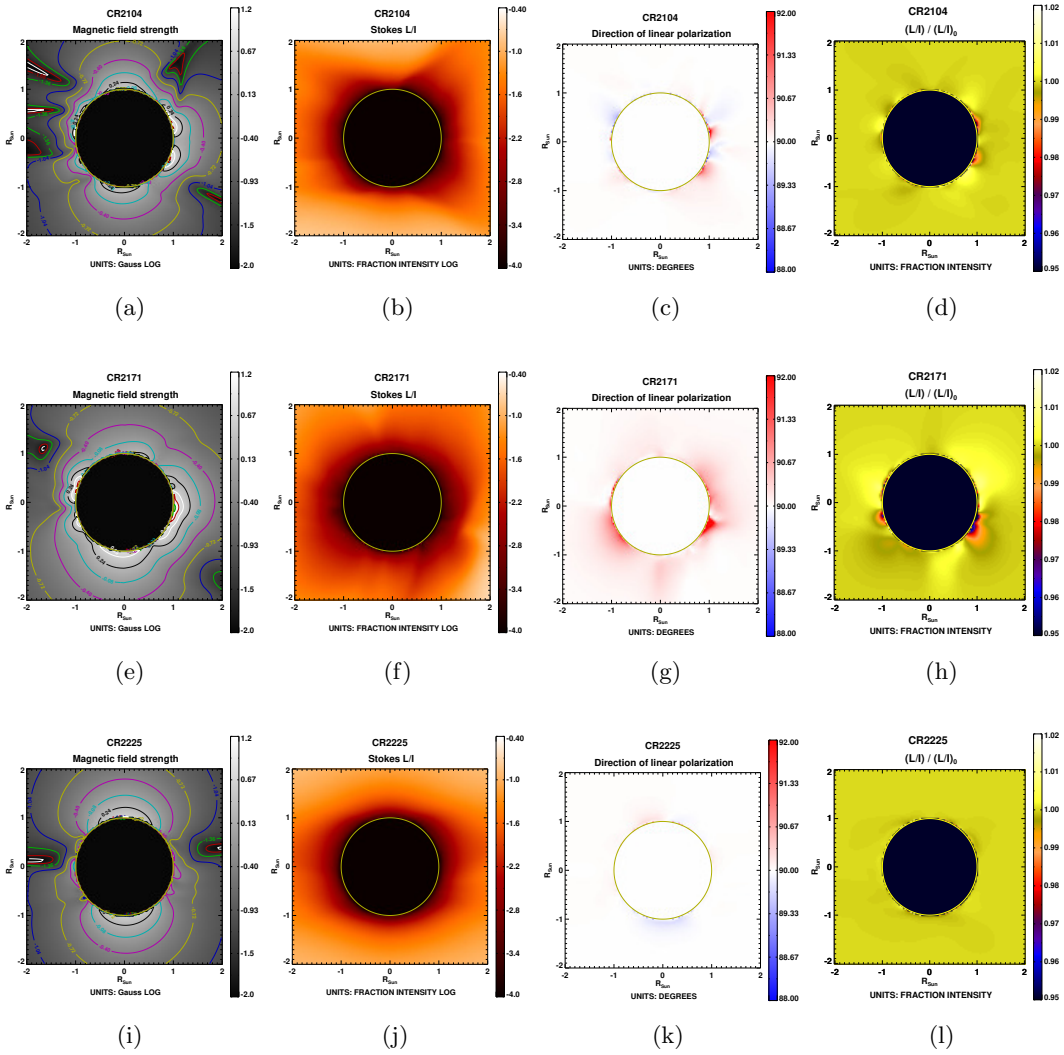

Figure 3.4: Similar maps as shown in Figure 3.3, with the solar disk masked in order to emphasize the off-limb scales.

Figures 3.3 and 3.4 (second column);

- the rotation angle of the plane of polarization, or polarization azimuth β shown in Figures 3.3 and 3.4 (third column); in FORWARD it is directly attained by using the two-argument form of the arctan function, $\beta = \frac{1}{2}\arctan(U, Q)$, with the additional folding of the negative branch $[-90°, 0°)$ to the positive branch via addition of 180°; this also ensures that the tangent to the limb in our maps corresponds to 90°, in order to reflect our choice of the reference direction for $Q > 0$ which is everywhere aligned with the radius vector from the disk center to the observed point.

- the ratio between linear polarization in a magnetized vs non-magnetized plasma

given in Figures 3.3 and 3.4 (fourth column).

3.3.1 Effects of TR brightness variations

We discuss here the impact of the pumping radiation change on the emitted intensity at Ne VIII 770 Å due to physical processes such as resonance scattering. As pointed out earlier in Section 3.1, this radiation comes from heights below the resonantly scattered coronal emission, and for Ne VIII 770 Å these heights correspond to the high TR and the lower corona (Fludra *et al.*, 2021).

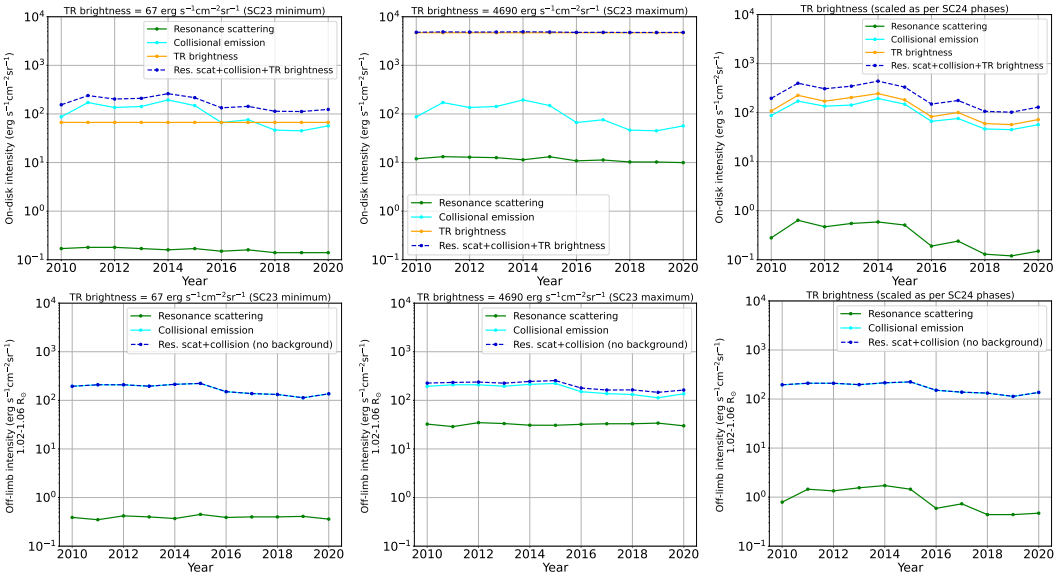

Figure 3.5: *Top row* and *bottom row* depict, respectively, on-disk Stokes I (median value) and off-limb Stokes I (median value between 1.02 and 1.06 $R_\odot$) as a function of SC24 period. *First*, *second* and *third* columns describe, respectively, the three cases of TR brightness, i.e., observed during SC23 minimum, SC23 maximum, and linearly scaled values as per the MAS simulations for SC24 and SC25. The Y-axis represents the intensity in logarithmic scale, while the X-axis covers the phases of SC24 and the beginning phase of SC25. Colored lines separate out the contributions from resonance scattering (green), collisional excitation (cyan), TR brightness (orange, on-disk), and the total of all sources of emissions (blue dashed). Note how the observed radiation on the disk is completely dominated by the TR brightness during peaks of solar activity (second column). Instead, the collisional component to the line radiation is always the dominant contribution to the brightness of the off-limb corona, so the visibility of its polarized component via resonance scattering is enhanced near solar maximum.

In the first column of Figure 3.5 (orange curve), we have assumed a TR brightness at Ne VIII 770 Å of 67 erg $s^{-1}cm^{-2}sr^{-1}$, based on Curdt *et al.* (2001) (Solar Cycle 23 (SC23) minimum phase). In the second column of Figure 3.5, we have chosen 4690 erg $s^{-1}cm^{-2}sr^{-1}$ from Sarro and Berihuete (2011), which corresponds to the average TR brightness observed during the maximum phase of SC23. In the third column,

we have linearly interpolated the TR brightness according to the median value of the full-disk collisional emission obtained from the MAS simulations for each of the phases of SC24 and also the beginning of SC25. We now explain the justification for the scaling of this interpolation.

Carrasco and Vaquero (2021) reported that the beginning of SC25 was similar to that of SC24, which was in turn weaker than SC23. Hence, we chose 57 erg $s^{-1}cm^{-2}sr^{-1}$ (taken as 15% lower than the above mentioned SC23 value of 67 erg $s^{-1}cm^{-2}sr^{-1}$ as justified by Didkovsky *et al.* 2010) as the TR brightness for both SC24 and SC25 minimum, and applied it to the year 2019. We further used linear interpolation, relating to the median value of collisional emission on the disk, to derive the TR brightness for the rest of the years from 2010 to 2020. We then analyzed how the variation of this radiation with solar cycle affects the signal on the disk (shown in the top row of Figure 3.5), and off the limb between a height of 1.02 $R_\odot$ and 1.06 $R_\odot$ (shown in the bottom row of Figure 3.5). In addition, we have calculated the LOS-integrated intensity above the disk considering only resonance scattering (green points) and only collisional emission (cyan points).

The effect of the mean TR brightness on the LOS-integrated linear polarization parameters (Stokes L/I and polarization azimuth), and the resulting SNR, are demonstrated by the synthetic polarization maps generated with the two extreme brightness values from the SC23 as shown in Figure 3.6. We have calculated the SNR on the linear Stokes parameters using Eqs. 7.15 and 7.16. A detailed derivation of these equations is given in Appendix A.1. Here, we have considered a telescope of aperture 50 cm with a throughput of 0.5% and a 32 arcsecond pixel. In order to calculate the maximum feasible time of integration on the disk of the Sun, let us consider to be observing a parcel of coronal plasma moving along the equator. Based on a synodic rotation rate at the equator of 26.24 days, this results in approximately 8 arcsecond displacement at disk center over 50 minutes for a feature at the solar surface. Assuming a (highly) conservative estimate of two solar radii for the highest coronal feature to be contributing to the LOS integral, the maximum smearing would be 16 arcseconds at disk center, roughly half a pixel, and hence tolerable.

By comparing between the right and left columns of Figure 3.6, we observe the drastic increase in the Stokes L/I signal, especially off the limb, and also notice the improved SNR (reduced green masked regions on the disk) in both Stokes L/I and azimuth maps. Due to such variability in the scattered radiation, it is not a good approximation to choose a single TR brightness value while forward modeling the Hanle regime signals for all phases of a particular solar cycle. However, in the absence of adequate observations at Ne VIII 770 Å to be able to include routinely observed TR brightness values throughout SC24 and SC25, we have scaled this radiation as a function of SC24 phases (shown in the third column of Figure 3.5), for use in our analyses of the Hanle polarization signal at Ne VIII 770 Å, as applied in the results

shown in Figures 3.1 to 3.4 and 3.7 – 3.8.

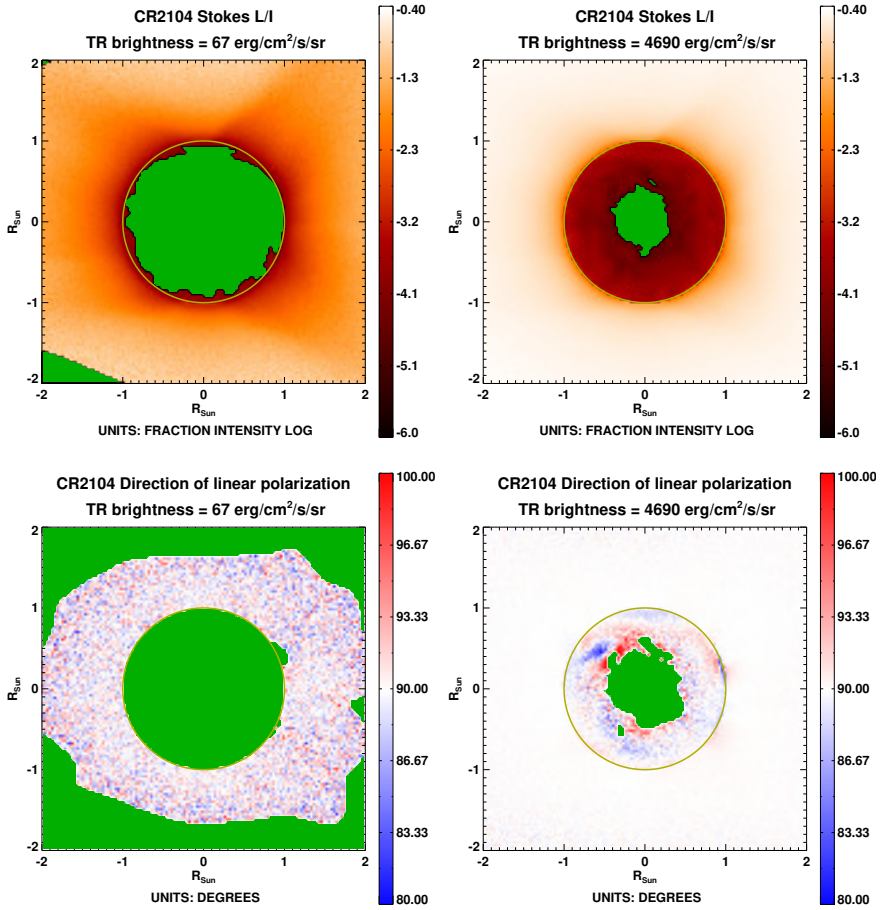

Figure 3.6: *Left column* and *right column* correspond to polarization maps considering a TR brightness of 67 erg cm^{-2} s^{-1} sr^{-1} (observed during SC23 minima) and 4690 erg cm^{-2} s^{-1} sr^{-1} (observed during SC23 maxima), respectively, for a telescope of aperture 50 cm, 30 arcsecond pixel size, instrument throughput of 0.5% and total integration time of 50 minutes. Green masked regions in azimuth maps indicate the areas where error on azimuth measurement is greater than $\pm 3°$, while in L/I maps they indicate areas where SNR on L/I is less than 5σ.

3.3.2 Variation with phases of the Solar Cycle

Figures 3.1(c), (f) and (i) depict simulated Stokes I maps for different phases across the entire SC24, including all of the contributary terms discussed in Section 3.3.1 and shown in Figure 3.5. As SC24 progresses, the total photon energy emitted (Stokes I) at Ne VIII 770 Å keeps increasing until SC24 reaches its maximum (Figure 3.1(f)), after which Stokes I decreases again until the end of SC24 (Figure 3.1(i)).

Similarly, the effect of the different phases of SC24 is observed on the degree of linear polarization. Figures 3.3 and 3.4 show the on-disk and the off-limb maps,

respectively. Panels marked (b), (f) and (j) describe the fractional L/I maps, while those marked (d), (h) and (l) describe the ratio between L/I in the presence of magnetic fields and $(L/I)_0$ in the absence of magnetic field.

As we proceed towards the maximum phase of SC24 (i.e., columnwise from Figure 3.3(l) to (d) to (h)), it is noticed that the overall contrast in fractional L/I on the disk increases with respect to the zero field case, owing to the increase in magnetic field strength and different field geometries along the LOS. In addition, there is an increased complexity of structures as opposed to the faint cylindrical structures visible in (l) and (d) (and in the equivalent magnetic structures in the first column of Figure 3.3).

The increase of the polarization contrast $(L/I)/(L/I)_0$ on the disk is easily explained, since the amplitude of scattering polarization goes to zero as one approaches the condition of pure forward scattering at disk center (under our simplifying hypothesis that the radiation field remains axially symmetric around the local vertical through the scattering point). Thus, the increased linear polarization is simply due to the presence of plasma structures harboring inclined magnetic fields generating polarization on top of a nearly zero background of scattering polarization.

In contrast, as the magnetic field strength intensifies towards the maximum phase of SC24, a notable decrease of polarization amplitude (i.e., the ratio $(L/I)/(L/I)_0$ becoming less than 1) is observed off the limb. This phenomenon is particularly evident in right-angle scattering, as the Hanle effect causes a reduction of the linear polarization induced by the radiation anisotropy, which reaches its maximum for 90° scattering.

The third column of Figure 3.3 shows the polarization azimuth across the disk, whereas Figure 3.4 shows the same quantity within the off-limb corona. The white regions on these maps indicate areas where the linear polarization is tangent to the nearest limb, which is consistent with the case of radiation scattering from E1 transitions in the absence of magnetic fields (Zhao *et al.* 2019). Conversely, in the presence of magnetic fields, the blue (red) regions show where the polarization direction tilts clockwise (counterclockwise) relative to the reference direction. The CR2225 simulation during the solar minimum (panel (k) of Figures 3.3 and 3.4) shows that the linear polarization of the scattered Ne VIII radiation remains along the tangent to the limb for most of the regions in the model, due to relatively weak magnetic fields. However, with the increase in magnitude of the magnetic field towards the rising phase (panel (c) of Figures 3.3 and 3.4) and the maximum phase (panel (g) of Figures 3.3 and 3.4) of the SC24, these red and blue regions become more pronounced, indicating greater deviations of the linear polarization vector from the reference axis.

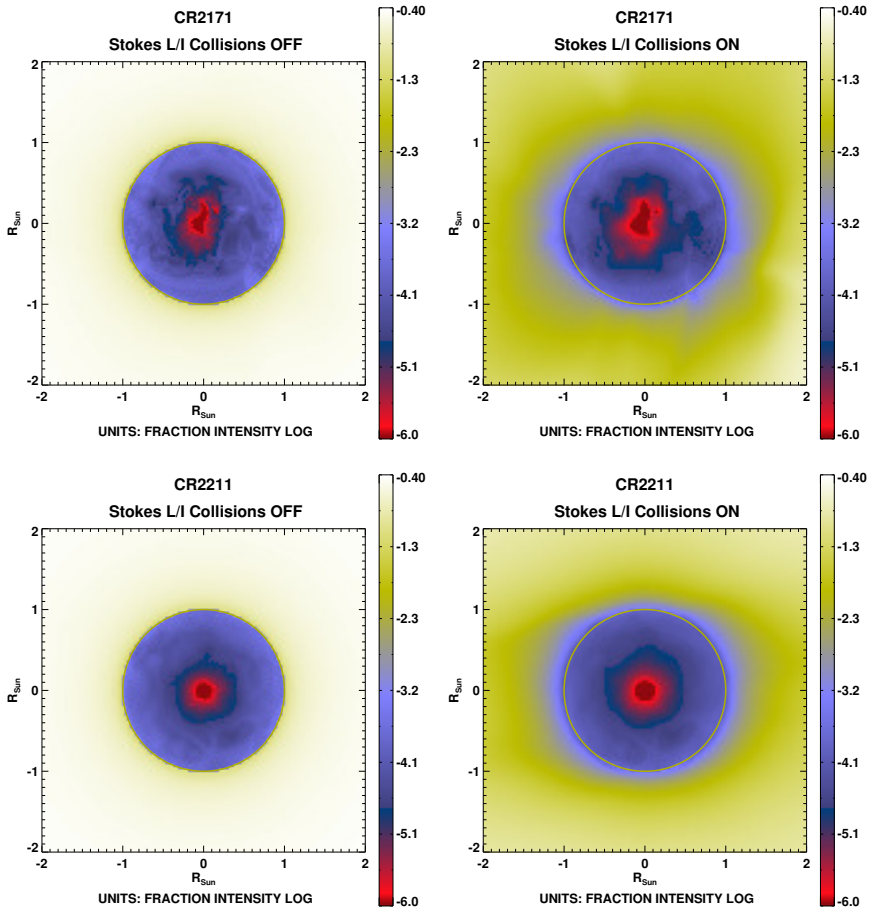

Figure 3.7: *Top row* and *bottom row* corresponds to the solar maximum and minimum phase of SC24, respectively. *Left column* shows linear polarization fraction (L/I) maps in absence of collisions, while *right column* shows L/I when collisions are switched on. SNR requirements are not considered here. Note a different color table is used for (L/I) than was shown in earlier figure, to enable visualization of limb and disk simultaneously.

3.3.3 Effect of collisional excitation

The electron collisional rates have been calculated using the analytical formula given in Susino *et al.* (2018), i.e.

$$C^e_{ij}(T) = 2.73 \times 10^{-15} \frac{f_{ij} g}{E_{ij} T^{1/2}} e^{\frac{-Eij}{k_B T}}, \tag{3.5}$$

where, C^e_{ij} is in cgs units, f_{ij} is the absorption oscillator strength for the considered transition, g is the average electron-impact Gaunt factor, E_{ij} is the transition energy, k_B is the Boltzmann constant and T is the electron temperature. The above formula

can be further simplified in terms of the collision strength. Hence, we can write

$$C^e_{ij}(T) = \frac{8.63 \times 10^{-6}}{\omega_i T^{1/2}} e^{\frac{-Eij}{k_B T}} \Omega_{ij}, \tag{3.6}$$

where, ω_i is the statistical weight of level i, and Ω_{ij} is the collision strength for the specified ion, its transition $i \rightarrow j$ and temperature. The collision strengths for Ne VIII line at 770 Å are obtained from the CHIANTI 10.0 version.

To visualize the effect of the collisional contribution to the emitted radiation, we consider the fractional linear polarization maps considering a model CR2171 from the solar maximum and a model CR2211 from the solar minimum of the SC24. Figure 3.7 shows the L/I signal for Ne VIII in the absence (left column) and presence (right column) of collisions. As can be seen from the right column of Figure 3.7, more areas of the Stokes L/I map darken in the presence of collisions. In general, collisions do not affect the linear polarization L due to their isotropic nature, but they increase the unpolarized intensity. Therefore, with the increase in collisions, the overall emitted intensity I – which is the sum of both polarized and unpolarized intensities – increases, thereby reducing the L/I signal.

The left column maps of Figure 3.7 illustrate a gradual change in the orientation of the LOS with respect to the local solar vertical, as we move from the disk center to the limb, which results in variation of Stokes L/I with maximum being at the limb of the model while negligible L/I around the disk center. In the right column maps of Figure 3.7, a relatively similar trend of increase in L/I is observed from disk center to the limb except that collisions result in lower value of L/I at each point as compared to the respective points in the left column maps. In addition, the coronal helmet streamer belt is clearly seen around the equator, with the characteristic dipolar structure typical of the solar minimum, and which manifests itself also through a similarly shaped depression of the L/I signal.

3.3.4 Signal-to-noise ratio in Ne VIII

In the previous sections, we have discussed the sensitivity of Ne VIII 770 Å to the Hanle effect across the entire SC24 and the beginning of SC25. Here we discuss the change in the required SNR during the various phases of the solar cycle for the detection of those polarization signatures. The instrument parameters considered here have been discussed in Section 3.3.1. For coronal modeling on the disk of the Sun, apart from the resonance line scattering intensity, we have accounted for an additional background intensity as explained in Section 3.2.2. We have then computed the SNR on the quantities Stokes L/I and azimuth (Az). Considering photon-noise limited polarization measurements, we have masked the regions on the Stokes L/I maps (shown as green shaded areas in the first and second columns of Figure 3.8) which have SNR of $\leq 5\sigma$. Similarly, the green masked areas on the azimuth maps (third

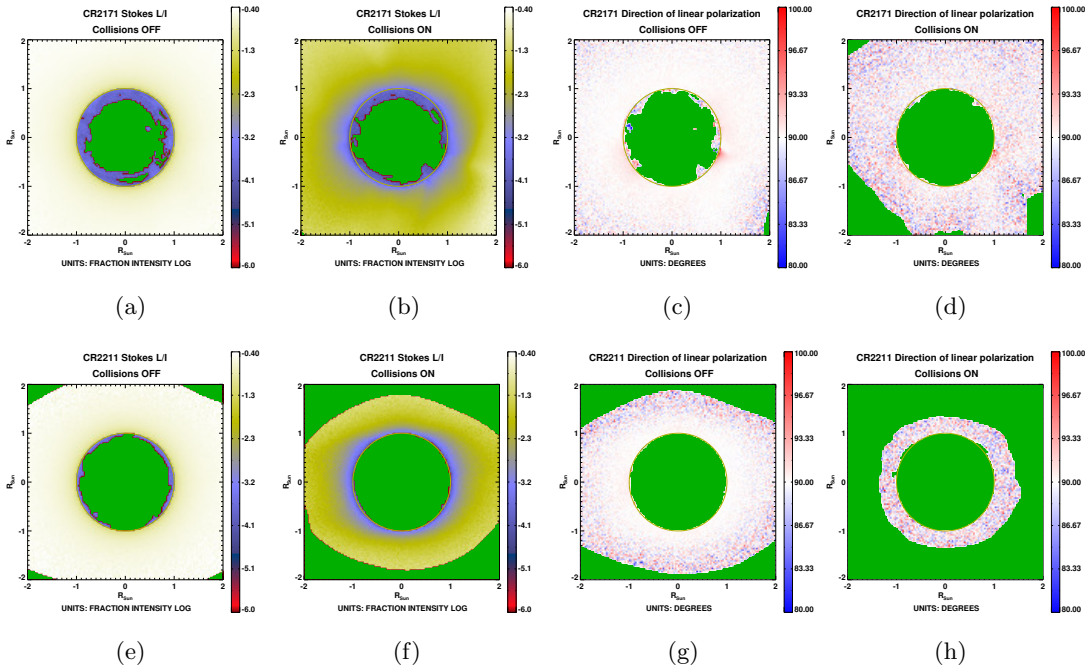

Figure 3.8: *Top row* and *bottom row* corresponds to the solar maximum and minimum phase of SC24, respectively. *First column* and *third column* show the maps without collisions, while *second* and *fourth* columns show the maps with collisions, for a telescope of aperture 50 cm, 30 arcsecond pixel size, instrument throughput of 0.5% and total integration time of 50 minutes. Green masked regions in azimuth maps indicate the areas where error on azimuth measurement is greater than $\pm 3°$, while in L/I maps they indicate areas where SNR on L/I is less than 5σ.

and fourth column of Figure 3.8) represent the points which have an error of greater than $\pm 3°$ in determining the direction of the linear polarization vector.

Considering the first and second columns of Figure 3.8, we observe how the area covered by the green shaded regions, where the SNR on Stokes L/I is below 5σ, increases in the presence of collisions. At the same time, there is a significant reduction in the off-limb polarization signal, adding significant complexity to the interpretation of the observed L/I in terms of magnetic sensitivity (as was also seen in Figure 3.7). In addition, we observe that the noise on L/I improves during the solar maximum phase (top row of Figure 3.8) as compared to the solar minimum phase (bottom row of Figure 3.8) due to the overall increase of the TR brightness (as was also seen in Figure 3.6). This implies that underestimating the pumping radiation at the spectral line considered can easily lead to under-calculating the SNR on the polarization signal.

Azimuth is independent of the collisional contribution to total intensity and this makes its interpretation in terms of magnetic sensitivity much more straightforward. However, collisions still affect the measurement error in determining the azimuth. Comparing between the third and fourth column maps in the top row of Figure 3.8,

we observe a trend of increase in the green shaded areas when collisions are turned on. Moreover, we note that there is lesser noise in the azimuth measurement during the maximum phase of the solar cycle (as seen in the third and fourth column maps in top row of Figure 3.8), while the error in azimuth measurement both on the disk and off the limb increases during the solar minimum (third and fourth column maps in bottom row of Figure 3.8) phase as the TR brightness reduces.

3.4 Conclusion

In this study, we have explored the possibility of using the EUV emission line Ne VIII 770 Å as a potential diagnostic for the coronal magnetic fields – both for the off-limb corona and on the disk. We have utilized the 3D thermodynamic models developed by the Predictive Science Inc. to simulate linear polarization maps, and study the change in the Hanle-regime polarization signals during the different phases of the solar cycle.

Further, we have performed a critical study of the effect of variation in the TR brightness on the scattered radiation at Ne VIII 770 Å. We have also examined the effect of collisions on the linear polarization and azimuth signals, and calculated the required SNR on these quantities. Although collisions have a significant impact on the Hanle polarization signals at all solar phases, we showed how the higher TR brightness characterizing the solar maximum helps achieve a larger SNR values in both Stokes L/I and azimuth. In particular, the azimuth values are not affected by the presence of collisional excitation, although the noise on their measurement is, because of the impact of its contribution to the intensity which affects the detectability of polarized signals.

The present study has also shown that Ne VIII 770 Å has the potential to be used as an overall coronal diagnostic without the need of a coronagraphic instrument. This EUV line is a useful complement to other coronal field diagnostics in the FUV, such as O VI 1032 Å and H I 1216 Å, which share comparable critical Hanle fields of about 35 gauss and 53 gauss, respectively. EUV coronal diagnostics can open a new era of non-coronagraphic measurements of the coronal magnetic field, and will complement other off-limb spectropolarimetric measurements in the visible and infrared wavelengths, such as those obtained with the Upgraded Coronal Multi-Channel Polarimeter (UCOMP; Tomczyk *et al.*, 2022) and the Daniel K. Inouye Solar Telescope (DKIST; Rast *et al.*, 2021).

There are other symmetry-breaking processes, including non-radial Doppler dimming and anisotropies in the kinetic temperature due to the solar wind, which could potentially impact scattering polarization (Zhao *et al.*, 2021). The Doppler dimming effect can arise in the presence of bulk motion of the scattering ions. When the incident radiation is dominated by line emission from the underlying atmosphere, the moving ions absorb radiation mostly from the line wings (i.e., away from the zero-

velocity line center), which is dimmer compared to the case of absorption by the ions at rest. Notably, when the bulk velocity direction is non-radial (as in the case of solar wind), Doppler dimming breaks the cylindrical symmetry around the local solar vertical of the incident radiation from the disk, as seen by the moving ions, thus leading to the modification of the linear polarization in the scattered radiation. Furthermore, the kinetic temperature anisotropy factor ($T_\perp/T_\parallel$) leads to a broader intensity profile in the perpendicular direction to the solar wind than in the parallel direction. Therefore, the linear polarization induced by the resonance scattering will be more reduced in the perpendicular direction, resulting in an asymmetry in the LOS integral, thereby causing a comparatively greater rotation of the polarization vector towards the perpendicular. Hence, it is important to incorporate these additional effects in the theoretical model of the atomic polarization, and quantify their influence on the Hanle polarization signal of the spectral line considered, particularly the narrower lines such as Ne VIII 770 Å and O VI 1032 Å.

Chapter 4
Design of an EUV spectropolarimeter

Design concepts of EUV polarimeter
Raveena Khan, K. Nagaraju, D.V.S. Phanindra, 2023, **SPIE proceedings**, Optics for EUV, X-Ray, and Gamma-Ray Astronomy XI, Volume 12679, id. 126790T, 7 pp.

Design requirements of a Spectropolarimeter for solar Extreme-ultraviolet Observations and characterization of K-mirror based on Brewster's angle
Raveena Khan, Radhika Dharmadhikari, Harsh Mathur, K. Nagaraju, Sinchana R. Jain, D.V.S. Phanindra, K. Sagayanathan, 2024, **Applied Optics**, *under revision.*

4.1 Introduction

Coronal magnetism lies at the heart of many long standing questions in solar physics, such as the problem of coronal heating, the acceleration source of the solar wind, and various eruptive events. Despite its importance, measurements of the coronal magnetic field have remained sporadic till date. The first detection of linear polarization at FUV line O VI at 1032 Å (a coronal emission line with peak line-formation temperature of about 400,000 K) was derived from the intensity measurements recorded during a manoeuvre of the SOHO satellite. By utilizing the instrumental polarization of the SUMER spectrometer, a magnetic field strength of approximately 3 gauss was derived above a coronal hole (Raouafi, Lemaire, and Sahal-Bréchot, 1999; Raouafi, Sahal-Bréchot, and Lemaire, 2002; Raouafi *et al.*, 2002). Even such an impromptu and unoptimized measurement of spectral line polarization underlines the promising capabilities of UV spectropolarimeters onboard upcoming space telescopes for acquiring critical magnetic field measurements in the solar corona.

UV solar spectrographs operational in the past include SUMER (Wilhelm *et al.*, 1995), UVCS (Kohl *et al.*, 1995) and CDS (Harrison *et al.*, 1995) aboard the SOHO. Currently, the SPICE (Fludra *et al.*, 2013) operates as a high-resolution imaging

spectrometer within two UV spectral bands: one ranging from 704 to 790 Å and the other from 973 to 1049 Å. Hitherto, there is no EUV spectropolarimeter for probing the coronal magnetic fields of the Sun. In this context, we have explored suitable coatings and various polarimeter concepts for operating in the EUV wavelength range.

The main criteria we have used in the selection of coatings for a polarimeter are high throughput and high polarizing power. Since there are no known optics with high transmissivity in the EUV spectral range, we have explored highly reflective and polarizing coating materials whose optical properties are relatively well known. The optical constants refer to refractive index (n) and extinction coefficient (k) of the coatings, which are obtained from Palik (1985, 1991). We have found that barium fluoride (BaF_2), magnesium fluoride (MgF_2) and lithium fluoride (LiF) are the suitable coatings with high refractive indices in the EUV spectral range as shown in Figure 4.1.

Reflecting surfaces with polarizing coatings (dielectric or metal) split the electric field vector of the incident beam of light into two components: parallel to the plane of incidence, called the s-component, and perpendicular to the plane of incidence, called the p-component. But when light of a particular wavelength is incident on a reflecting surface at the Brewster's angle, the reflected beam is optimally linear polarized, i.e., there is maximum reflectivity of the s-polarized component while the reflectivity of the p-polarized component is minimized. The Brewster's angle (Brewster, 1815) is calculated as

$$\theta_B = \tan^{-1}(n) \ , \tag{4.1}$$

where n is the refractive index of the surface coating at a particular wavelength. Since refractive index of a medium depends on the wavelength, the Brewster's angle also varies with refractive index. Hence, we have chosen a narrow spectral band of 740 to 800 Å in which there is no substantial change in the refractive index of the chosen fluoride coatings as shown in Figure 4.1. The aforementioned wavelength range constitutes pairs of Hanle sensitive lines such as, Mg IX at 749 Å and Ne VIII at 770 Å; Ne VIII at 770 Å and Mg VIII at 772 Å; Mg IX at 749 Å and Mg VIII at 762 Å, which can be suitably incorporated in the method of *differential* Hanle effect as proposed by Bommier, Sahal-Bréchot, and Leroy (1981). Additionally, this specific wavelength range is chosen to position Ne VIII at 770 Å as the central wavelength for designing an EUV spectropolarimeter and optimizing the coating parameters, which will be explained later in this Chapter.

4.2 ZEMAX analysis of polarimeter configurations based on mirrors

Initially, we designed a 1-mirror configuration in which we considered a glass substrate with an aluminium (Al) coating followed by a fluoride coating on top of it. Figure 4.2 shows an example of the sequence of coating layers on the glass substrate and

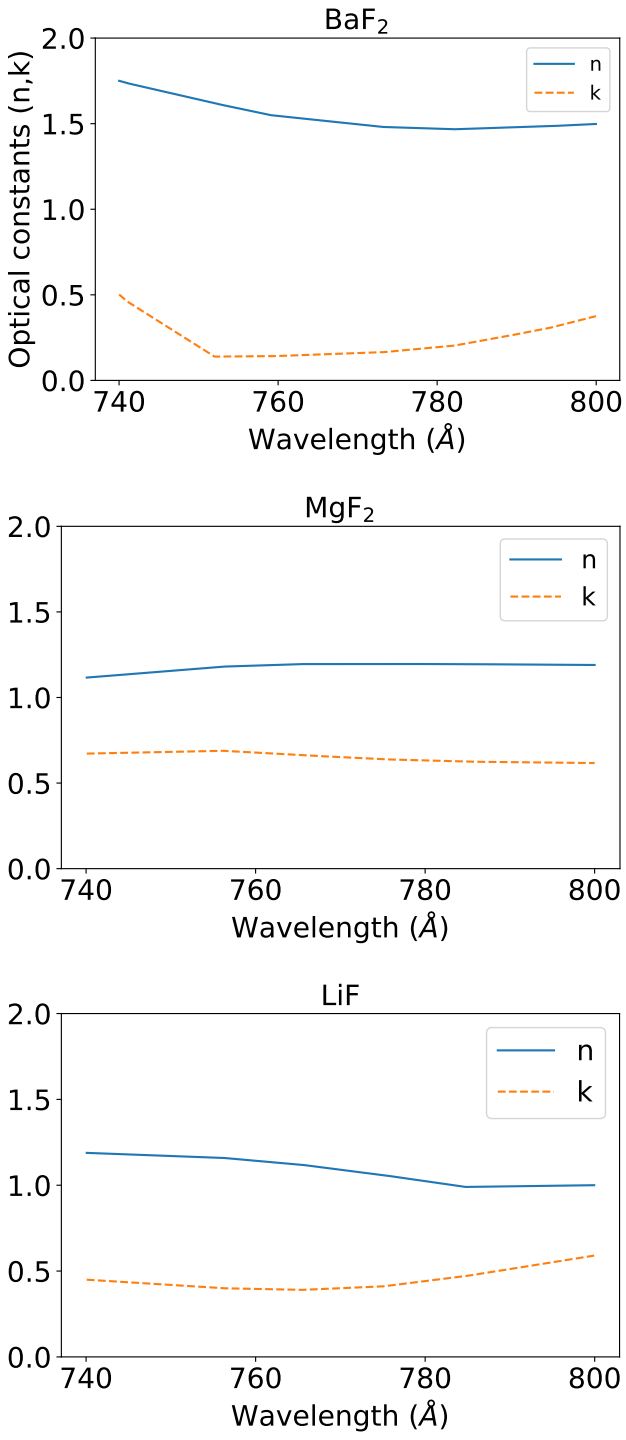

Figure 4.1: Optical constants of barium fluoride (top), magnesium fluoride (middle) and lithium fluoride (bottom) for the wavelength range 740-800 Å.

illustrates the concept of multiple reflections and transmissions occurring at each interface. Subsequently, we extended 1-mirror into a 2-mirror configuration as shown

in the left panel of Figure 4.3. In the 2-mirror configuration, the angle of incidence at each mirror is the same, i.e. β, which is equal to the Brewster's angle (θ_B). We further extended the design to include a third mirror (Robin, Kuebler, and Pao, 1966) in which α is the angle of incidence at mirrors **M1** and **M3**, while β is the angle of incidence at mirror **M2**. In the 3-mirror design, the angles of incidence at the three mirrors of the polarimeter follow the relation $2\alpha - \beta = 90°$ (Hass and Hunter, 1978). This condition ensures that the emergent beam from mirror **M3** follows the same path as the incident beam at mirror **M1**.

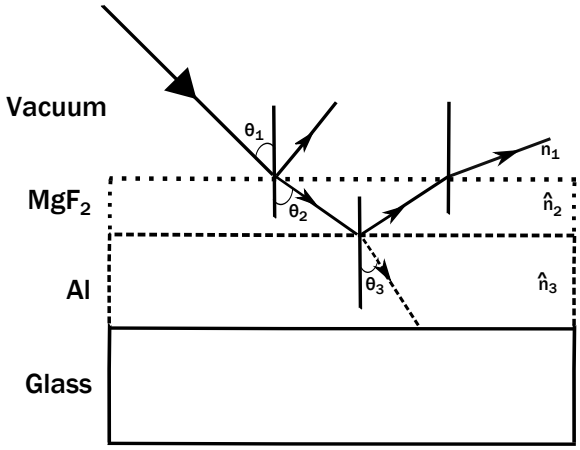

Figure 4.2: Graphical representation of the sequence of various coating layers on a glass substrate. $\hat{n_2}$ and $\hat{n_3}$ are the complex refractive indices $(n + ik)$ of the materials MgF_2 and Al (Not to scale).

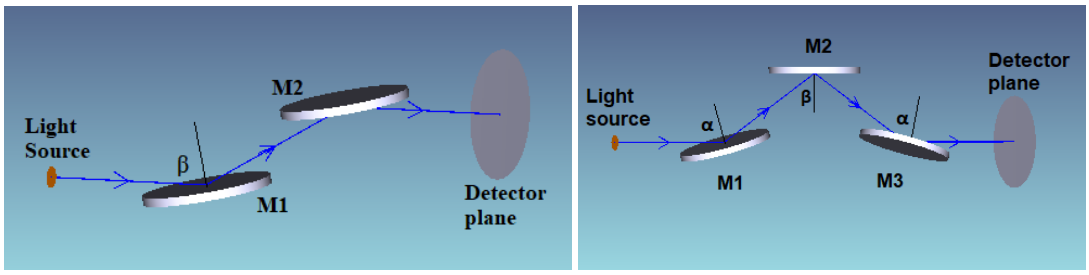

Figure 4.3: Schematic diagram showing (left panel) a 2-mirror based polarimeter setup, and (right panel) a 3-mirror-based polarimeter setup.

The polarizing power of a reflecting surface is defined as

$$P = \frac{R_s - R_p}{R_s + R_p} \ , \tag{4.2}$$

while throughput is defined as

$$T = R_s + R_p \ , \tag{4.3}$$

where R_s is the reflectivity for the component of the electric field vector perpendicular to the plane of incidence (s-polarized light), while R_p is the reflectivity for the parallel component (p-polarized light).

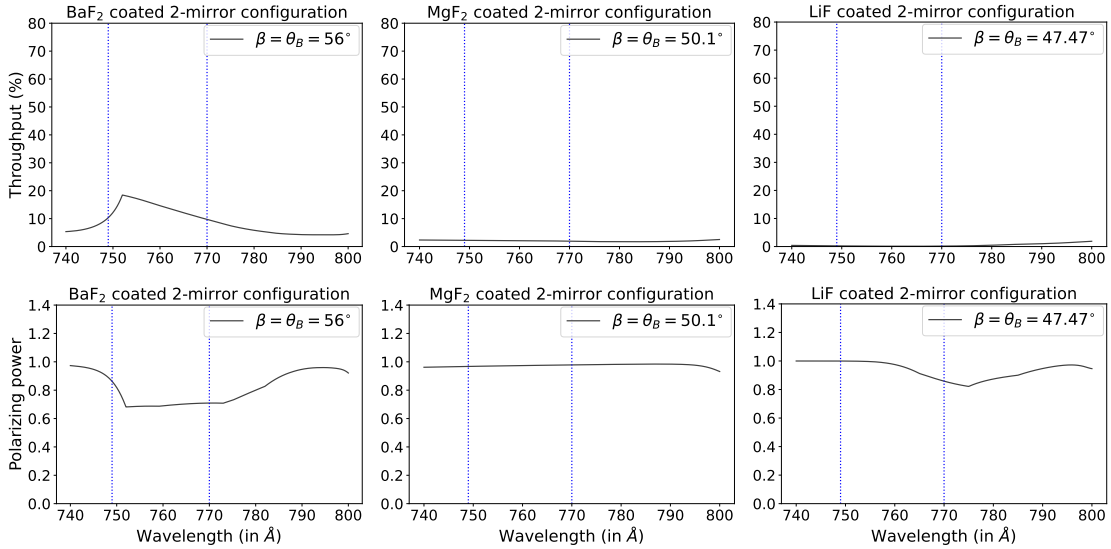

Figure 4.4: Top row shows throughput vs wavelength, while bottom row shows polarizing power vs wavelength, for a 2-mirror polarimeter coated with BaF_2 (first column), MgF_2 (second column) and LiF (third column). The blue dotted lines indicate Mg IX at 749 Å and Ne VIII at 770 Å.

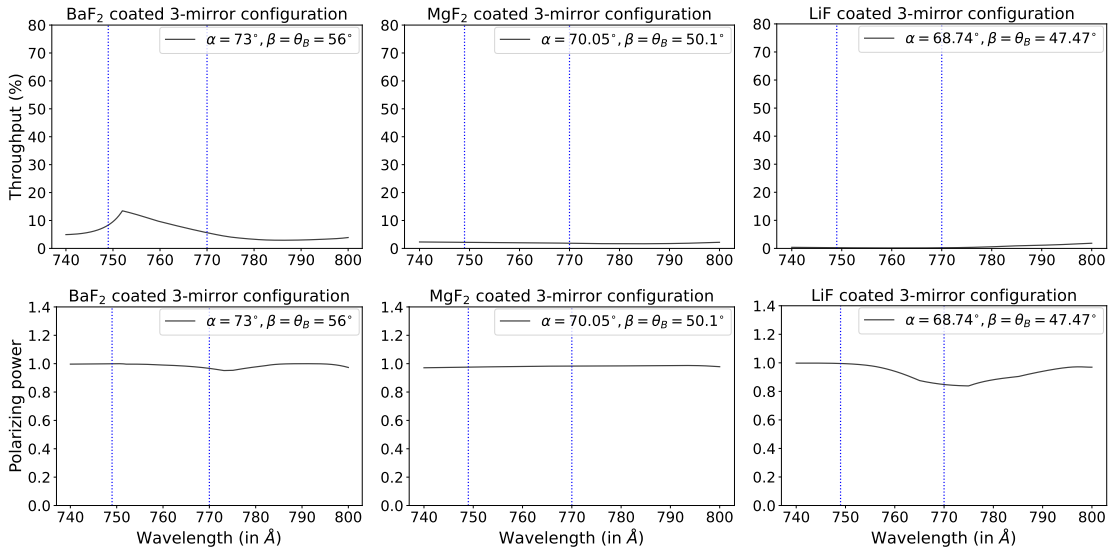

Figure 4.5: Similar plots as shown in Figure 4.4, but for a 3-mirror polarimeter configuration.

The reflectivity of s-polarized and p-polarized light at each mirror is derived from ZEMAX. The total reflectivities, R_s and R_p, for a given polarimeter configuration, are

determined by multiplying the reflectivities of s-polarized and p-polarized light at each mirror surface. The polarizing power and the throughput are then calculated using Eqs. 4.2 and 4.3, respectively. These values are plotted as functions of wavelength for 2- and 3-mirror configurations, as illustrated in Figures 4.4 and 4.5. The blue dotted vertical lines indicate two Hanle sensitive lines, i.e. Mg IX at 749 Å and Ne VIII at 770 Å.

We have analyzed and compared the throughput and the polarizing power between the two polarimeter configurations by considering the same (absolute) coating thickness on all the mirrors. It was found that BaF_2 provides a better throughput of approximately $10 - 20\%$ for both 2- and 3-mirror configurations, whereas MgF_2 and LiF reflect less than 4% at the desired wavelengths (see top row in Figures 4.4 and 4.5). Additionally, there is improvement in the polarizing power of BaF_2 in the 3-mirror model (compare bottom rows of Figures 4.4 and 4.5). Therefore, BaF_2 is preferred as a coating material due to its higher throughput compared to MgF_2 and LiF. Furthermore, the BaF_2 coated 3-mirror model is advantageous over the corresponding 2-mirror model in terms of its higher polarizing power.

4.3 Design of EUV spectropolarimeter (SPOLEO) using ZEMAX

In this section, we discuss the design of a SpectroPOLarimeter for Extreme-ultraviolet Observations (SPOLEO; see Figure 4.6) of the TR and corona. The SPOLEO design incorporates a 3-mirror-based polarimeter, chosen for its advantages discussed in Section 4.2, integrated with a high-resolution spectrograph similar to the design principles used in the SUMER spectrometer (Wilhelm *et al.*, 1995). Additionally, we have increased the telescope aperture to a 50 cm off-axis parabolic mirror for enhancing the instrument's capability to achieve the required polarization sensitivity levels.

4.3.1 Design Concepts

The optical arrangement includes reflective parabolic mirrors (a telescope primary mirror and a collimator), a 3-mirror-based polarimeter (also named as K-mirror polarimeter) and a spherical concave grating. In addition, an aperture stop is positioned before the telescope primary mirror – an off-axis parabola with a focal length of 1320 mm. A slit is placed at the focal plane of the telescope. The divergent beam from the slit illuminates the collimator which is an off-axis parabolic mirror with a focal length of 172 mm. A Lyot stop is placed, prior to the polarimeter, in order to block the diffracted light from the collimating and primary mirrors. The collimated beam, after reflection from the polarimeter, is incident onto a spherical concave grating (used in the first diffraction order) which acts as an imager. We have used a grating of 4000 grooves/mm, similar to the spherical concave grating which was demonstrated on the

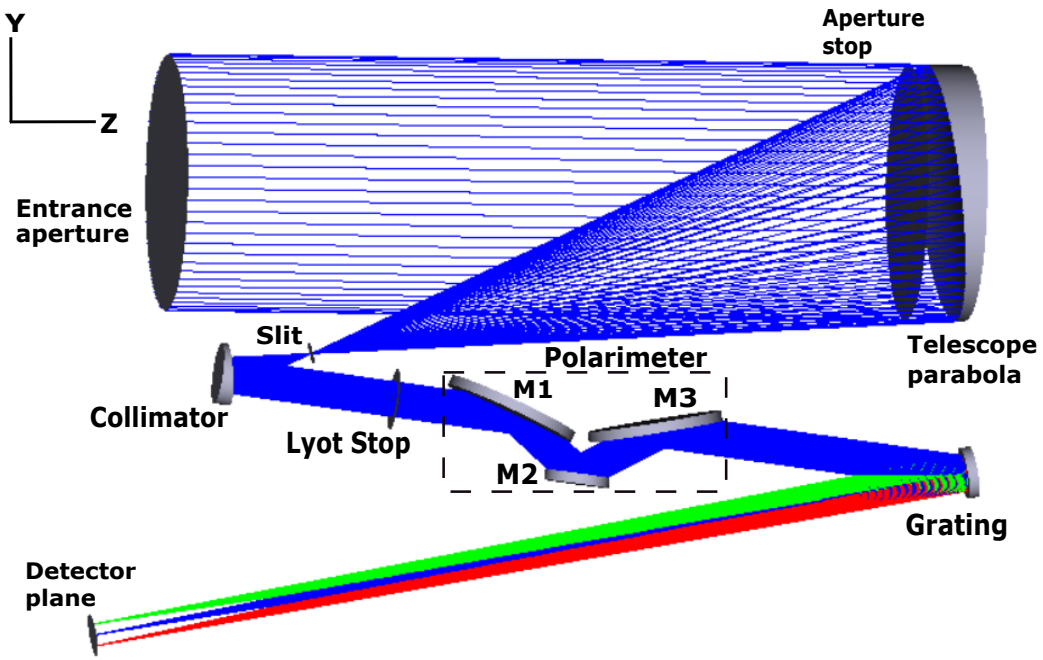

Figure 4.6: Design layout of SPOLEO instrument using ZEMAX.

SUMER spectrometer for about a decade of solar observations in the EUV spectral range of 470 to 1609 Å (Wilhelm *et al.*, 1995). A two-dimensional detector array, with 1024 (spectral) by 1280 (spatial) pixels, has been considered at the focal plane of the grating. The optimized parameter values of the optical components are given in Table 4.1.

Figure 4.7 illustrates the performance of the optimized instrument at the three wavelengths of the design – the lowest wavelength at 740 Å, the central wavelength at 770 Å and the highest wavelength at 800 Å. The radius of the airy disk, as shown by the dashed circle, measures about 2.44 μm. We observe that the optimized design achieves a diffraction-limited resolution. If we consider each pixel size equal to 15 μm, a detector with 1024 pixels (linear dispersion of 0.021 Å/pixel) along the spectral direction is required to accommodate a pair of Hanle sensitive lines which are about 21 Å apart (for e.g., Mg IX at 749 Å and Ne VIII at 770 Å). In the design of the instrument, we have chosen a slit width (at which the fraction of enclosed energy is maximum) of 1″ and length of 0.24″ in the no-binning case. As calculated in Appendix B.1, the photon fluxes at Ne VIII 770 Å expected during the two extreme phases of solar cycle 23 are presented in Table 7.1.

In the SPOLEO design, the polarimeter (contained in a dashed outlined box in Figure 4.6) consists of three reflective mirrors **M1**, **M2** and **M3** which are designed as glass (fused silica) substrates with aluminium (Al) coating followed by BaF_2 coating on the surface. The angle of incidence (α) at mirrors M1 and M3 is 73°, while

Table 4.1: Optical prescription of the SPOLEO optics

Parameter	Value
Telescope parabola:	
Entrance pupil	500 mm
Focal length	1302.77 mm
Off-axis angle	14.21°
Plate scale at slit plane	158.33″/mm
Slit:	
Width	1″
Lengths	32″, 300″
Collimator parabola:	
Focal length	172.25 mm
Off-axis angle	20.09°
Diameter	12 cm
Concave grating:	
Curvature radius	3509.52 mm
Groove density	4000 grooves/mm
Focal length	1803.28 mm
Angle of incidence (w.r.t. grating normal)	18.52°
Detector:	
Plate scale	0.24″/pixel
Pixel size	15 μm
Array dimensions	1024 × 1280 pixels
Linear dispersion	0.021 Å/pixel
LSF FWHM	0.09 Å $\equiv 65\mu m$
Resolving power	8220 - 8890 @ 740 – 800 Å
System efficiency	4.92%

the angle of incidence (β) at mirror M2 is 56°, which is equal to the Brewster's angle at 770 Å. As observed in Figure 4.5, BaF_2 is a highly polarizing coating with better throughput in the wavelength range of 740 to 800 Å. The glass (fused silica) substrates of remaining optical elements are coated with magnesium (Mg) followed by silicon carbide (SiC). Mg/SiC coated mirrors exhibit a long-term stability and constant reflectivity up to a temperature of 300°C (Pelizzo *et al.*, 2012; Takenaka *et al.*, 2005). In addition, Mg/SiC has higher reflectivity ($\sim$ 40%) in the EUV spectral range, whereas it transmits ($>$ 70%) the longer wavelengths (visible and infrared) further reducing the unwanted radiation. Another primary aspect of the SPOLEO design is the thickness of coatings used on each of the reflective components. Hence, we have optimized the material thicknesses which is discussed in Section 4.4.

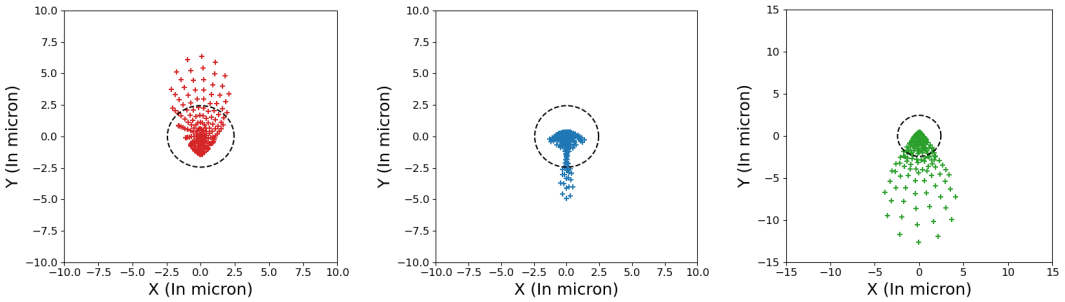

Figure 4.7: Spot diagram at lowest design wavelength 740 Å (*left panel*), central wavelength 770 Å (*middle panel*), and highest design wavelength 800 Å (*right panel*). Dashed circle encloses the airy disk.

4.3.2 Key considerations

Ne VIII 770 Å is one of the brightest lines among all the Hanle sensitive lines in the EUV as listed in Table 2.1. Most importantly, it exhibits a line-formation temperature of approximately 800,000 K, which is higher compared to the other brighter emission lines, such as O VI at 1032 Å and H I at 1216 Å. Such elevated temperature sensitivity suggests that Ne VIII originates between the TR and the lower solar corona (also reported by Fludra *et al.*, 2021), making it well suited for the TR and coronal magnetic field measurements. Ne VIII 770 Å corresponds to E1 transition and the linear polarization of an E1 line is sensitive to both magnetic field strength and field orientation in the plane-of-sky (POS), as observed in Chapter 3. This implies that measurements of the degree of linear polarization (Stokes L/I, where $L = \sqrt{Q^2 + U^2}$) and the rotation angle of the plane of polarization (Stokes $\beta = \frac{1}{2}\arctan(U/Q)$) can aid in deriving the complete magnetic field vector.

The average on-disk quiet Sun flux at Ne VIII 770 Å fluctuates between different phases of the solar cycle. Consequently, we consider two distinct flux scenarios: one observed during the maximum phase with a value of 4290 ph $\mathrm{cm}^{-2}\mathrm{s}^{-1}\mathrm{arcsec}^{-2}$ (Sarro and Berihuete, 2011), and another observed during the minimum phase of SC23 with a value of 61.29 ph $\mathrm{cm}^{-2}\mathrm{s}^{-1}\mathrm{arcsec}^{-2}$ (Curdt *et al.*, 2001). Assuming the EUV intensity measurements are photon-noise limited (with no background photons) which follow the Poisson statistics, the noise in an intensity measurement is given by $\sigma_I = \sqrt{I}$, where I is the photon counts of the peak line intensity.

From the FORWARD modeling of Ne VIII 770 Å, Stokes L/I is estimated to be in the orders of 1×10^{-4} at the solar limb region. Therefore, detection of polarization sensitivity in these levels is an essential requirement which has driven the design of SPOLEO. Considering $P = L/I \sim 1 \times 10^{-4}$, the level of sensitivity σ_P that can be achieved on the measurement of P using the specified instrument, can be derived

using Eq. 7.4 as

$$\sigma_P = \frac{\sigma_I}{I}\sqrt{P^2 + \frac{\epsilon_I^2}{\epsilon_{Q,U}^2}} = \frac{1}{SNR}\sqrt{P^2 + \frac{\epsilon_I^2}{\epsilon_{Q,U}^2}}\,, \tag{4.4}$$

where where ϵ_I, ϵ_Q, ϵ_U are efficiencies for Stokes I, Q, U, respectively. While the optimized design achieves a diffraction-limited resolution (shown in Figure 4.7), our primary objective is to achieve polarimetric precision that enables the detection of Hanle polarization signals in the orders of 10^{-4}. Using above Eq. 4.4, we have examined the variation of the polarization sensitivity (as shown in Figure 4.8) for different telescope apertures (top panel) and integration times (bottom panel). We observe that for a 50 cm telescope aperture, better sensitivity levels can be acquired during the maxima phase of SC23 (as shown by the blue curves), due to increase in the photon flux at Ne VIII 770 Å compared to that acquired during the minima phase (as shown by the red dashed curves). As seen from the bottom panel of Figure 4.8, these sensitivity levels can further be enhanced by increasing the integration time.

We further investigated the effect of different spatial sampling on the polarization sensitivities, as illustrated by different markers in Figure 4.8. In the top panel, we observe that during the minimum phase of SC23, a minimum spatial sampling of 32″/pixel (represented by maroon asterisk on the red dashed curves) is required to achieve polarization sensitivity of around 10^{-4} over shorter integration time of 5 minutes. However, during the maximum phase, a spatial sampling of 6.4″/pixel (represented by yellow circle on the blue solid curves) is sufficient to achieve sensitivities better than 10^{-4} over the same integration time. Furthermore, in the bottom panel of Figure 4.8, we demonstrate that the previously mentioned sensitivity levels can be further enhanced to the order of 10^{-5} for longer integration times. Therefore, the detection capability of the instrument can be upgraded beyond the typical signal levels of 10^{-4}, and allow observations of a wide range of science targets ranging from dynamic events of a few minutes, such as coronal jets, coronal mass ejections (CMEs), to long-lived structures on the Sun, such as coronal holes and coronal fans, which can persist for several Carrington rotations (Mierla *et al.*, 2010; West *et al.*, 2022).

To meet the desired spatial sampling of 6.4″/pixel and 32″/pixel, we need to apply spatial binning techniques. Approximately 27 and 134 pixels (with pixel pitch of 15 μm) must be spatially binned to attain the required sampling of 6.4″/pixel and 32″/pixel, respectively, with the current instrument parameters. In order to enable larger spatial sampling of 32″/pixel, a longer slit needs to be selected which will also facilitate the acquisition of the desired levels of polarization sensitivity. Therefore, a 1024×156 detector with 156 spatial pixels will be required to accommodate a slit length of about 32″. However, an even longer slit of about 300″ will aid in observing the large-scale structures, such as coronal holes, which will then require a 1024×1280 detector with 1280 spatial pixels.

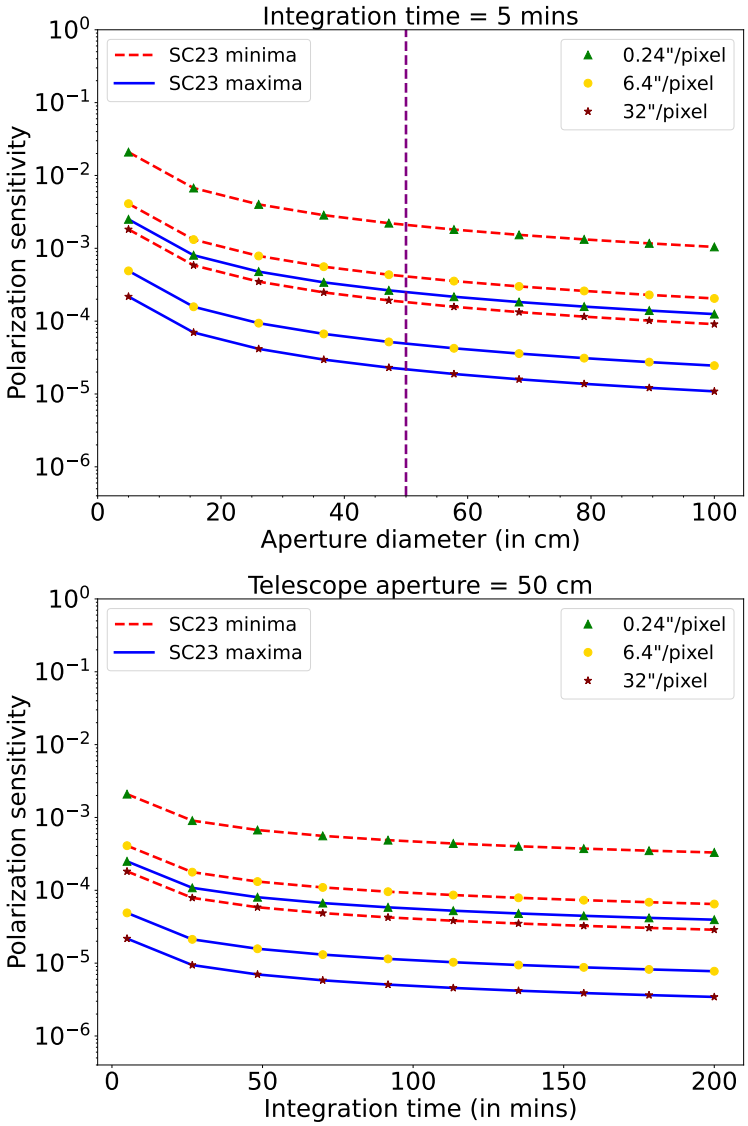

Figure 4.8: Sensitivity σ_P on linear polarization degree, as a function of telescope aperture (*top panel*) and integration time (*bottom panel*), during the maxima (blue curves) and the minima (red dashed curves) phases of SC23. Different spatial samplings considered are $0.24''$/pixel (green triangle), $6.4''$/pixel (yellow circle) and $32''$/pixel (maroon asterisk). Dashed purple vertical line in the top panel indicates 50 cm telescope aperture diameter of SPOLEO.

4.4 Results and Discussion

In this section, we discuss the performance of the instrument design in terms of coating thickness and thermal analyses of the components. We also provide an error budget of tolerances to be allowed on the optical components so as to remain within the limit of achieving the scientific objectives.

4.4.1 Optimization of coating thickness

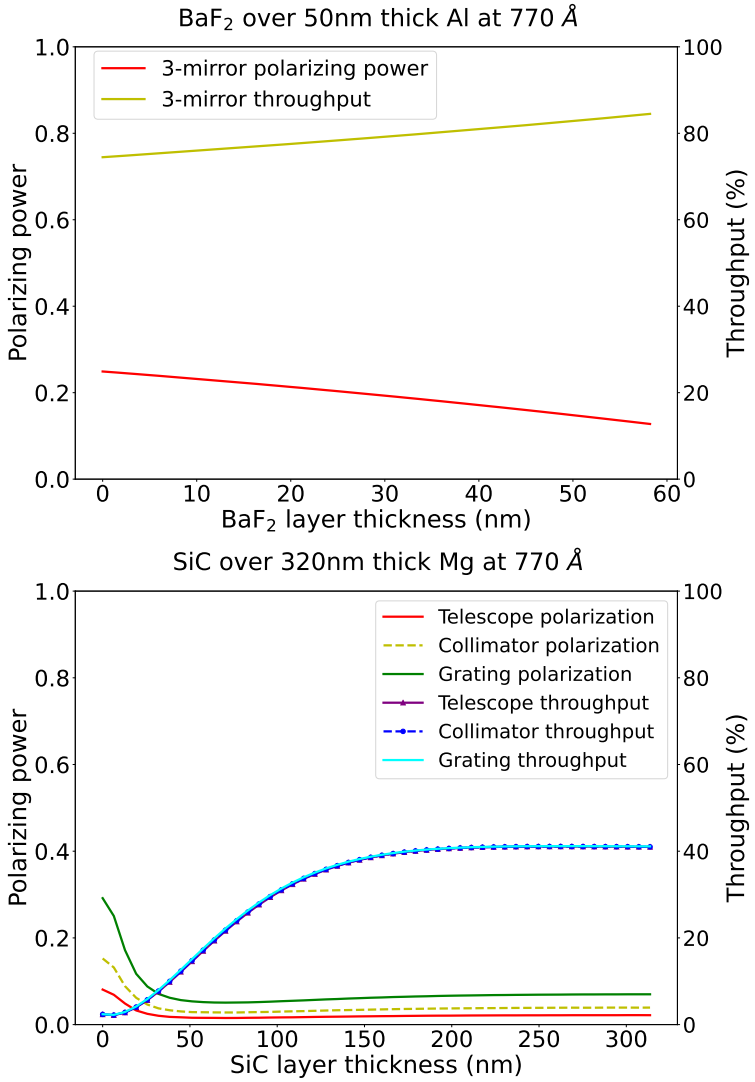

Figure 4.9: *Top panel* shows polarizing power and throughput of K-mirror polarimeter for different thickness of BaF_2 coating over 50nm thick Al. *Bottom panel* shows polarizing power and throughput of rest of the components (telescope, collimator and grating) for different thickness of SiC coating over 320nm thick Mg. All plots are shown for the central wavelength of 770 Å. Note that the throughput curves of the telescope (purple), the collimator (blue) and the grating (cyan) are largely overlapping with each other.

The thickness of the coatings and their complex refractive indices, especially in shorter wavelengths such as EUV, affect the throughput and the polarizing power of the optical system. We wrote a ZPL macro in Zemax to generate a coating polarization report for various combinations of material thickness at the central wavelength of 770 Å. This method was used to examine the impact of BaF_2 coating thickness varia-

tion over different Al thicknesses for the K-mirror polarimeter. We observe that as the thickness of the BaF_2 coating increases, the polarizing power gets reduced but there is an increase in the throughput (as depicted in the top panel of Figure 4.9). Hence, it is crucial to select an optimal BaF_2 coating thickness that maximizes the polarizing power without significantly reducing the throughput of the polarimeter, thereby not compromising the scientific objectives. Balancing between polarizing power and throughput, we opted for a 14 nm thickness of BaF_2 over 50 nm Al, and computed the polarizing power and the throughput for the design wavelength range of 740 to 800 Å (Figure 4.10).

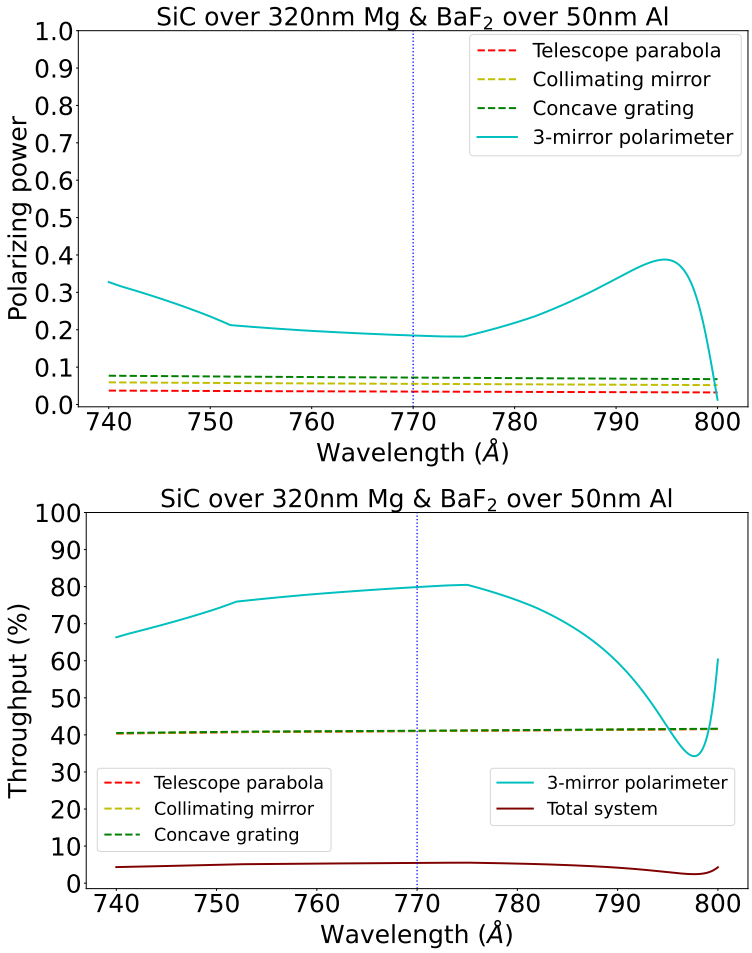

Figure 4.10: Polarizing power (*top panel*), and throughput (*bottom panel*) of the optical components as functions of wavelength. Note that the throughput of telescope, collimator and grating are largely overlapping with each other.

Similarly, we have also varied the thickness of SiC coating over different thicknesses of Mg for the other reflective components. The grating exhibits higher polarization than the telescope and the collimating mirrors, for the SiC layer thickness range of 0.01 to 300 nm, as shown in the bottom panel of Figure 4.9. Therefore, we opted for a

Table 4.2: Throughput of different subsystems

Component	Throughput @ 770 Å (in %)
Telescope parabola	41
Collimator	41.06
Polarimeter	79.88
Grating	41.12

thickness of 300 nm SiC over 320 nm thick Mg for the other components (the grating, the telescope and the collimator) so as to minimize their polarization in the required spectral range of 740 to 800 Å. Since there is no effect of change in thickness of the bottom layer (Al in case of K-mirror polarimeter and Mg in case of other components) on either throughput or polarizing power, hence respective plots are not shown here. Due to the optimization of coating thicknesses on the mirrors of the polarimeter, we are able to achieve higher throughput compared to the plots shown in Figure 4.5.

Assuming a uniform coating thickness on all the components, we have calculated their throughput at the central wavelength of 770 Å as listed in Table 4.2. In order to compute the total throughput of the instrument, we assume an EUV detector with 89% quantum efficiency (Harada *et al.*, 2020). Therefore, the total throughput or efficiency of the system is calculated as approximately 4.92% at 770 Å.

4.4.2 Error budget

After designing an instrument, it is important to identify the various types of errors which will be encountered during the fabrication and assembly of the instrument. In this section, we discuss the different sources of errors, calculated using the tolerancing feature of Zemax, which will affect the system throughput and, consequently, the acquired polarization sensitivity.

In order to achieve a polarimetric precision (in orders better than 10^{-4}) that enables the detection of Hanle polarization signals for diagnosing TR and coronal magnetic fields, we chose a broader slit width of $1''$ (equivalent to 6.32 μm). As a result, the actual spectral resolution of the instrument is defined by the spectral slit width (or, the full-width at half maximum (FWHM) of the line spread function) on the detector which measures approximately 65 μm (calculations are given in Appendix B.1). Therefore, the tolerance analysis is performed with the root-mean-square (RMS) spot radius as the nominal criterion and its maximum limit is set to be the FWHM of the line spread function (LSF).

Through the Inverse Sensitivity analysis, we identify the critical components within the design and establish permissible tolerances for each of their parameter values. The comprehensive error budget for each of the components are documented in Table 4.3. Based on the specified tolerances in Table 4.3, the Monte-Carlo tolerance analysis rigorously evaluates the cumulative effect of these tolerance values on the RMS spot

Table 4.3: Error budget of SPOLEO design components (RMS spot radius of 65 μm)

Parameter	Tolerance Value
Radius of curvature	$\pm 180 \mu m$
Element Tilt	$\pm 10''$
Surface irregularity	$\lambda/10$ @ 770 Å
Element Decenter	$\pm 10 \mu m$
Thicknesses	$\pm 10 \mu m$

radius. It is observed that the radius of curvature causes maximum change in the RMS spot radius from its nominal value. Therefore, the tolerance on the radius of curvature of the components need to be tightened compared to the other parameters.

Table 4.4: Error budget for RMS spot radius of 0.0049 μm (diffraction-limited resolution).

Parameter	Tolerance Value
Telescope parabola:	
Radius of curvature	$\pm$ 56 μm
Element Tilt	$\pm 1.9''$
Surface irregularity	$\lambda/10$ @ 770 Å
Element Decenter	± 10 μm
Thicknesses	± 10 μm
Collimator:	
Radius of curvature	± 47 μm
Element Tilt	$\pm 10''$
Surface irregularity	$\lambda/20$ @ 770 Å
Element Decenter	± 10 μm
Thicknesses	± 10 μm
All other elements:	
Element Tilt	$\pm 10''$
Surface irregularity	$\lambda/10$ @ 770 Å
Element Decenter	± 10 μm
Thicknesses	± 10 μm

Table 4.4 presents the error budget for all the components of the SPOLEO design while considering the case of diffraction-limited resolution. In this case, the maximum limit of perturbing the RMS spot radius is set as the airy disk diameter, i.e. 4.88 μm. We observe that the radius of curvature of telescope and collimating mirrors are stricter than the former case when the RMS spot radius was limited to 65 μm. We also note that in the diffraction-limited case shown in Table 4.4, a higher surface quality ($\lambda/20$) is required for the collimating mirror compared to the other components. However, all the components required a relaxed surface error of $\lambda/10$ in the former case. Furthermore, the tolerance on the tilt angle of the telescope mirror

is about 1.9″, which is very tight compared to the former case when all the elements could be allowed a tilt angle upto 10″ for the RMS spot radius to remain within the limit of 65 μm.

Table 4.5: CTE values for thermal analysis in ZEMAX

Component	Material	CTE
Parabolic Mirrors and Grating	Fused Silica	$0.48 * 10^{-6}$ /K (over -100 to 35°C)
Base Plate	Titanium	$8.6 * 10^{-6}$ /K
	Aluminium	$13 * 10^{-6}$ /K

4.4.3 Thermal analysis

SPOLEO is suitably designed to operate within the EUV wavelengths. These vacuum wavelengths necessitate a space-based instrument that will inevitably encounter substantial temperature variations. Therefore, after determining the error budget for the components used in SPOLEO design, we have simulated the effects of thermal fluctuation on the RMS spot radius by carrying out an extensive analysis for each of the components using ZEMAX.

Due to higher thermal conductivity and very low reflection in the visible and infrared radiation, the telescope parabolic mirror will possess a higher operating temperature than the following components. Therefore, the nominal temperature is assumed to be at 75°C for the telescope parabola and 20°C for the remaining optical components (considered from the SUMER operating temperatures). The change in the RMS spot radius was examined with a temperature variation of ±5°C from the nominal temperature. During the analysis, we observed that the base plate contributes significantly to temperature-induced changes. Therefore, it is crucial to choose a material with lower coefficient of thermal expansion (CTE; cf. Table 4.5) and hence titanium was preferred as the base plate material over aluminium.

For further assessment of the temperature fluctuation on each optical component, we considered six different cases for the analysis. In the first five cases, only one optical component has been subjected to thermal variation, while the others are maintained at their nominal temperature. In the final case, the components altogether are subjected to temperature variation. The change in the RMS spot radius with temperature for each of these cases is shown in Figure 4.11. From the case study, it is noted that the temperature fluctuation of the base plate contributes significantly to the variation in the RMS spot radius, emphasizing the importance of choosing a material exhibiting lower CTE. In order to restrict the RMS spot radius within 65 μm (i.e., the FWHM of the LSF shown as dashed gray line in Figure 4.11), the temperature fluctuation of the base plate must be maintained within ±4°C from the nominal temperature.

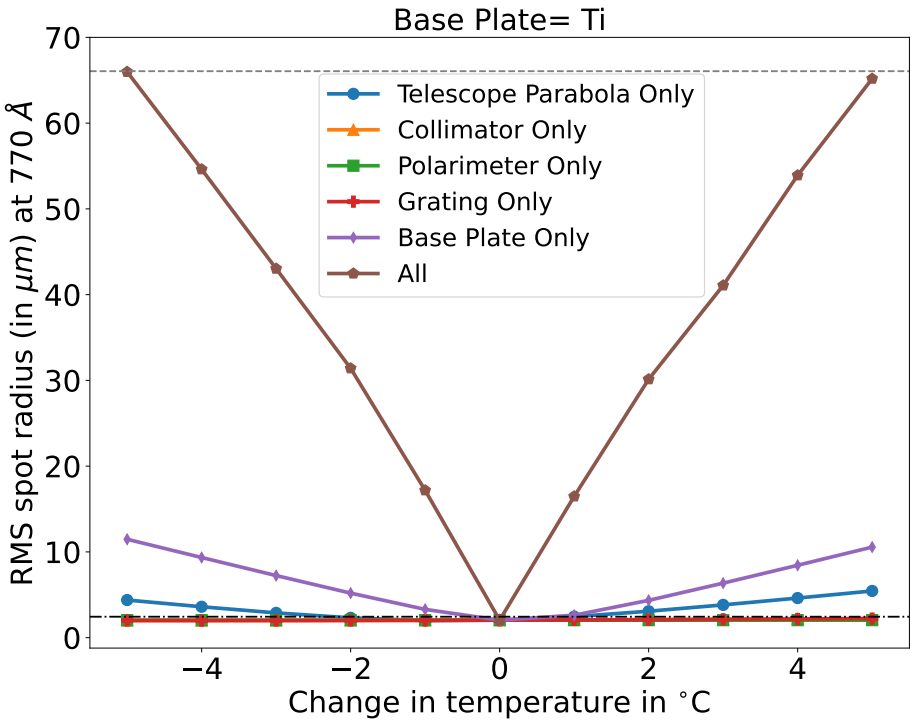

Figure 4.11: Variation of RMS spot radius with temperature. Dashed dotted line corresponds to the airy radius, while dashed gray line corresponds to the FWHM of the LSF.

4.5 Conclusion

While designing a spectropolarimeter, a larger aperture telescope is important to collect more photon flux to achieve higher SNR, thereby achieving the required polarization sensitivity levels. Therefore, we have chosen a telescope aperture of 50 cm in designing SPOLEO which helps in acquiring sensitivity levels of 10^{-5}. The selection of the coating and its thickness plays a pivotal role in optimizing the overall system performance. Assuming a uniform coating on the entire surface of the optical components, we have optimized the coating thicknesses so as to allow for maximum throughput for all the components and maximum polarizing power for the polarimeter. The overall system throughput of SPOLEO is about 5%, which is sufficient to acquire the polarization sensitivity in the orders of 10^{-5}. Furthermore, the dimensions of the slit are crucial in achieving the spatial sampling required for the scientific objective of coronal spectropolarimetric observations of the Sun.

These factors are some of the key considerations in the design of a spectropolarimeter, especially due to photon starvation of the polarimetric observations, a condition that becomes even more challenging when dealing with a fainter corona. To address

this, we performed a comparison of the SNR for photon noise dominated intensity measurements of the EUV corona during the extreme phases of the solar cycle. Our findings (as sorted in Table 7.1) reveal a tenfold increase in SNR from the minima to the maxima phase of the solar cycle. We also estimated the sensitivity level that can be achieved on the degree of linear polarization for different telescope apertures and integration times. It is suggested that pixels binning along the spatial direction of the detector and longer integration times will help in enhancing the polarization sensitivity to the order of 10^{-5} with the designed instrument.

We have also provided an error budget detailing the tolerances which will be required for each component during the fabrication process, thereby guiding the determination of acceptable trade-offs. Since high spectral resolution is not crucial for the Hanle diagnostic technique, the error values have been relaxed within the limits of the scientific requirements. These error values are then compared with those achieved in the diffraction-limited case and we found that more relaxation can be allowed in the former case.

Moreover, we have estimated the surface roughness (or, surface irregularity) which is a key parameter governing the radiation scattering within the instrument. The roughness and the uniformity of the surface coating will also affect the polarizing power of the coating used on the reflection-based polarimeter. Therefore, an in-depth study of the impact of multiple scattering, due to the designed surfaces, on the polarizing power of the instrument can be performed through the stray light analyses of the entire system. The stray light analyses will also ascertain the surface roughness required for each of the optical elements in the SPOLEO design. The conceptual framework of SPOLEO can be further extended to study the polarization aberrations in order to understand their effects on the image-forming potential of the entire system. For this study, the polarization ray tracing feature of Zemax can be utilized to analyze the SPOLEO instrumental polarization.

Chapter 5
Development and laboratory characterization of polarimeter prototype

Design requirements of a Spectropolarimeter for solar Extreme-ultraviolet Observations and characterization of K-mirror based on Brewster's angle
Raveena Khan, Radhika Dharmadhikari, Harsh Mathur, K. Nagaraju, Sinchana R. Jain, D.V.S. Phanindra, K. Sagayanathan, 2024, **Applied Optics**, *under revision.*

5.1 Introduction

To infer the vector magnetic field in the Sun and Sun-type stars, spectropolarimeters are utilized to record measurements of intensity in full polarization mode (i.e., recording Stokes I, Q, U, V). A number of spectropolarimeters are currently operational in different telescopes that differ mainly in the technical realization of polarization modulation. This polarization modulation is either achieved by rotating retarder waveplates (for eg. Socas-Navarro *et al.*, 2006; de Wijn *et al.*, 2022) or by switching retardance using ferroelectric liquid crystals (FLCs) (for eg. Collados *et al.*, 2007; Scharmer *et al.*, 2008). All these techniques involve the utilization of transmission optics for modulation of the polarization states of incoming light.

On the other hand, reflecting surfaces with polarizing coatings (dielectric or metal) split the electric field vector of the incident beam of light into two components: parallel to the plane of incidence, called the s-component, and perpendicular to the plane of incidence, called the p-component. When light of a particular wavelength is incident on a reflecting surface at the Brewster's angle, the reflected beam is optimally linearly polarized, i.e., one polarized component gets suppressed while maximally reflecting the other component. Therefore, the concept of Brewster's angle can be exploited to design a linear polarization modulator.

Such linear polarization modulators find applications in weak-field polarimetry

where the magnetic field of the Sun (Sahal-Brechot, Bommier, and Leroy, 1977; Stenflo, Keller, and Gandorfer, 1998; Khan *et al.*, 2024), the stars (Pallavicini, 1988; Ignace, Nordsieck, and Cassinelli, 2004) and the planets (Ben-Jaffel *et al.*, 2005) can be diagnosed through the Hanle effect (Hanle, 1924). Such polarimeters can also be used for the wavelength domains where transmission optics are non-feasible options. For example, POLLUX onboard the Large Ultraviolet Optical Infrared surveyor (LUVOIR) mission is an innovative reflective polarimeter designed for the far-ultraviolet range (Bouret *et al.*, 2018; Le Gal *et al.*, 2020).

As a continuation of the SPOLEO design discussed in the previous Chapter 4, we have developed a prototype of the K-mirror based polarimeter utilizing the principle of Brewster's angle (Brewster, 1815). Since we do not have a vacuum chamber and clean room facility yet for fabricating the BaF_2 coated mirrors, the prototype has been fabricated with readily available aluminium coated mirrors. In this chapter, we discuss the performance modeling of the polarimeter design and analytical derivation of the modulation matrix, along with the expected Stokes efficiency, using the ZEMAX optical design software. We also demonstrate the development and calibration of the K-mirror based polarimeter in the lab at a visible wavelength of 700 nm. Since the detectors at these wavelengths are sensitive only to intensity, we have established a scheme to encode the polarization information of light in form of intensities. We also discuss the experimental setup which has been used to retrieve the polarization (Stokes I, Q, U) profiles of the incoming light.

5.2 Polarimeter model and Mueller modulation

Figure 5.1 illustrates a three-dimensional (3D) layout of the K-mirror based polarimeter. For the preliminary experiment, we have modeled aluminum (Al) coated mirrors using ZEMAX. Additionally, we have incorporated a thin layer of aluminum oxide coating (Al_2O_3) which forms a thickness of approximately 50 nm over Al coating within few hours of air exposure (Sankarasubramanian, Samson, and Venkatakrishnan, 1999). α represents the angle of incidence at mirrors **M1** and **M3**, and β represents the angle of incidence at mirror **M2**. Different configurations of mirror-based polarimeter have been explored in Chapter 4.2, out of which the 3-mirror configuration (shaped as the letter K) exhibits higher polarizing power (Khan, Nagaraju, and Phanindra, 2023). Moreover, in this design, the angles of incidence at the three mirrors of the polarimeter follow the given relation $2\alpha - \beta = 90^\circ$ (Hass and Hunter, 1978). This condition ensures that the emergent beam from mirror **M3** follows the same path as the incident beam at mirror **M1**. We have considered angle β as the *Brewster's angle* which is calculated as $\theta_B = \tan^{-1}(n)$, where n is the refractive index of the Al_2O_3 coating at 700 nm wavelength.

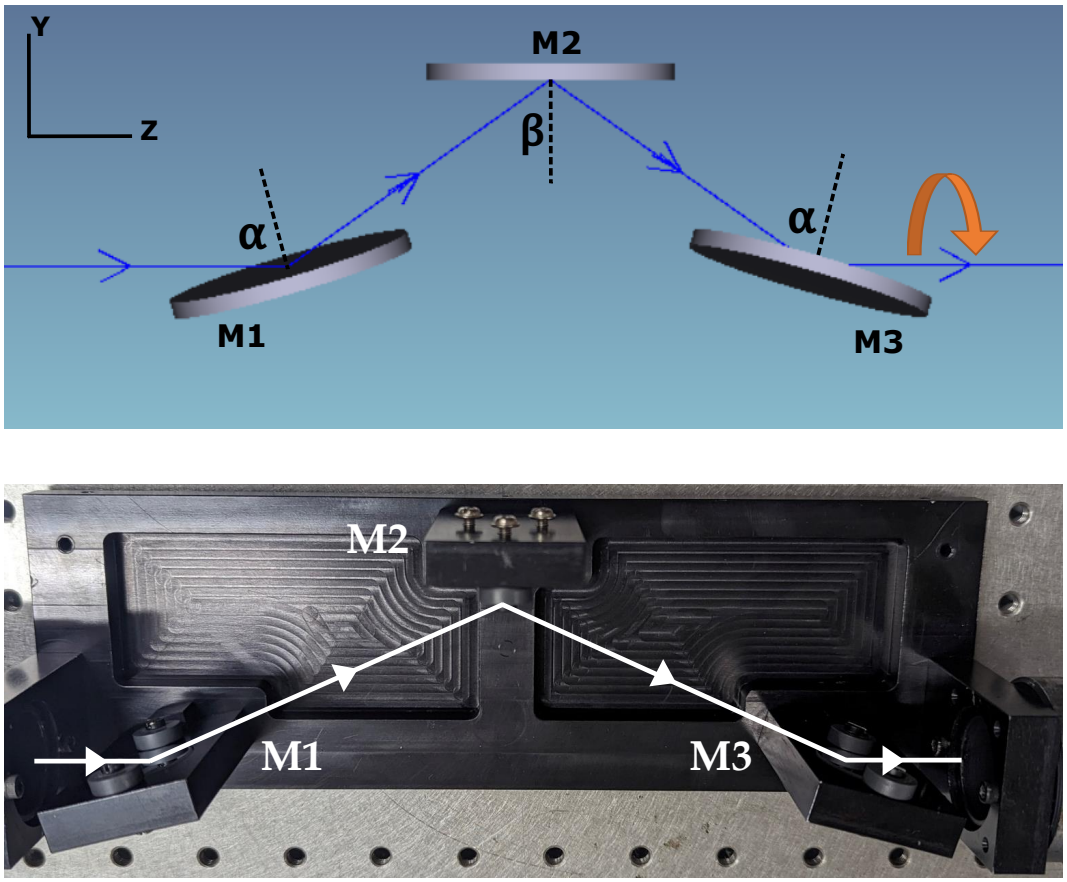

Figure 5.1: *Top panel:* ZEMAX 3D layout of the aluminium coated K-mirror polarimeter. $\boldsymbol{\alpha}$ is the angle of incidence at M1 and M3, while $\boldsymbol{\beta}$ is the angle of incidence at M2 satisfying the relation $2\boldsymbol{\alpha} - \boldsymbol{\beta} = \mathbf{90°}$. Axis Z depicts the optical axis around which the polarimeter is rotated in clockwise direction. *Bottom panel:* Corresponding K-mirror polarimeter housing is fabricated at IIA workshop. The angles $\boldsymbol{\alpha}$ and $\boldsymbol{\beta}$ for the prototype polarimeter at 700 nm are 76° and 61°.

5.2.1 Methodology

The Mueller matrix is a mathematical concept used in polarimetry, which characterizes how the polarization state of the incident light gets affected by interacting with each component in the ensemble of components in the entire system (del Toro Iniesta, 2003). It is usually written as a 4×4 matrix that encompasses the modification of both intensity and the polarization state of light, represented by the Stokes vector (I, Q, U, V). The input Stokes vector $\mathbf{S_{in}}$ can be mathematically related to the output Stokes vector $\mathbf{S_{out}}$ as

$$\mathbf{S_{out}} = \begin{pmatrix} I' \\ Q' \\ U' \\ V' \end{pmatrix} = \mathbf{M_s} \cdot \begin{pmatrix} I \\ Q \\ U \\ V \end{pmatrix} = \mathbf{M_s} \cdot \mathbf{S_{in}} \ , \tag{5.1}$$

where M_s is the Mueller matrix of the system ensemble. In this study, we have considered the system ensemble to be consisting of three mirrors, as shown in Figure 5.1, which altogether form the modulation unit of the polarimeter. The system also acts as a linear polarization analyzer (LPA) due to the second mirror **M2** being set at the Brewster's angle, which polarizes the emergent beam in one direction. The aim of this work is to characterize the LPA through the derivation of its modulation and demodulation matrices so as to retrieve the Stokes parameters (I, Q, U) of the input light.

The Mueller matrix of LPA is calculated using the electric field vector information obtained from ZEMAX (Anche *et al.*, 2015). Starting with deriving the Mueller matrix of each mirror of the LPA, the Jones vectors corresponding to different polarization states are given as inputs to the *Polarization Pupil Map*. In the output for each polarized state, the electric field amplitudes (E_x and E_y) and their phase differences ($\delta = \delta_y - \delta_x$) are obtained from the pupil map. Using these field amplitudes and phase differences, the Stokes parameters are calculated as

$$\begin{pmatrix} I_j \\ Q_j \\ U_j \\ V_j \end{pmatrix} = \begin{pmatrix} E_{xj}^2 + E_{yj}^2 \\ E_{xj}^2 - E_{yj}^2 \\ 2E_{xj}E_{yj}\cos\delta_j \\ 2E_{xj}E_{yj}\sin\delta_j \end{pmatrix} , \tag{5.2}$$

where j corresponds to each of the six states of polarization, i.e., horizontal (0), vertical (90), linear (45 and -45), right circular (RC), and left circular (LC). The Mueller matrix of each mirror surface is then calculated using the six Stokes vectors, as

$$\mathbf{M_{ps}} = \begin{pmatrix} I_0 + I_{90} & I_0 - I_{90} & I_{45} - I_{-45} & I_{RC} - I_{LC} \\ Q_0 + Q_{90} & Q_0 - Q_{90} & Q_{45} - Q_{-45} & Q_{RC} - Q_{LC} \\ U_0 + U_{90} & U_0 - U_{90} & U_{45} - U_{-45} & U_{RC} - U_{LC} \\ V_0 + V_{90} & V_0 - V_{90} & V_{45} - V_{-45} & V_{RC} - V_{LC} \end{pmatrix}. \tag{5.3}$$

For the incident beam of light being parallel, collimated and symmetric about the optical axis, the derived matrices are identical for all the rays. Since the Mueller matrices of each mirror surface are in the local coordinate (ps) frame, they are converted

to the global coordinate system of the incident ray via the rotation matrix,

$$R(\theta) = \begin{pmatrix} 1 & 0 & 0 & 0 \\ 0 & cos(2\theta) & sin(2\theta) & 0 \\ 0 & -sin(2\theta) & cos(2\theta) & 0 \\ 0 & 0 & 0 & 1 \end{pmatrix}. \tag{5.4}$$

The Mueller matrix of each reflecting surface is therefore derived as

$$M(\theta_1) = R(-\theta_1) \cdot M1_{ps} \cdot R(\theta_1), \tag{5.5}$$

$$M(\theta_2) = R(-\theta_2) \cdot M2_{ps} \cdot R(\theta_2), \tag{5.6}$$

$$M(\theta_3) = R(-\theta_3) \cdot M3_{ps} \cdot R(\theta_3), \tag{5.7}$$

respectively, for mirrors **M1**, **M2** and **M3**. Subsequently, the Mueller matrix of the entire polarimeter is calculated as

$$M_{LPA} = M(\theta_3) \cdot M(\theta_2) \cdot M(\theta_1). \tag{5.8}$$

Here, θ_1, θ_2 and θ_3 are the direction cosines of the normal at the surfaces **M1**, **M2** and **M3**. The Mueller matrices of these surfaces in the global coordinate system are $M(\theta_1)$, $M(\theta_2)$ and $M(\theta_3)$.

5.2.2 Simulated results

Using Eqs. 5.2 to 5.8, the Mueller matrix of LPA is derived as

$$\mathbf{M_{LPA}} = \begin{pmatrix} 0.491 & 0.099 & -0.247 & 0.144 \\ -0.196 & -0.285 & 0.317 & 0.075 \\ -0.225 & -0.031 & 0.204 & -0.396 \\ 0.050 & -0.277 & -0.259 & -0.084 \end{pmatrix}. \tag{5.9}$$

The input light is modulated by rotating the K-mirror polarimeter by different angles about its optical axis. The optimal modulation angles are determined using the minimization algorithm of *scipy.optimize.least_squares* function in Python, with the constraint of maximizing the efficiency of Stokes (Q, U). Since the Hanle diagnostic technique focuses solely on the measurement of Stokes (Q, U), we aim to modulate just these Stokes parameters with a balanced (identical) efficiency. After several iterations, we obtained four suitable position angles of LPA: 0°, 5.01°, 23.04° and 45°.

We define the modulation matrix **O** as a $3 \times N$ dimensional matrix formed by positioning the polarimeter at each of the N modulation angles and estimating the

respective Mueller matrix. To derive the modulation matrix from the simulated model, we have selected $N = 4$. Therefore, the first row of the corresponding Mueller matrices together form a 3×4 modulation matrix, which is given as

$$\mathbf{O} = \begin{pmatrix} 1.0000 & 0.203 & -0.503 \\ 1.0000 & 0.288 & -0.460 \\ 1.0000 & 0.503 & -0.203 \\ 1.0000 & 0.503 & 0.203 \end{pmatrix}. \tag{5.10}$$

From the above simulated modulation matrix, the maximum polarimetric efficiency of the Al mirrors based polarimeter is expected to be [1.0, 0.4, 0.37].

5.3 Laboratory experiment

Figure 5.2 shows a side view of the experimental setup at the optics laboratory of the Indian Institute of Astrophysics (IIA). In this section, we delve into the details of the polarimeter characterization procedure conducted within the lab and compare with the simulated results mentioned in the previous Section 5.2.1.

5.3.1 Calibration setup

The calibration setup is placed prior to the LPA. The setup begins with a 12 V, 100 W tungsten-halogen lamp as the light source followed by the collimator. The collimating optics housing has been built in-house at IIA, which is equipped with a 500 μm diameter pinhole at its entrance aperture. The collimated beam passes through a 700 nm bandpass filter before reaching the linear polarization generator (LPG). The LPG is mounted on a rotation stage R1 which is connected to a microstepping driver.

5.3.2 Polarimeter setup

Bottom panel of Figure 5.1 depicts the top view of the polarimeter setup and its rotation housing, which was custom-built at the IIA workshop. This housing accommodates three mirrors, each with a diameter of 25 mm, and incorporates tip-tilt adjustment screws positioned at the rear of the mirror-holding blocks. To confine the beam size within the mirrors' surface area, we have placed a 25 mm variable aperture between the filter and the LPG. The LPA is mounted on a similar rotation stage R2.

5.3.3 Experimental Procedure

Following the LPA, the imaging optics housing is placed before the camera. For acquiring the measured data, we have used an Andor Neo 5.5 sCMOS camera with low read noise (1 electron). A Python code has been developed to control the rotation

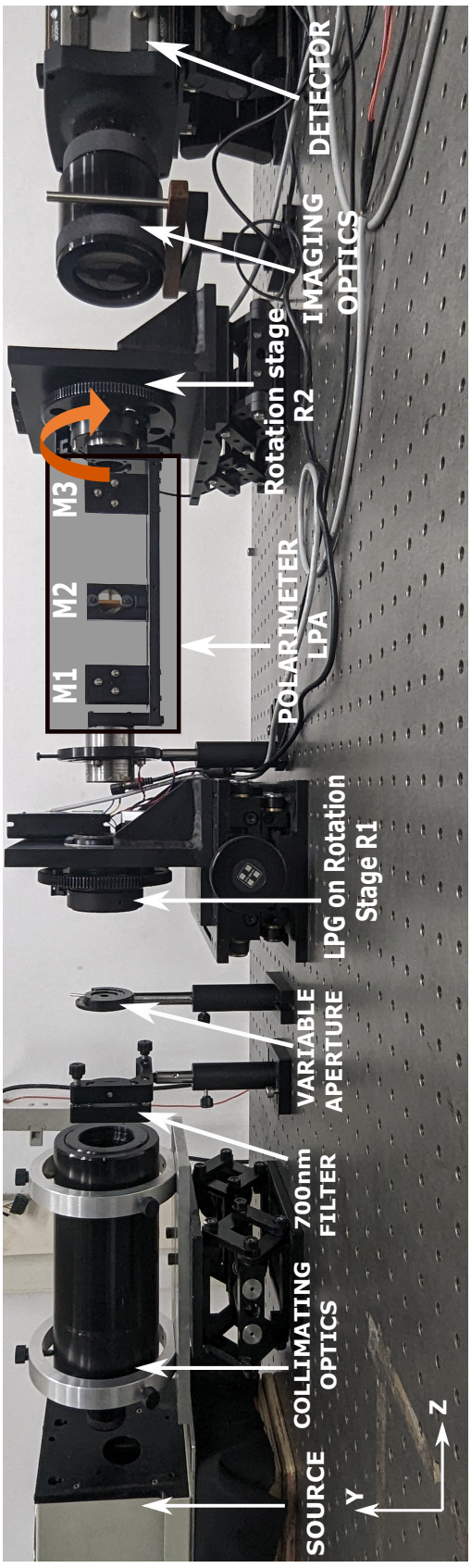

Figure 5.2: Calibration setup for characterizing the K-mirror polarimeter LPA. The optical axis is along Z around which the polarimeter LPA and the LPG are rotated in clockwise direction. (Not to be scaled)

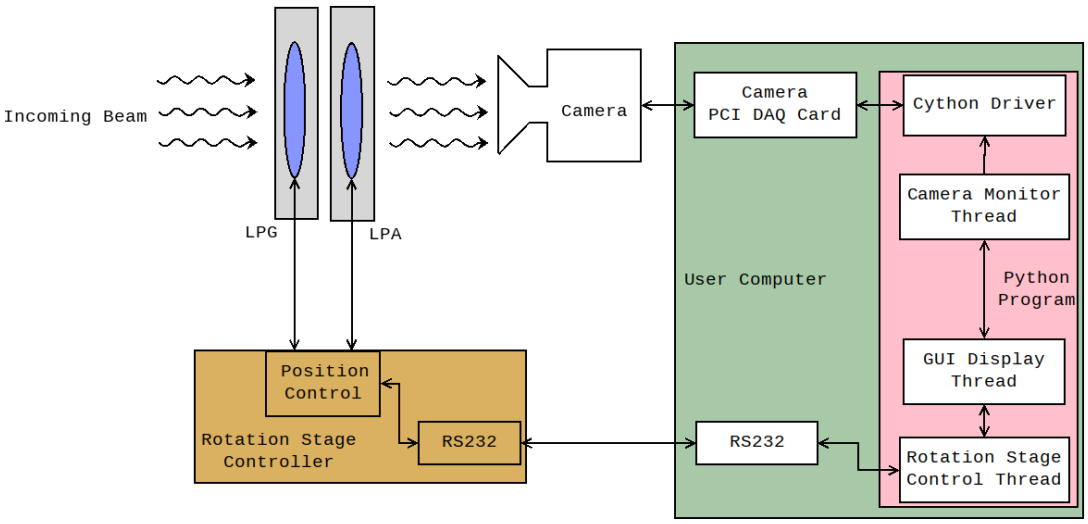

Figure 5.3: Schematic of the rotation stage controller and the camera interface with the computer.

of the LPG and LPA by sending user commands via the RS232 interface. Additionally, the image acquisition is enabled by using a Peripheral Component Interconnect Data Acquisition (PCI-DAQ) card interfaced through the driver provided by Andor. A block diagram illustrating the internal components of the rotation stage controller is shown in Figure 5.3.

Since the detector can only measure the intensities, denoted as I (i.e., first element of $\mathbf{S_{out}}$ in Eq. 5.1), the input polarization must be encoded into intensity variations in such a manner that the polarization states can be derived by analyzing these intensity measurements. As a result, only the first row of the Mueller matrix is relevant for modulation. A generic form of the modulation matrix $\mathbf{O}$ can, therefore, be equated to these output intensities as

$$\mathbf{I_{out}} = \begin{pmatrix} I^1_{out} \\ I^2_{out} \\ . \\ . \\ I^N_{out} \end{pmatrix} = \begin{pmatrix} 1 & m^1_{01} & m^1_{02} & m^1_{03} \\ 1 & m^2_{01} & m^2_{02} & m^2_{03} \\ . & . & . & . \\ . & . & . & . \\ 1 & m^N_{01} & m^N_{02} & m^N_{03} \end{pmatrix} . \begin{pmatrix} I \\ Q \\ U \end{pmatrix} = \mathbf{O} \cdot \mathbf{S_{in}} \, , \tag{5.11}$$

where $\mathbf{I_{out}}$ is the column vector of N intensity measurements performed at each angle of modulation, and $\mathbf{S_{in}}$ is the input Stokes vector we want to obtain from the measurements.

The LPG is rotated from 0 to 360° in steps of 15° at each modulation angle of the LPA. The known states of polarization ($\mathbf{S_{in}}$) are generated, which are then sent through the LPA, and the corresponding intensity outputs are recorded at the detector. This process is repeated for the four position angles of the polarimeter, viz. 0°, 5.01°, 23.04° and 45°, as obtained through the iteration scheme in Section 5.2.2.

Using these intensity measurements ($\mathbf{I_{out}}$), the modulation matrix is calculated as

$$\mathbf{O} = \mathbf{I_{out}} \cdot \mathbf{S_{in}^T} \cdot (\mathbf{S_{in}} \cdot \mathbf{S_{in}^T})^{-1}. \tag{5.12}$$

In order to retrieve the input Stokes parameters $\mathbf{S_{in}}$, the corresponding demodulation matrix ($\mathbf{D}$) is calculated as the pseudo-inverse of the modulation matrix, i.e.,

$$\mathbf{D} = (\mathbf{O^T} \cdot \mathbf{O})^{-1} \cdot \mathbf{O^T}. \tag{5.13}$$

Subsequently, we derive the input Stokes vector as

$$\mathbf{S_{in}} = \mathbf{D} \cdot \mathbf{I_{out}}. \tag{5.14}$$

The efficiency of the polarimeter LPA is calculated from the modulation matrix as

$$\epsilon_i = \left(\frac{1}{N} \sum_{j=1}^{N} O_{ji}^2 \right)^{1/2}, \tag{5.15}$$

where $i \in [I, Q, U]$. While a minimum of $N = 3$ measurements is necessary to retrieve the three Stokes parameters, we have opted for $N = 4$ measurements repeated twice at each of the modulation angles. This choice has improved the SNR associated with each Stokes vector and has therefore enhanced the efficiency of measuring Stokes Q and U.

5.4 Results and Discussion

In the process of deriving the modulation matrix following the experimental procedure mentioned in Section 5.3.3, the LPG is rotated from 0 to 360° in steps of 15° at each modulation angle of the LPA. Hence, we obtain a total of 25×4 data frames, where 25 is the number of known input states of polarization and 4 is the number of modulations. Modulation and demodulation matrices are obtained using Eq. 5.12 and 5.13, respectively. The demodulation matrix is then applied to the measured intensity vector $\mathbf{I_{out}}$ to infer the Stokes parameters of the known input states of polarization. These inferred Stokes inputs are compared with the theoretical values. Figure 5.4 displays the inferred input Stokes parameters after modulating and subsequently demodulating the input. The inferred Stokes inputs (shown as dashed blue line), along with the associated errorbars, are overplotted on the theoretical values (shown as solid orange line).

While determining the modulation and the demodulation matrices, it is crucial to derive the uncertainties arising from the measurement errors, and hence getting propagated to the inferred Stokes profiles. Following the technique described by Asensio Ramos and Collados (2008), we have applied the Monte Carlo method (with

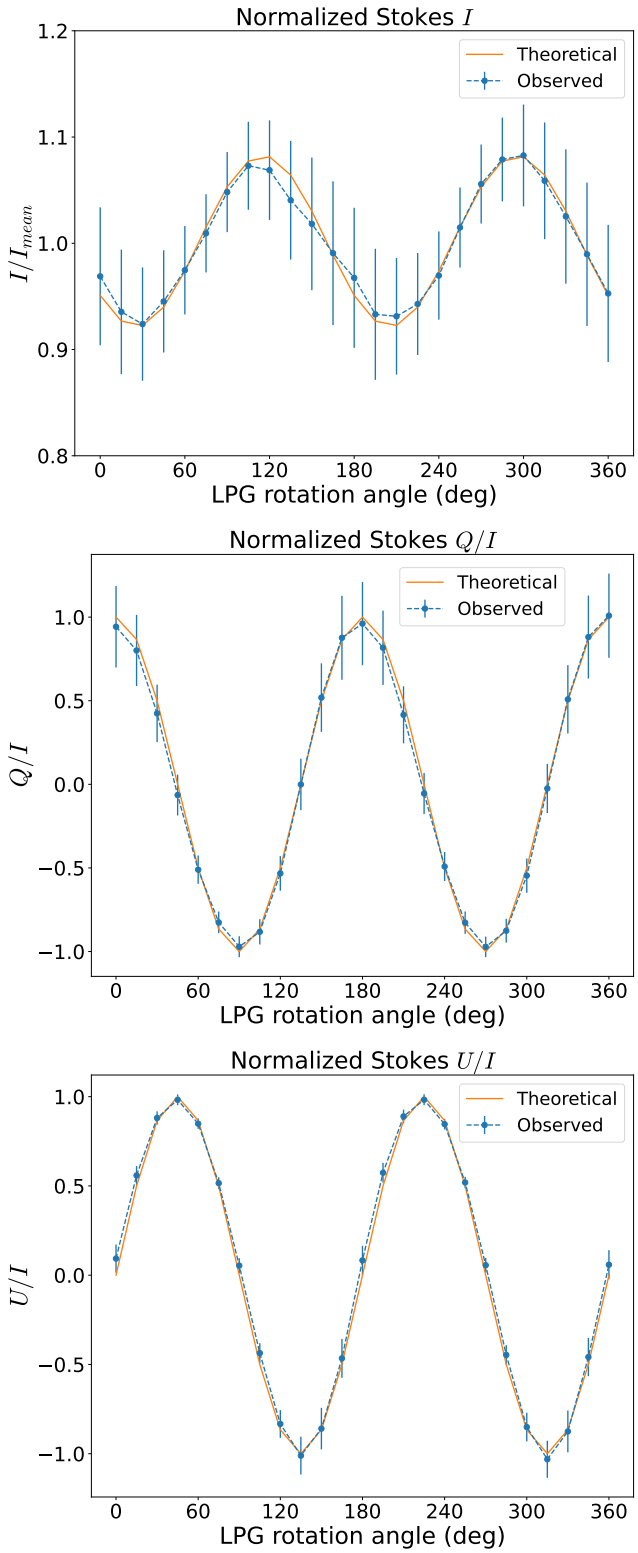

Figure 5.4: Demodulated Stokes profiles which correspond to the input polarization states into the polarimeter LPA. Solid orange line is theoretical, while dashed blue line is measured through the balanced modulation scheme.

$M = 10000$ simulations) to estimate errors in both the modulation and demodulation matrices. In this process, we have utilized the standard deviation of the measured intensities to calculate the errors produced by the measurement setup. Modulation and demodulation matrices are given below along with their associated error estimates.

$$\mathbf{O} = \begin{pmatrix} 1.0 & 0.177 & -0.395 \\ 1.0 & 0.243 & -0.360 \\ 1.0 & 0.404 & -0.156 \\ 1.0 & 0.367 & 0.221 \end{pmatrix} \pm \begin{pmatrix} 0.0 & 0.006 & 0.006 \\ 0.0 & 0.006 & 0.006 \\ 0.0 & 0.007 & 0.008 \\ 0.0 & 0.009 & 0.009 \end{pmatrix}, \tag{5.16}$$

and

$$\mathbf{D} = \begin{pmatrix} 0.716 & -1.944 & 0.071 \\ 0.111 & -0.153 & -0.348 \\ -0.997 & 3.267 & -0.865 \\ 0.720 & -1.314 & 1.184 \end{pmatrix} \pm \begin{pmatrix} 0.063 & 0.178 & 0.059 \\ 0.058 & 0.168 & 0.050 \\ 0.075 & 0.210 & 0.077 \\ 0.078 & 0.224 & 0.072 \end{pmatrix}. \tag{5.17}$$

From the errors on the demodulation matrix (eq. 5.17), the polarimetric accuracy is estimated to be better than 0.224. The maximum difference between the expected and the measured Stokes profiles (shown in Figure 5.4) is about $\sim$ 0.224 for Stokes Q, thereby allowing the measurement of polarization signals upto 0.2 or higher. From the aforementioned modulation matrix, the polarimetric efficiency for Stokes (I, Q, U) is calculated as [1.0, 0.31, 0.30]. Therefore, we have obtained almost balanced efficiencies compared to the simulated results obtained in Section 5.2.2.

5.5 Conclusion

In this chapter, we have presented the development and calibration of a 3-mirror based polarimeter at the visible wavelength of 700 nm. We have studied the characteristics of the polarimeter setup in modulating the linear polarization states of incoming light. The modulating unit consists of three mirrors arranged in a K-shaped configuration to ensure that there is no deviation in the optical axis of the system while rotating the modulator. The second mirror is set at the Brewster's angle, effectively making the polarimeter to act as an analyzer as well.

In this preliminary study, our primary objective was to calibrate a reflection-based linear polarization modulator and explore its potential in the field of polarimetry. Therefore, we developed and tested a prototype polarimeter using readily available aluminium mirrors as reflecting surfaces. Aluminium exhibits low polarizing power; therefore, the instrument efficiency needs to be improved by using highly polarizing coatings on the K-mirror based polarimeter. In our next phase of research, we will focus on developing and characterizing the K-mirror based polarimeter at the Brewster's angle in the EUV spectral range where transmission-based optics is not feasible.

Chapter 6
Summary and Outlook

6.1 Summary

The prime focus of this thesis is to find new diagnostics of the TR and coronal magnetic field vector, exploring suitable instrument concepts and performing a proof-of-concept characterization of the instrument prototype in the laboratory. These new diagnostics in the EUV spectral range will enable both on-disk and off-limb observations of the TR and corona. On-disk magnetic field measurements are important to comprehend the stratification of magnetic field in various layers of the solar atmosphere. A part of the thesis was also associated with a science case of synthesizing the polarization maps at one of the EUV lines and studying the variation of polarization signatures during different phases of the solar cycle. We have also developed an in-house prototype of the polarimeter instrument and performed its characterization in the optics laboratory at a visible wavelength of 700 nm. A chapter wise summary of the main results is presented in the following sections.

6.1.1 Chapter 2

The Hanle diagnostic technique has the potential to probe the weak magnetic field vector of the TR and corona. However, this method requires at least two electric-dipole transition (permitted) lines within the critical Hanle regime to derive an unambiguous solution for the magnetic field vector. To achieve this, we determined crucial parameters, such as the critical Hanle field and the polarizability coefficient, which helped in identifying several permitted lines in the EUV/FUV spectral range of 100 to 1600 Å. The FUV and EUV lines are selected based on their critical magnetic field (those with B_H = 0.01 to 200 G) for Hanle sensitivity, non-zero polarizability coefficient (those with $W_2 > 0$), and reasonable line radiances (those with radiances > 1 photon $\mathrm{cm}^{-2}\mathrm{s}^{-1}\mathrm{arcsec}^{-2}$). The potential Hanle sensitive lines span across the temperature range of $\log_{10}(T) = 5.5 - 6.3$, indicating their emitting regions are in the TR and corona. From an instrumentation perspective, these lines have close proximity in

terms of wavelength separation. Therefore, a single polarimetric instrument based on the concept of Brewster's angle can accommodate at least a pair of these Hanle sensitive lines. A few FUV lines are also examined in the context of providing additional constraints on the LOS component of the magnetic field vector. However, the use of FUV lines is limited by the large wavelength separation (a passband of about 110 Å exists between 1349 Å and 1467 Å) between them. We also found two intriguing lines, Si IX 694 Å and Al X 637 Å, with Hanle sensitivity from 0.001 to 0.05 gauss, which can help in probing very weak TR and coronal magnetic field in the milligauss range. A detailed modeling and interpretation of the polarization of few of these lines will help in determining the polarization signal levels expected for developing a suitable instrument.

6.1.2 Chapter 3

Ne VIII 770 Å is one of the brightest EUV lines emitted between the TR and the lower corona. We have utilized 3D PSIMAS models to simulate the linear polarization and study the variation in the Hanle regime polarization signals during different phases of the solar cycle. The Hanle regime polarization signals at Ne VIII 770 Å vary from 10^{-6} at the disk centre to 10^{1} off-the-limb. We have also examined the effect of collisions on the degree of linear polarization and azimuth signals. Although collisions have a significant impact on the Hanle polarization signals at all solar phases, we have demonstrated how the higher pumping radiation characterizing the solar maximum can help achieve larger SNR values in both Stokes L/I and azimuth. While azimuth values are not affected by the presence of collisional excitation, the noise on their measurement is, because of the contribution of collisional excitation to the total intensity which affects the detectability of polarized signals. Ne VIII 770 Å has shown potential to be used as an overall coronal diagnostic without the need of a coronagraphic instrument. This EUV line is a useful complement to other coronal field diagnostics in the FUV, such as O VI 1032 Å and H I 1216 Å, which share comparable critical Hanle fields of about 35 gauss and 53 gauss, respectively. Further theoretical studies using other EUV spectral lines will help in determining potential candidates that can be used with Ne VIII 770 Å in tandem, for the differential Hanle diagnostic technique.

6.1.3 Chapter 4

Polarimetric observations generally suffer from photon starvation, which becomes even more challenging in case of fainter TR and corona. To address this issue, we have designed an EUV spectropolarimeter using ZEMAX, featuring a larger aperture telescope based on reflective components. We have incorporated suitable mirror coatings and their thicknesses to minimize throughput losses. A 3-mirror based polarimeter has been integrated and optimized which achieves a polarizing power of 20 – 40% in the wavelength range of 740 to 800 Å. Based on the overall performance of the system

in terms of throughput and polarizing power, we have explored various possibilities for achieving the required SNR and therefore the polarization sensitivity levels, along with their limitations. It is suggested that pixel binning along the spatial direction of the detector and longer integration times will help in enhancing the polarization sensitivity of the designed instrument. We have also provided an error budget detailing the tolerances which will be required for guiding through the determination of acceptable trade-offs during the fabrication of each component. The conceptual design of SPOLEO aims to enhance polarimetric diagnostic capabilities to detect the weak polarization signals from the TR and corona. The development of SPOLEO will be a critical step in advancing the EUV spectropolarimetric instrumentation and will aid in bridging the gap in our understanding of the coronal magnetic fields.

6.1.4 Chapter 5

In this chapter, we have used the concept of Brewster's angle to design and develop a 3-mirror based polarimeter at the visible wavelength of 700 nm. We have studied the characteristics of the polarimeter setup in modulating the linear polarization states of incoming light. The modulating unit of the polarimeter consists of three mirrors arranged in a K-shaped configuration to ensure that there is no deviation in the optical axis of the system while rotating the modulator. The second mirror is set at Brewster's angle, effectively allowing the polarimeter to act as an analyzer as well. We have developed and tested a prototype polarimeter using readily available aluminium mirrors as reflecting surfaces. Although these mirrors exhibit low polarizing power, we optimized the polarimeter for maximum possible efficiency. The preliminary results of characterizing this specialized polarimeter will guide us in calibrating the polarimeter with BaF_2 coated mirrors in the required EUV spectral range of 740 to 800 Å, where transmission optics are impractical.

6.1.5 Novelty of thesis

This thesis has the following novel aspects:

- **Novel list of unexplored Hanle sensitive lines in EUV spectra:** A list of Hanle sensitive lines in the EUV spectral range was identified having temperature sensitivity in the TR and coronal regions of the Sun. These lines can be further utilized for developing suitable instruments to measure the magnetic fields at the upper solar atmosphere.
- **First time simulation of on-disk polarization:** We have utilized 3D PSI-MAS datacubes to determine the Hanle polarization signals and study its variation due to several factors, which is a first time approach to perform these simulations directly on the disk of the Sun.

- **A new diagnostic of coronal magnetic field – Ne VIII 770 Å:** We have demonstrated the potential of Ne VIII 770 Å as a new coronal magnetic field diagnostic without the inclusion of a coronagraph instrument. Due to its sensitivity to the critical Hanle effect, Ne VIII 770 Å can be used for probing both the magnetic field strength and the field azimuth in the solar corona.
- **Highly polarizing mirror coatings found in EUV:** We have explored suitable fluoride coatings in the EUV spectral range and found barium fluoride to be possessing high polarizing power and throughput in the EUV spectral range of 740 to 800 Å, where transmission optics is impractical.
- **Design of an EUV solar spectropolarimeter with 50 cm telescope:** We designed an EUV spectropolarimeter with larger aperture telescope for the observations of TR and corona. We have optimized the instrument design to provide higher throughput and allow for the spatial sampling required to enhance the polarization sensitivity levels.
- **First time in-house development of 3-mirror based polarimeter and its rotation housing:** We developed a 3-mirror based polarimeter housing at the IIA workshop and conducted an experiment in the lab to study its characteristics of polarization modulation.

6.2 Future Work

The future scope of this thesis encompasses several intriguing projects. The polarimeter setup developed in the lab is currently a proof-of-concept that was characterized in the visible wavelength of 700 nm. Our future goal is to conduct experiments with mirrors coated with highly polarizing BaF_2 in the required EUV spectral range of 740 to 800 Å, which has been reported to exhibit superior polarizing capability. Additionally, we aim to enhance the polarimeter sensitivity and accuracy by integrating advanced calibration techniques. Furthermore, the stray light analysis of the SPOLEO design will be carried out to determine the requirements on the surface roughness of the optical components used in the instrument.

Another future prospect includes the synthesis of polarization maps using multiple EUV lines and the development of new algorithms to derive the magnetic field information using both the differential Hanle effect and the Zeeman effect. These algorithms will be designed to handle the complex data obtained from the observations and provide more accurate magnetic field measurements. Moreover, there are other symmetry-breaking processes such as non-radial solar wind, ion temperature anisotropy and presence of active regions, which could modify the scattering polarization in addition to the weak magnetic field due to the Hanle effect. In the future, these factors will be carefully accounted for while interpreting the simulated polarization at

the spectral lines considered. A proper comprehension of the contribution of each of these factors to the scattering linear polarization at the transition region and corona will help in isolating them from the ambient magnetic field modification due to the Hanle effect.

Additionally, we plan to collaborate with other research groups to validate our findings and explore new applications of the developed polarimeter in different areas of astrophysics. This collaborative approach will not only enhance the robustness of our results but also open up new avenues for research and innovation.

Bibliography

Altschuler, M.D., Newkirk, G.: 1969, Magnetic Fields and the Structure of the Solar Corona. I: Methods of Calculating Coronal Fields. *Solar Phys.* **9**(1), 131. DOI. ADS.

Anche, R.M., Anupama, G.C., Reddy, K., Sen, A., Sankarasubramanian, K., Ramaprakash, A.N., Sengupta, S., Skidmore, W., Atwood, J., Tirupathi, S., Pandey, S.B.: 2015, Analytical modelling of Thirty Meter Telescope optics polarization. In: Bhattacharya, K. (ed.) *International Conference on Optics and Photonics 2015*, *Society of Photo-Optical Instrumentation Engineers (SPIE) Conference Series* **9654**, 965408. DOI. ADS.

Arnaud, J., Newkirk, J. G.: 1987, Mean properties of the polarization of the Fe XIII 10747 A coronal emission line. *Astron. Astrophys.* **178**(1-2), 263. ADS.

Asensio Ramos, A., Collados, M.: 2008, Error propagation in polarimetric demodulation. *Applied Optics* **47**(14), 2541. DOI. ADS.

Ben-Jaffel, L., Harris, W., Bommier, V., Roesler, F., Ballester, G.E., Jossang, J.: 2005, Predictions on the application of the Hanle effect to map the surface magnetic field of Jupiter. *Icarus* **178**(2), 297. DOI. ADS.

Boe, B., Habbal, S., Druckmüller, M.: 2020, Coronal Magnetic Field Topology from Total Solar Eclipse Observations. *Astrophys. J.* **895**(2), 123. DOI. ADS.

Bogod, V.M., Yasnov, L.V.: 2016, Determination of the Structure of the Coronal Magnetic Field Using Microwave Polarization Measurements. *Solar Phys.* **291**(11), 3317. DOI. ADS.

Bommier, V., Sahal-Brechot, S.: 1982, The Hanle Effect of the Coronal L-Alpha Line of Hydrogen - Theoretical Investigation. *Solar Phys.* **78**(1), 157. DOI. ADS.

Bommier, V., Leroy, J.L., Sahal-Bréchot, S.: 2021, 24 synoptic maps of average magnetic field in 296 prominences measured by the Hanle effect during the ascending phase of solar cycle 21. *Astron. Astrophys.* **647**, A60. DOI. ADS.

Bommier, V., Sahal-Bréchot, S., Leroy, J.L.: 1981, Determination of the complete vector magnetic field in solar prominences, using the Hanle effect. *Astron. Astrophys.* **100**(2), 231. ADS.

Bommier, V., Landi Degl'Innocenti, E., Leroy, J.-L., Sahal-Bréchot, S.: 1994, Complete determination of the magnetic field vector and of the electron density in 14 prominences from

linear polarizaton measurements in the HeI D_3 and Hα lines. *Solar Phys.* **154**(2), 231. DOI. ADS.

Born, M., Wolf, E.: 1999, *Principles of Optics*. ADS.

Bouret, J.-C., Muslimov, E., Neiner, C., Le Gal, M., Lopez Ariste, A., Ferrari, M.: 2018, POLLUX, a high-resolution UV spectropolarimeter for LUVOIR. In: Di Matteo, P., Billebaud, F., Herpin, F., Lagarde, N., Marquette, J.-B., Robin, A., Venot, O. (eds.) *SF2A-2018: Proceedings of the Annual meeting of the French Society of Astronomy and Astrophysics*, Di. ADS.

Brewster, D.: 1815, On the Laws Which Regulate the Polarisation of Light by Reflexion from Transparent Bodies. *Philosophical Transactions of the Royal Society of London Series I* **105**, 125. ADS.

Brosius, J.W., Rabin, D.M., Thomas, R.J.: 2007, Doppler Velocities Measured in Coronal Emission Lines from a Bright Point Observed with the EUNIS Sounding Rocket. *Astrophys. J. Lett.* **656**(1), L41. DOI. ADS.

Brosius, J.W., Rabin, D.M., Thomas, R.J., Landi, E.: 2008, Analysis of a Solar Coronal Bright Point Extreme Ultraviolet Spectrum from the EUNIS Sounding Rocket Instrument. *Astrophys. J.* **677**(1), 781. DOI. ADS.

Carrasco, V.M.S., Vaquero, J.M.: 2021, Solar Cycle 25 is Currently Very Similar to Solar Cycle 24. *Research Notes of the American Astronomical Society* **5**(8), 181. DOI. ADS.

Casini, R., Judge, P.G.: 1999, Spectral Lines for Polarization Measurements of the Coronal Magnetic Field. II. Consistent Treatment of the Stokes Vector forMagnetic-Dipole Transitions. *Astrophys. J.* **522**(1), 524. DOI. ADS.

Collados, M., Lagg, A., Díaz Garcí A, J.J., Hernández Suárez, E., López López, R., Páez Mañá, E., Solanki, S.K.: 2007, Tenerife Infrared Polarimeter II. In: Heinzel, P., Dorotovič, I., Rutten, R.J. (eds.) *The Physics of Chromospheric Plasmas*, *Astronomical Society of the Pacific Conference Series* **368**, 611. ADS.

Condon, E.U., Shortley, G.H.: 1935, *The Theory of Atomic Spectra*. ADS.

Culhane, J.L.: 2007, The Solar-B EUV Imaging Spectrometer: an Overview of the EIS Instrument. In: Shibata, K., Nagata, S., Sakurai, T. (eds.) *New Solar Physics with Solar-B Mission*, *Astronomical Society of the Pacific Conference Series* **369**, 3. ADS.

Curdt, W., Landi, E.: 2001, Spectral windows of the solar atmosphere. In: Battrick, B., Sawaya-Lacoste, H., Marsch, E., Martinez Pillet, V., Fleck, B., Marsden, R. (eds.) *Solar encounter. Proceedings of the First Solar Orbiter Workshop*, *ESA Special Publication* **493**, 199. ADS.

Curdt, W., Landi, E., Feldman, U.: 2004, The SUMER spectral atlas of solar coronal features. *Astron. Astrophys.* **427**, 1045. DOI. ADS.

BIBLIOGRAPHY

Curdt, W., Brekke, P., Feldman, U., Wilhelm, K., Dwivedi, B.N., Schühle, U., Lemaire, P.: 2001, The SUMER spectral atlas of solar-disk features. In: Wimmer-Schweingruber, R.F. (ed.) *Joint SOHO/ACE workshop "Solar and Galactic Composition"*, *American Institute of Physics Conference Series* **598**, 45. DOI. ADS.

de Wijn, A.G., Casini, R., Carlile, A., Lecinski, A.R., Sewell, S., Zmarzly, P., Eigenbrot, A.D., Beck, C., Wöger, F., Knölker, M.: 2022, The Visible Spectro-Polarimeter of the Daniel K. Inouye Solar Telescope. *Solar Phys.* **297**(2), 22. DOI. ADS.

del Toro Iniesta, J.C.: 2003, *Introduction to Spectropolarimetry*. ADS.

del Toro Iniesta, J.C., Collados, M.: 2000, Optimum Modulation and Demodulation Matrices for Solar Polarimetry. *Applied Optics* **39**(10), 1637. DOI. ADS.

Del Zanna, G.: 2012, Benchmarking atomic data for the CHIANTI atomic database: coronal lines observed by Hinode EIS. *Astron. Astrophys.* **537**, A38. DOI. ADS.

Del Zanna, G., Dere, K.P., Young, P.R., Landi, E.: 2021, CHIANTI—An Atomic Database for Emission Lines. XVI. Version 10, Further Extensions. *Astrophys. J.* **909**(1), 38. DOI. ADS.

Dere, K.P., Landi, E., Mason, H.E., Monsignori Fossi, B.C., Young, P.R.: 1997, CHIANTI - an atomic database for emission lines. *Astron. Astrophys. Suppl.* **125**, 149. DOI. ADS.

Didkovsky, L.V., Judge, D.L., Wieman, S.R., McMullin, D.: 2010, Minima of Solar Cycles 22/23 and 23/24 as Seen in SOHO/CELIAS/SEM Absolute Solar EUV Flux. In: Cranmer, S.R., Hoeksema, J.T., Kohl, J.L. (eds.) *SOHO-23: Understanding a Peculiar Solar Minimum*, *Astronomical Society of the Pacific Conference Series* **428**, 73. DOI. ADS.

Drake, G.W.F.: 2006, *Springer Handbook of Atomic, Molecular, and Optical Physics*. DOI. ADS.

Feldman, U., Behring, W.E., Curdt, W., Schühle, U., Wilhelm, K., Lemaire, P., Moran, T.M.: 1997, A Coronal Spectrum in the 500–1610 Angstrom Wavelength Range Recorded at a Height of 21,000 Kilometers above the West Solar Limb by the SUMER Instrument on Solar and Heliospheric Observatory. *Astrophys. J.S* **113**(1), 195. DOI. ADS.

Feldman, U., Brown, C.M., Laming, J.M., Seely, J.F., Doschek, G.A.: 1998, A Compact Spectral Range and Matching Extreme-Ultraviolet Spectrometer for the Simultaneous Study of 1×10^4-2×10^7 K Solar Plasmas. *Astrophys. J.* **502**(2), 997. DOI. ADS.

Fineschi, S., Habbal, S.R.: 1995, Coronal magnetic field diagnostics via the Hanle effect of Lyman series lines. In: *Solar Wind Eight*, 68. ADS.

Fineschi, S., Hoover, R.B., Fontenla, J.M., Walker, J. Arthur B. C.: 1991, Solar EUV/FUV line polarimetry. Pt. 1. Observational parameters and theoretical considerations. In: Hoover, R.B., Walker, J. Arthur B. C. (eds.) *X-Ray/EUV Optics for Astronomy, Microscopy, Polarimetry, and Projection Lithography*, *Society of Photo-Optical Instrumentation Engineers (SPIE) Conference Series* **1343**, 376. DOI. ADS.

Fineschi, S., Hoover, R.B., Zukic, M., Kim, J., Walker, J. Arthur B. C., Baker, P.C.: 1993, Polarimetry of HI Lyman-alpha for coronal magnetic field diagnostics. In: Hoover, R.B., Walker, J. Arthur B. C. (eds.) *Multilayer and Grazing Incidence X-Ray/EUV Optics for Astronomy and Projection Lithography*, *Society of Photo-Optical Instrumentation Engineers (SPIE) Conference Series* **1742**, 423. DOI. ADS.

Fludra, A., Griffin, D., Caldwell, M., Eccleston, P., Cornaby, J., Drummond, D., Grainger, W., Greenway, P., Grundy, T., Howe, C., McQuirk, C., Middleton, K., Poyntz-Wright, O., Richards, A., Rogers, K., Sawyer, C., Shaughnessy, B., Sidher, S., Tosh, I., Beardsley, S., Burton, G., Marshall, A., Waltham, N., Woodward, S., Appourchaux, T., Philippon, A., Auchere, F., Buchlin, E., Gabriel, A., Vial, J.-C., Schühle, U., Curdt, W., Innes, D., Meining, S., Peter, H., Solanki, S., Teriaca, L., Gyo, M., Büchel, V., Haberreiter, M., Pfiffner, D., Schmutz, W., Carlsson, M., Haugan, S.V., Davila, J., Jordan, P., Thompson, W., Hassler, D., Walls, B., Deforest, C., Hanley, J., Johnson, J., Phelan, P., Blecha, L., Cottard, H., Paciotti, G., Autissier, N., Allemand, Y., Relecom, K., Munro, G., Butler, A., Klein, R., Gottwald, A.: 2013, SPICE EUV spectrometer for the Solar Orbiter mission. In: Fineschi, S., Fennelly, J. (eds.) *Solar Physics and Space Weather Instrumentation V*, *Society of Photo-Optical Instrumentation Engineers (SPIE) Conference Series* **8862**, 88620F. DOI. ADS.

Fludra, A., Caldwell, M., Giunta, A., Grundy, T., Guest, S., Leeks, S., Sidher, S., Auchère, F., Carlsson, M., Hassler, D., Peter, H., Aznar Cuadrado, R., Buchlin, É., Caminade, S., DeForest, C., Fredvik, T., Haberreiter, M., Harra, L., Janvier, M., Kucera, T., Müller, D., Parenti, S., Schmutz, W., Schühle, U., Solanki, S.K., Teriaca, L., Thompson, W.T., Tustain, S., Williams, D., Young, P.R., Chitta, L.P.: 2021, First observations from the SPICE EUV spectrometer on Solar Orbiter. *Astron. Astrophys.* **656**, A38. DOI. ADS.

Gary, D.E., Hurford, G.J.: 1994, Coronal Temperature, Density, and Magnetic Field Maps of a Solar Active Region Using the Owens Valley Solar Array. *Astrophys. J.* **420**, 903. DOI. ADS.

Gibson, S., Kucera, T., White, S., Dove, J., Fan, Y., Forland, B., Rachmeler, L., Downs, C., Reeves, K.: 2016, FORWARD: A toolset for multiwavelength coronal magnetometry. *Frontiers in Astronomy and Space Sciences* **3**, 8. DOI. ADS.

Gopalswamy, N., Nitta, N., Akiyama, S., Mäkelä, P., Yashiro, S.: 2012, Coronal Magnetic Field Measurement from EUV Images Made by the Solar Dynamics Observatory. *Astrophys. J.* **744**(1), 72. DOI. ADS.

Grumer, J., Brage, T., Andersson, M., Li, J., Jönsson, P., Li, W., Yang, Y., Hutton, R., Zou, Y.: 2014, Unexpected transitions induced by spin-dependent, hyperfine and external magnetic-field interactions. *Phys. Scr.* **89**(11), 114002. DOI. ADS.

Hale, G.E.: 1908, On the Probable Existence of a Magnetic Field in Sun-Spots. *Terrestrial Magnetism and Atmospheric Electricity* **13**(4), 159. DOI. ADS.

Hanle, W.: 1924, Über magnetische Beeinflussung der Polarisation der Resonanzfluoreszenz. *Zeitschrift fur Physik* **30**(1), 93. DOI. ADS.

Harada, T., Teranishi, N., Watanabe, T., Zhou, Q., Bogaerts, J., Wang, X.: 2020, High-exposure-durability, high-quantum-efficiency (¿90%) backside-illuminated soft-X-ray CMOS sensor. *Applied Physics Express* **13**(1), 016502. DOI. ADS.

Harrington, D.M., Sueoka, S.R., Schad, T.A., Beck, C., Eigenbrot, A.D., de Wijn, A.G., Casini, R., White, A.J., Jaeggli, S.A.: 2023, Systems Approach to Polarization Calibration for the Daniel K. Inouye Solar Telescope (DKIST). *Solar Phys.* **298**(1), 10. DOI. ADS.

Harrison, R.A., Sawyer, E.C., Carter, M.K., Cruise, A.M., Cutler, R.M., Fludra, A., Hayes, R.W., Kent, B.J., Lang, J., Parker, D.J., Payne, J., Pike, C.D., Peskett, S.C., Richards, A.G., Gulhane, J.L., Norman, K., Breeveld, A.A., Breeveld, E.R., Al Janabi, K.F., Mccalden, A.J., Parkinson, J.H., Self, D.G., Thomas, P.D., Poland, A.I., Thomas, R.J., Thompson, W.T., Kjeldseth-Moe, O., Brekke, P., Karud, J., Maltby, P., Aschenbach, B., Bräuninger, H., Kühne, M., Hollandt, J., Siegmund, O.H.W., Huber, M.C.E., Gabriel, A.H., Mason, H.E., Bromage, B.J.I.: 1995, The Coronal Diagnostic Spectrometer for the Solar and Heliospheric Observatory. *Solar Physics* **162**(1-2), 233. DOI. ADS.

Harvey, J.W.: 1969, Magnetic Fields Associated with Solar Active-Region Prominences. PhD thesis, National Solar Observatory. ADS.

Hass, G., Hunter, W.R.: 1978, Reflection polarizers for the vacuum ultraviolet using Al+MgF_2 mirrors and an MgF_2 plate. *Applied Optics* **17**(1), 76. DOI. ADS.

Hebbur Dayananda, S., Trujillo Bueno, J., de Vicente, Á., del Pino Alemán, T.: 2021, Polarization of the Lyα Lines of H I and He II as a Tool for Exploring the Solar Corona. *Astrophys. J.* **920**(2), 140. DOI. ADS.

Hou, J., de Wijn, A.G., Tomczyk, S.: 2013, Design and measurement of the Stokes polarimeter for the COSMO K-coronagraph. *Astrophys. J.* **774**(1), 85. DOI. ADS.

House, L.L.: 1977, Coronal emission-line polarization from the statistical equilibrium of magnetic sublevels. I. Fe XIII. *Astrophys. J.* **214**, 632. DOI. ADS.

House, L.L., Smartt, R.N.: 1982, Vector Magnetic Fields in Prominences - Part One - Preliminary Discussion of Polarimeter Observations in he i D3. *Solar Phys.* **80**(1), 53. DOI. ADS.

Ignace, R., Nordsieck, K.H., Cassinelli, J.P.: 2004, The Hanle Effect as a Diagnostic of Magnetic Fields in Stellar Envelopes. IV. Application to Polarized P Cygni Wind Lines. *Astrophys. J.* **609**(2), 1018. DOI. ADS.

Ingleby, L.D., Spangler, S.R., Whiting, C.A.: 2007, Probing the Large-Scale Plasma Structure of the Solar Corona with Faraday Rotation Measurements. *Astrophys. J.* **668**(1), 520. DOI. ADS.

Ishikawa, R., Bueno, J.T., del Pino Alemán, T., Okamoto, T.J., McKenzie, D.E., Auchère, F., Kano, R., Song, D., Yoshida, M., Rachmeler, L.A., Kobayashi, K., Hara, H., Kubo, M., Narukage, N., Sakao, T., Shimizu, T., Suematsu, Y., Bethge, C., De Pontieu, B., Dalda, A.S., Vigil, G.D., Winebarger, A., Ballester, E.A., Belluzzi, L., Štěpán, J., Ramos, A.A., Carlsson, M., Leenaarts, J.: 2021, Mapping solar magnetic fields from the photosphere to the base of the corona. *Science Advances* **7**(8), eabe8406. DOI. ADS.

Jönsson, P., He, X., Froese Fischer, C., Grant, I.P.: 2007, The grasp2K relativistic atomic structure package. *Computer Physics Communications* **177**(7), 597. DOI. ADS.

Kano, R., Trujillo Bueno, J., Winebarger, A., Auchère, F., Narukage, N., Ishikawa, R., Kobayashi, K., Bando, T., Katsukawa, Y., Kubo, M., Ishikawa, S., Giono, G., Hara, H., Suematsu, Y., Shimizu, T., Sakao, T., Tsuneta, S., Ichimoto, K., Goto, M., Belluzzi, L., Štěpán, J., Asensio Ramos, A., Manso Sainz, R., Champey, P., Cirtain, J., De Pontieu, B., Casini, R., Carlsson, M.: 2017, Discovery of Scattering Polarization in the Hydrogen Lyα Line of the Solar Disk Radiation. *Astrophys. J. Lett.* **839**(1), L10. ADS.

Khan, R., Nagaraju, K.: 2022, Spectral Lines in FUV and EUV for Diagnosing Coronal Magnetic Field. *Solar Physics* **297**(7), 96. DOI. ADS.

Khan, R., Nagaraju, K., Phanindra, D.: 2023, Design concepts of euv polarimeter. In: *Optics for EUV, X-Ray, and Gamma-Ray Astronomy XI* **12679**, 161. SPIE.

Khan, R., Gibson, S.E., Casini, R., Nagaraju, K.: 2024, EUV polarimetric diagnostics of the solar corona: the Hanle effect of Ne VIII 770 Å. *arXiv e-prints*, arXiv:2406.05539. DOI. ADS.

Kohl, J.L., Esser, R., Gardner, L.D., Habbal, S., Daigneau, P.S., Dennis, E.F., Nystrom, G.U., Panasyuk, A., Raymond, J.C., Smith, P.L., Strachan, L., Van Ballegooijen, A.A., Noci, G., Fineschi, S., Romoli, M., Ciaravella, A., Modigliani, A., Huber, M.C.E., Antonucci, E., Benna, C., Giordano, S., Tondello, G., Nicolosi, P., Naletto, G., Pernechele, C., Spadaro, D., Poletto, G., Livi, S., Von Der Lühe, O., Geiss, J., Timothy, J.G., Gloeckler, G., Allegra, A., Basile, G., Brusa, R., Wood, B., Siegmund, O.H.W., Fowler, W., Fisher, R., Jhabvala, M.: 1995, The Ultraviolet Coronagraph Spectrometer for the Solar and Heliospheric Observatory. *Solar Physics* **162**(1-2), 313. DOI. ADS.

Kooi, J.E., Ascione, M.L., Reyes-Rosa, L.V., Rier, S.K., Ashas, M.: 2021, VLA Measurements of Faraday Rotation Through a Coronal Mass Ejection Using Multiple Lines of Sight. *Solar Phys.* **296**(1), 11. DOI. ADS.

Lagg, A., Lites, B., Harvey, J., Gosain, S., Centeno, R.: 2017, Measurements of Photospheric and Chromospheric Magnetic Fields. *Space Sci. Rev.* **210**(1-4), 37. DOI. ADS.

Landi, E., Habbal, S.R., Tomczyk, S.: 2016, Coronal plasma diagnostics from ground-based observations. *Journal of Geophysical Research (Space Physics)* **121**(9), 8237. DOI. ADS.

Landi, E., Hutton, R., Brage, T., Li, W.: 2020, Hinode/EIS Measurements of Active-region Magnetic Fields. *Astrophys. J.* **904**(2), 87. DOI. ADS.

Landi, E., Li, W., Brage, T., Hutton, R.: 2021, Hinode/EIS Coronal Magnetic Field Measurements at the Onset of a C2 Flare. *Astrophys. J.* **913**(1), 1. DOI. ADS.

Landi Degl'Innocenti, E.: 1982, On the effective Landé factor of magnetic lines. *Solar Phys.* **77**(1-2), 285. DOI. ADS.

Landi Degl'Innocenti, E., Landolfi, M.: 2004, *Polarization in Spectral Lines* **307**. DOI. ADS.

Le Gal, M., López Ariste, A., Neiner, C., Pertenais, M.: 2020, Simulation and optimization of a broadband reflective far ultraviolet polarimeter. *Applied Optics* **59**(30), 9320. DOI. ADS.

Leroy, J.L.: 1977, On the intensity of magnetic field in quiescent prominences. *Astron. Astrophys.* **60**(1), 79. ADS.

Li, W., Grumer, J., Yang, Y., Brage, T., Yao, K., Chen, C., Watanabe, T., Jönsson, P., Lundstedt, H., Hutton, R., Zou, Y.: 2015, A Novel Method to Determine Magnetic Fields in Low-density Plasma Facilitated through Accidental Degeneracy of Quantum States in Fe^{9+}. *Astrophys. J.* **807**(1), 69. DOI. ADS.

Li, W., Yang, Y., Tu, B., Xiao, J., Grumer, J., Brage, T., Watanabe, T., Hutton, R., Zou, Y.: 2016, Atomic-level Pseudo-degeneracy of Atomic Levels Giving Transitions Induced by Magnetic Fields, of Importance for Determining the Field Strengths in the Solar Corona. *Astrophys. J.* **826**(2), 219. DOI. ADS.

Li, W., Li, M., Wang, K., Brage, T., Hutton, R., Landi, E.: 2021, A Theoretical Investigation of the Magnetic-field-induced Transition in Fe X, of Importance for Measuring Magnetic Field Strengths in the Solar Corona. *Astrophys. J.* **913**(2), 135. DOI. ADS.

Lin, H., Kuhn, J.R., Coulter, R.: 2004, Coronal Magnetic Field Measurements. *Astrophys. J. Lett.* **613**(2), L177. DOI. ADS.

Lin, H., Penn, M.J., Tomczyk, S.: 2000, A New Precise Measurement of the Coronal Magnetic Field Strength. *Astrophys. J. Lett.* **541**(2), L83. DOI. ADS.

Lionello, R., Linker, J.A., Mikić, Z.: 2001, Including the Transition Region in Models of the Large-Scale Solar Corona. *Astrophys. J.* **546**(1), 542. DOI. ADS.

Liu, J., McIntosh, S.W., De Moortel, I., Wang, Y.: 2015, On the Parallel and Perpendicular Propagating Motions Visible inPolar Plumes: An Incubator For (Fast) Solar Wind Acceleration? *Astrophys. J.* **806**(2), 273. DOI. ADS.

Mackay, D.H., Yeates, A.R.: 2012, The Sun's Global Photospheric and Coronal Magnetic Fields: Observations and Models. *Living Reviews in Solar Physics* **9**(1), 6. DOI. ADS.

Mierla, M., Inhester, B., Antunes, A., Boursier, Y., Byrne, J.P., Colaninno, R., Davila, J., de Koning, C.A., Gallagher, P.T., Gissot, S., Howard, R.A., Howard, T.A., Kramar, M., Lamy, P., Liewer, P.C., Maloney, S., Marqué, C., McAteer, R.T.J., Moran, T., Rodriguez, L., Srivastava, N., St. Cyr, O.C., Stenborg, G., Temmer, M., Thernisien, A., Vourlidas, A., West, M.J., Wood, B.E., Zhukov, A.N.: 2010, On the 3-D reconstruction of Coronal Mass Ejections using coronagraph data. *Annales Geophysicae* **28**(1), 203. DOI. ADS.

Mikić, Z., Linker, J.A., Schnack, D.D., Lionello, R., Tarditi, A.: 1999, Magnetohydrodynamic modeling of the global solar corona. *Physics of Plasmas* **6**(5), 2217. DOI. ADS.

Mitchell, A.C.G., Zemansky, M.W., Keenan, P.C.: 1934, REVIEW: Resonance Radiation and Excited Atoms. *Astrophys. J.* **80**, 77. DOI. ADS.

Mitchell, W.M.: 1904, Reversals in the Spectra of Sun-Spots. *Astrophys. J.* **19**, 357. DOI. ADS.

Moran, T.G.: 2003, Test for Alfvén Wave Signatures in a Solar Coronal Hole. *Astrophys. J.* **598**(1), 657. DOI. ADS.

Nagaraju, K., Prasad, B.R., Hegde, B.S., Narra, S.V., Utkarsha, D., Kumar, A., Singh, J., Kumar, V.: 2021, Spectropolarimeter on board the Aditya-L1: polarization modulation and demodulation. *Applied Optics* **60**(26), 8145. DOI. ADS.

Narra, V.S., Hegde, B., Dasamantarao, U., Venkatasubramanian, N., Somasundaram, P.K., Padhavu, U.K., Budihal, R.P.: 2023, Calibration of Spectropolarimetry Package for Visible Emission Line Coronagraph (VELC) on Board Aditya-L1 Mission. *Journal of Astronomical Instrumentation* **12**(4), 2350011. DOI. ADS.

Nitta, N., White, S.M., Kundu, M.R., Gopalswamy, N., Holman, G.D., Brosius, J.W., Schmelz, J.T., Saba, J.L.R., Strong, K.T.: 1991, Coronal Magnetic Structures Observing Campaign. I. Simultaneous Microwave and Soft X-Ray Observations of Active Regions at the Solar Limb. *Astrophys. J.* **374**, 374. DOI. ADS.

Palik, E.D.: 1985, *Handbook of optical constants of solids*. ADS.

Palik, E.D.: 1991, *Handbook of optical constants of solids II*. ADS.

Pallavicini, R.: 1988, Stellar magnetic fields: measurements and diagnostics. In: Havnes, O., Pettersen, B.R., Schmitt, J.H.M.M., Solheim, J.E. (eds.) *Activity in Cool Star Envelopes* **143**, 25. DOI. ADS.

Patzold, M., Bird, M.K., Volland, H., Levy, G.S., Seidel, B.L., Stelzried, C.T.: 1987, The Mean Coronal Magnetic Field Determined from HELIOS Faraday Rotation Measurements. *Solar Phys.* **109**(1), 91. DOI. ADS.

Pelizzo, M.G., Fineschi, S., Corso, A.J., Zuppella, P., Nicolosi, P., Seely, J., Kjornrattanawanich, B., Windt, D.L.: 2012, Long-term stability of Mg/SiC multilayers. *Optical Engineering* **51**(2), 023801. DOI. ADS.

Peter, H., Abbo, L., Andretta, V., Auchère, F., Bemporad, A., Berrilli, F., Bommier, V., Braukhane, A., Casini, R., Curdt, W., Davila, J., Dittus, H., Fineschi, S., Fludra, A., Gandorfer, A., Griffin, D., Inhester, B., Lagg, A., Landi Degl'Innocenti, E., Maiwald, V., Sainz, R.M., Martínez Pillet, V., Matthews, S., Moses, D., Parenti, S., Pietarila, A., Quantius, D., Raouafi, N.-E., Raymond, J., Rochus, P., Romberg, O., Schlotterer, M., Schühle, U., Solanki, S., Spadaro, D., Teriaca, L., Tomczyk, S., Trujillo Bueno, J., Vial, J.-C.: 2012, Solar magnetism eXplorer (SolmeX). Exploring the magnetic field in the upper atmosphere of our closest star. *Experimental Astronomy* **33**(2-3), 271. DOI. ADS.

Priest, E.R., Hood, A.W. (eds.): 1991, *Advances in solar system magnetohydrodynamics, Cambridge Univ. Press*. ADS.

Querfeld, C.W., Smartt, R.N.: 1984, Comparison of Coronal Emission Line Structure and Polarization. *Solar Phys.* **91**(2), 299. DOI. ADS.

Raouafi, N.-E.: 2002, Stokes parameters of resonance lines scattered by a moving, magnetic medium. Theory of the two-level atom. *Astron. Astrophys.* **386**, 721. DOI. ADS.

Raouafi, N.-E., Lemaire, P., Sahal-Bréchot, S.: 1999, Detection of the O VI 103.2 NM line polarization by the SUMER spectrometer on the SOHO spacecraft. *Astron. Astrophys.* **345**, 999. ADS.

Raouafi, N.-E., Sahal-Bréchot, S., Lemaire, P.: 2002, Linear polarization of the O VI lambda 1031.92 coronal line. II. Constraints on the magnetic field and the solar wind velocity field vectors in the coronal polar holes. *Astron. Astrophys.* **396**, 1019. DOI. ADS.

Raouafi, N.-E., Sahal-Bréchot, S., Lemaire, P., Bommier, V.: 2002, Linear polarization of the O VI lambda 1031.92 coronal line. I. Constraints on the solar wind velocity field vector in the polar holes. *Astron. Astrophys.* **390**, 691. DOI. ADS.

Raouafi, N.E., Riley, P., Gibson, S., Fineschi, S., Solanki, S.K.: 2016, Diagnostics of Coronal Magnetic Fields Through the Hanle Effect in UV and IR Lines. *Frontiers in Astronomy and Space Sciences* **3**, 20. DOI. ADS.

Rast, M.P., Bello González, N., Bellot Rubio, L., Cao, W., Cauzzi, G., Deluca, E., de Pontieu, B., Fletcher, L., Gibson, S.E., Judge, P.G., Katsukawa, Y., Kazachenko, M.D., Khomenko, E., Landi, E., Martínez Pillet, V., Petrie, G.J.D., Qiu, J., Rachmeler, L.A., Rempel, M., Schmidt, W., Scullion, E., Sun, X., Welsch, B.T., Andretta, V., Antolin, P., Ayres, T.R., Balasubramaniam, K.S., Ballai, I., Berger, T.E., Bradshaw, S.J., Campbell, R.J., Carlsson, M., Casini, R., Centeno, R., Cranmer, S.R., Criscuoli, S., Deforest, C., Deng, Y., Erdélyi, R., Fedun, V., Fischer, C.E., González Manrique, S.J., Hahn, M., Harra, L., Henriques, V.M.J., Hurlburt, N.E., Jaeggli, S., Jafarzadeh, S., Jain, R., Jefferies, S.M., Keys, P.H., Kowalski, A.F., Kuckein, C., Kuhn, J.R., Kuridze, D., Liu, J., Liu, W., Longcope, D., Mathioudakis, M., McAteer, R.T.J., McIntosh, S.W., McKenzie, D.E., Miralles, M.P., Morton, R.J., Muglach, K., Nelson, C.J., Panesar, N.K., Parenti, S., Parnell, C.E., Poduval, B., Reardon, K.P., Reep, J.W., Schad, T.A., Schmit, D., Sharma, R., Socas-Navarro, H., Srivastava, A.K., Sterling, A.C., Suematsu, Y., Tarr, L.A., Tiwari, S., Tritschler, A., Verth, G., Vourlidas, A., Wang, H., Wang, Y.-M., NSO and DKIST Project, DKIST Instrument Scientists, DKIST Science Working Group, DKIST Critical Science Plan Community: 2021, Critical Science Plan for the Daniel K. Inouye Solar Telescope (DKIST). *Solar Phys.* **296**(4), 70. DOI. ADS.

Robin, M.B., Kuebler, N.A., Pao, Y.-H.: 1966, Micaceous Biotite as Efficient Brewster Angle Polarizer for Vacuum Ultraviolet. *Review of Scientific Instruments* **37**(7), 922. DOI. ADS.

Sahal-Bréchot, S.: 1977, Calculation of the polarization degree of the infrared lines of Fe XIII of the solar corona. *Astrophys. J.* **213**, 887. DOI. ADS.

Sahal-Brechot, S., Bommier, V., Leroy, J.L.: 1977, The Hanle effect and the determination of magnetic fields in solar prominences. *Astron. Astrophys.* **59**(2), 223. ADS.

Sahal-Bréchot, S., Malinovsky, M., Bommier, V.: 1986, The polarization of the O VI 1032 Å line as a probe for measuring the coronal vector magnetic field via the Hanle effect. *Astron. Astrophys.* **168**, 284. ADS.

Sakurai, T., Spangler, S.R.: 1994, The Study of Coronal Plasma Structures and Fluctuations with Faraday Rotation Measurements. *Astrophys. J.* **434**, 773. DOI. ADS.

Sankarasubramanian, K., Samson, J.P.A., Venkatakrishnan, P.: 1999, Measurement of instrumental polarisation of the Kodaikanal tunnel tower telescope. In: Nagendra, K.N., Stenflo, J.O. (eds.) *Polarization, Astrophysics and Space Science Library* **243**, 313. DOI. ADS.

Saqri, J., Veronig, A.M., Heinemann, S.G., Hofmeister, S.J., Temmer, M., Dissauer, K., Su, Y.: 2020, Differential Emission Measure Plasma Diagnostics of a Long-Lived Coronal Hole. *Solar Phys.* **295**(1), 6. DOI. ADS.

Sarro, L.M., Berihuete, A.: 2011, Statistical techniques for the detection and analysis of solar explosive events. *Astron. Astrophys.* **528**, A62. DOI. ADS.

Sasikumar Raja, K., Venkata, S., Singh, J., Raghavendra Prasad, B.: 2021, Solar Coronal Magnetic Fields and Sensitivity Requirements for Spectropolarimetry Channel of VELC Onboard Aditya-L1. *arXiv e-prints*, arXiv:2110.14179. ADS.

Scharmer, G.B., Narayan, G., Hillberg, T., de la Cruz Rodriguez, J., Löfdahl, M.G., Kiselman, D., Sütterlin, P., van Noort, M., Lagg, A.: 2008, CRISP Spectropolarimetric Imaging of Penumbral Fine Structure. *Astrophys. J. Lett.* **689**(1), L69. DOI. ADS.

Schatten, K.H., Wilcox, J.M., Ness, N.F.: 1969, A model of interplanetary and coronal magnetic fields. *Solar Phys.* **6**(3), 442. DOI. ADS.

Schmelz, J.T., Holman, G.D., Brosius, J.W., Willson, R.F.: 1994, Coronal Magnetic Structures Observing Campaign. III. Coronal Plasma and Magnetic Field Diagnostics Derived from Multiwaveband Active Region Observations. *Astrophys. J.* **434**, 786. DOI. ADS.

Socas-Navarro, H., Elmore, D., Pietarila, A., Darnell, A., Lites, B.W., Tomczyk, S., Hegwer, S.: 2006, Spinor: Visible and Infrared Spectro-Polarimetry at the National Solar Observatory. *Solar Phys.* **235**(1-2), 55. DOI. ADS.

Stenflo, J.: 1994, *Solar Magnetic Fields: Polarized Radiation Diagnostics* **189**. DOI. ADS.

Stenflo, J.O.: 2017, History of Solar Magnetic Fields Since George Ellery Hale. *Space Sci. Rev.* **210**(1-4), 5. DOI. ADS.

Stenflo, J.O., Keller, C.U., Gandorfer, A.: 1998, Differential Hanle effect and the spatial variation of turbulent magnetic fields on the Sun. *Astron. Astrophys.* **329**, 319. ADS.

Susino, R., Bemporad, A., Jejčič, S., Heinzel, P.: 2018, Hot prominence detected in the core of a coronal mass ejection. III. Plasma filling factor from UVCS Lyman-α and Lyman-β observations. *Astron. Astrophys.* **617**, A21. DOI. ADS.

Takenaka, H., Ichimaru, S., Ohchi, T., Gullikson, E.M.: 2005, Soft-X-ray reflectivity and heat resistance of SiC/Mg multilayer. *Journal of Electron Spectroscopy and Related Phenomena* **144**, 1047. DOI. ADS.

Tian, H., Curdt, W., Marsch, E., Schühle, U.: 2009, Hydrogen Lyman-α and Lyman-β spectral radiance profiles in the quiet Sun. *Astron. Astrophys.* **504**(1), 239. DOI. ADS.

Tian, H., DeLuca, E., Cranmer, S., De Pontieu, B., Peter, H., Martínez-Sykora, J., Golub, L., McKillop, S., Reeves, K.K., Miralles, M., *et al.*: 2014, Prevalence of small-scale jets from the networks of the solar transition region and chromosphere. *Science* **346**(6207), 1255711.

Tomczyk, S., McIntosh, S.W., Keil, S.L., Judge, P.G., Schad, T., Seeley, D.H., Edmondson, J.: 2007, Alfvén Waves in the Solar Corona. *Science* **317**(5842), 1192. DOI. ADS.

Tomczyk, S., Card, G.L., Darnell, T., Elmore, D.F., Lull, R., Nelson, P.G., Streander, K.V., Burkepile, J., Casini, R., Judge, P.G.: 2008, An Instrument to Measure Coronal Emission Line Polarization. *Solar Phys.* **247**(2), 411. DOI. ADS.

Tomczyk, S., Landi, E., Burkepile, J.T., Casini, R., DeLuca, E.E., Fan, Y., Gibson, S.E., Lin, H., McIntosh, S.W., Solomon, S.C., Toma, G., Wijn, A.G., Zhang, J.: 2016, Scientific objectives and capabilities of the Coronal Solar Magnetism Observatory. *Journal of Geophysical Research (Space Physics)* **121**(8), 7470. DOI. ADS.

Tomczyk, S., Landi, E., Berkey, B., Burkepile, J., Cotter, M., Galloy, M., Gibson, S., Kolinski, D., Perez-Gonzalez, L., Sewell, S., de Toma, G., Yang, Z., Zmarzly, P.: 2022, Coronal Magnetic Field Measurements with the Upgraded Coronal Multi-channel Polarimeter (UCoMP). In: *The Third Triennial Earth-Sun Summit (TESS* **54**, 2022n7i205p01. ADS.

Trujillo Bueno, J.: 2001, Atomic Polarization and the Hanle Effect. In: Sigwarth, M. (ed.) *Advanced Solar Polarimetry – Theory, Observation, and Instrumentation*, *Astronomical Society of the Pacific Conference Series* **236**, 161. DOI. ADS.

Trujillo Bueno, J.: 2014, Polarized Radiation Observables for Probing the Magnetism of the Outer Solar Atmosphere. In: *Solar Polarization 7*, *Astronomical Society of the Pacific Conference Series* **489**, 137. ADS.

Trujillo Bueno, J., Landi Degl'Innocenti, E., Belluzzi, L.: 2017, The Physics and Diagnostic Potential of Ultraviolet Spectropolarimetry. *Space Sci. Rev.* **210**(1-4), 183. DOI. ADS.

Trujillo Bueno, J., Štěpán, J., Belluzzi, L.: 2012, The Lyα Lines of H I and He II: A Differential Hanle Effect for Exploring the Magnetism of the Solar Transition Region. *Astrophys. J. Lett.* **746**(1), L9. DOI. ADS.

Trujillo Bueno, J., Štěpán, J., Casini, R.: 2011, The Hanle Effect of the Hydrogen Lyα Line for Probing the Magnetism of the Solar Transition Region. *Astrophys. J. Lett.* **738**(1), L11. DOI. ADS.

Trujillo Bueno, J., Landi Degl'Innocenti, E., Collados, M., Merenda, L., Manso Sainz, R.: 2002, Selective absorption processes as the origin of puzzling spectral line polarization from the Sun. *Nature* **415**(6870), 403. DOI. ADS.

Verdebout, S., Nazé, C., Jönsson, P., Rynkun, P., Godefroid, M., Gaigalas, G.: 2014, Hyperfine structures and Landé g_J-factors for n=2 states in beryllium-, boron-, carbon-, and nitrogen-like ions from relativistic configuration interaction calculations. *Atomic Data and Nuclear Data Tables* **100**(5), 1111. DOI. ADS.

Štěpán, J., Trujillo Bueno, J., Carlsson, M., Leenaarts, J.: 2012, The Hanle Effect of Lyα in a Magnetohydrodynamic Model of the Solar Transition Region. *Astrophys. J. Lett.* **758**(2), L43. DOI. ADS.

Wang, T., Innes, D.E., Qiu, J.: 2007, Determination of the Coronal Magnetic Field from Hot-Loop Oscillations Observed by SUMER and SXT. *Astrophys. J.* **656**(1), 598. DOI. ADS.

Warren, H.P., Brooks, D.H.: 2009, The Temperature and Density Structure of the Solar Corona. I. Observations of the Quiet Sun with the EUV Imaging Spectrometer on Hinode. *Astrophys. J.* **700**(1), 762. DOI. ADS.

Warren, H.P., Warshall, A.D.: 2002, Temperature and Density Measurements in a Quiet Coronal Streamer. *Astrophys. J.* **571**(2), 999. DOI. ADS.

West, M.J., Seaton, D.B., D'Huys, E., Mierla, M., Laurenza, M., Meyer, K.A., Berghmans, D., Rachmeler, L.R., Rodriguez, L., Stegen, K.: 2022, A Review of the Extended EUV Corona Observed by the Sun Watcher with Active Pixels and Image Processing (SWAP) Instrument. *Solar Phys.* **297**(10), 136. DOI. ADS.

Wiegelmann, T., Petrie, G.J.D., Riley, P.: 2017, Coronal Magnetic Field Models. *Space Sci. Rev.* **210**(1-4), 249. DOI. ADS.

Wilhelm, K., Curdt, W., Marsch, E., Schühle, U., Lemaire, P., Gabriel, A., Vial, J.-C., Grewing, M., Huber, M.C.E., Jordan, S.D., Poland, A.I., Thomas, R.J., Kühne, M., Timothy, J.G., Hassler, D.M., Siegmund, O.H.W.: 1995, SUMER - Solar Ultraviolet Measurements of Emitted Radiation. *Solar Physics* **162**(1-2), 189. DOI. ADS.

Yang, Z., Bethge, C., Tian, H., Tomczyk, S., Morton, R., Del Zanna, G., McIntosh, S.W., Karak, B.B., Gibson, S., Samanta, T., He, J., Chen, Y., Wang, L.: 2020a, Global maps of the magnetic field in the solar corona. *Science* **369**(6504), 694. DOI. ADS.

Yang, Z., Tian, H., Tomczyk, S., Morton, R., Bai, X., Samanta, T., Chen, Y.: 2020b, Mapping the magnetic field in the solar corona through magnetoseismology. *Science in China E: Technological Sciences* **63**(11), 2357. DOI. ADS.

Young, P.R., Del Zanna, G., Mason, H.E., Dere, K.P., Landi, E., Landini, M., Doschek, G.A., Brown, C.M., Culhane, L., Harra, L.K., Watanabe, T., Hara, H.: 2007, EUV Emission Lines and Diagnostics Observed with Hinode/EIS. *Pub. Astron. Soc. Japan* **59**, S857. DOI. ADS.

Zanna, G.D., Mason, H.E.: 2005, Spectral diagnostic capabilities of Solar-B EIS. *Advances in Space Research* **36**(8), 1503. DOI. ADS.

Zeeman, P.: 1897, The Effect of Magnetisation on the Nature of Light Emitted by a Substance. *Nature* **55**(1424), 347. DOI. ADS.

Zhao, J., Gibson, S.E., Fineschi, S., Susino, R., Casini, R., Li, H., Gan, W.: 2019, Simulating the Solar Corona in the Forbidden and Permitted Lines with Forward Modeling. I. Saturated and Unsaturated Hanle Regimes. *Astrophys. J.* **883**(1), 55. DOI. ADS.

Zhao, J., Gibson, S.E., Fineschi, S., Susino, R., Casini, R., Cranmer, S.R., Ofman, L., Li, H.: 2021, Simulating the Solar Minimum Corona in UV Wavelengths with Forward Modeling II. Doppler Dimming and Microscopic Anisotropy Effect. *Astrophys. J.* **912**(2), 141. DOI. ADS.

Chapter 7
Appendix

A FORWARD synthesis of EUV linear polarization

A.1 Noise estimation for linear-polarization degree and azimuth measurements

We consider a telescope with throughput τ, equipped with a polarimeter that employs a modulation scheme consisting of n independent signal measurements (modulation states), and characterized by Stokes efficiencies ϵ_i, where $i = 0, 1, 2, 3$ for $S_i = I, Q, U, V$. We follow del Toro Iniesta and Collados (2000) for the definition of the Stokes efficiencies of a polarization modulation scheme, in terms of which the polarimetric errors on the Stokes parameters at the entrance of the polarimeter are given by

$$\sigma_i = \frac{1}{\sqrt{n}} \frac{\sigma_s}{\epsilon_i} , \qquad i = 0, 1, 2, 3 , \tag{7.1}$$

where σ_s is the noise associated with the measurement of the signal by the detector at a given modulation state $s = 1, \ldots, n$. It is important to remark that the definition of Stokes efficiencies implied by Eq. (7.1) assumes that the polarimeter has unit transmissivity, so the actual throughput of the polarimeter, including any optical losses and the quantum efficiency of the detector, must be taken into account by the throughput τ of the instrument (see Section 3.3.4). In addition, Eq. (7.1) assumes that σ_s is constant over the modulation cycle, which generally is a good approximation for a temporal modulation scheme (e.g., a rotating retarder), under the condition of weakly polarized signals commonly encountered in observations of the solar corona.

We now consider the total linear polarization signal

$$L = \sqrt{Q^2 + U^2} ,$$

and the corresponding polarimetric error σ_L, given by

$$\sigma_L^2 = \left(\frac{Q}{L}\right)^2 \sigma_Q^2 + \left(\frac{U}{L}\right)^2 \sigma_U^2 \ .$$

For a balanced modulation scheme, $\epsilon_Q = \epsilon_U$,* and thus Eq. (7.1) gives

$$\sigma_L = \sigma_{Q,U} = \frac{1}{\sqrt{n}} \frac{\sigma_s}{\epsilon_{Q,U}} \ . \tag{7.2}$$

It is often preferable to work instead with the linear polarization *degree* $P = L/I$, for which error propagation gives

$$\sigma_P^2 = \left(\frac{L}{I^2}\right)^2 \sigma_I^2 + \frac{\sigma_L^2}{I^2} = P^2 \frac{\sigma_I^2}{I^2} + \frac{\sigma_L^2}{I^2} \ .$$

Using again Eq. (7.1), we can rewrite Eq. (7.2) as

$$\sigma_L = \frac{1}{\sqrt{n}} \frac{\sigma_s}{\epsilon_I} \frac{\epsilon_I}{\epsilon_{Q,U}} = \sigma_I \frac{\epsilon_I}{\epsilon_{Q,U}} \ , \tag{7.3}$$

which we substitute in the expression of σ_P^2 above to get

$$\sigma_P = \frac{\sigma_I}{I} \sqrt{P^2 + \frac{\epsilon_I^2}{\epsilon_{Q,U}^2}} \ . \tag{7.4}$$

Hence, the signal-to-noise ratio $\mathrm{SNR} = I/\sigma_I$ necessary to achieve a sensitivity σ_P on the measurement of P is

$$(\mathrm{SNR})_P = \frac{1}{\sigma_P} \sqrt{P^2 + \frac{\epsilon_I^2}{\epsilon_{Q,U}^2}} \ . \tag{7.5}$$

Similarly, for the linear polarization *azimuth* β, we adopt the definition

$$\beta = \frac{1}{2} \arctan \frac{U}{Q} + \beta_0 \ , \tag{7.6}$$

where β_0 is an appropriate offset necessary to identify the direction of polarization for different sign combinations of Q and U (cf. Landi Degl'Innocenti and Landolfi, 2004, Eqs. (1.8), and the definition of the azimuth we have given in Section 3.3). We thus

*In the ideal case of a balanced and optimally efficient linear-polarization scheme, $\epsilon_I = 1$ and $\epsilon_{Q,U} = 1/\sqrt{2}$.

have

$$\begin{aligned}\sigma_\beta^2 &= \frac{1}{4}\left(\frac{U}{L^2}\right)^2\sigma_Q^2 + \frac{1}{4}\left(\frac{Q}{L^2}\right)^2\sigma_U^2 \\ &= \frac{1}{4}\,\frac{Q^2+U^2}{L^4}\,\sigma_L^2 = \frac{1}{4L^2}\,\sigma_L^2 \\ &= \frac{1}{4P^2}\,\frac{\sigma_L^2}{I^2}\,,\end{aligned}$$

and using again Eq. (7.3),

$$\sigma_\beta = \frac{1}{2}\,\frac{\epsilon_I}{\epsilon_{Q,U}}\,\frac{1}{P}\,\frac{\sigma_I}{I}\,. \tag{7.7}$$

Hence, the signal-to-noise ratio (SNR) necessary to achieve a sensitivity σ_β on the measurement of β is

$$(\mathrm{SNR})_\beta = \frac{1}{2}\,\frac{\epsilon_I}{\epsilon_{Q,U}}\,\frac{1}{P}\,\frac{1}{\sigma_\beta}\,. \tag{7.8}$$

A.1.1 Presence of a background signal

The previous analysis assumed that the observed intensity signal I is produced exclusively by physical processes responsible for the line emission, possibly including collisional excitation and de-excitation. In the presence of ambient and instrumental stray light, or a physical continuum that does not pertain to the resonance scattering process (e.g., a Planckian continuum from the disk, or Thomson scattered radiation off the limb), the target signal I is only a contribution to the total observed signal, i.e.,

$$I_{\mathrm{obs}} = I + I_{\mathrm{bg}}\,, \tag{7.9}$$

where we indicate with I_{bg} the sum of all contributions to the observed intensity signal other than resonance line scattering. We call these contributions "background" because it is possible in theory (e.g., through the spectral analysis of the incoming radiation) to separate those contributions from the observed signal in order to isolate the target line signal. Thus, the intensity signal I needed to compute the observables of the previous analysis and their noise (we note that β is independent of I, but σ_β is not) must be obtained via background subtraction, i.e.,

$$I = I_{\mathrm{obs}} - I_{\mathrm{bg}}\,. \tag{7.10}$$

If the intensity signals I_{obs} and I_{bg} are expressed in photon counts, then the variance on I (assuming the independent measurement of the background) is given by

$$\begin{aligned}\sigma_I^2 &= \sigma_{\mathrm{obs}}^2 + \sigma_{\mathrm{bg}}^2 \\ &\approx I_{\mathrm{obs}} + I_{\mathrm{bg}} = I + 2I_{\mathrm{bg}}\,,\end{aligned} \tag{7.11}$$

where for the approximation in the second line we assume that all intensity measurements are photon-noise limited, so the photon count N satisfies the Poisson-statistics condition $\sigma_N \approx \sqrt{N}$, and in the last equivalence we use again Eq. (7.9). Eq. (7.11) can finally be rewritten as

$$\sigma_I^2 = \sigma_{\rm obs}^2 \left(1 + \frac{\sigma_{\rm bg}^2}{\sigma_{\rm obs}^2}\right) \approx \sigma_{\rm obs}^2 \left(1 + \frac{I_{\rm bg}}{I_{\rm obs}}\right) \ . \tag{7.12}$$

It is important to remark that the two *measured* signals in Eq. (7.9) are $I_{\rm obs}$ and $I_{\rm bg}$, and for these it is typically desirable (or required) to achieve photon-noise limited acquisition, so that the Poisson-statistics relation for the signal's noise implied by Eq. (7.11) is valid. On the other hand, the noise on the *derived* signal I does not satisfy the same relation, as shown by Eq. (7.11), even if the coronal photons that contribute to the I signal obviously still obey the Poisson statistics.

The expression (7.12) for σ_I must be used in Eqs. (7.4) and (7.7) in order to calculate the proper target SNR in the presence of a background, for a given noise target on P and β, respectively. After some tedious but straightforward algebra, we find

$$\begin{aligned} \frac{\sigma_I}{I} &= \left(\frac{\sigma_{\rm obs}}{I_{\rm obs}}\right) \frac{I_{\rm obs}}{I} \sqrt{1 + \frac{I_{\rm bg}}{I_{\rm obs}}} \\ &\equiv ({\rm SNR})^{-1} \sqrt{\frac{I_{\rm obs}^2}{I^2}\left(1 + \frac{I_{\rm bg}}{I_{\rm obs}}\right)} \\ &= ({\rm SNR})^{-1} \sqrt{\left(1 + \frac{I_{\rm bg}}{I}\right)\left(1 + \frac{2I_{\rm bg}}{I}\right)} \ , \end{aligned} \tag{7.13}$$

showing that, in the presence of a background, the required SNR of Eqs. (7.5) and (7.8) are augmented by the factor

$$k_{\rm bg} = \sqrt{\left(1 + \frac{I_{\rm bg}}{I}\right)\left(1 + \frac{2I_{\rm bg}}{I}\right)} \ . \tag{7.14}$$

We note that this correction factor is dimensionless and does not depend on the specific intensity units adopted. In particular, it can also be calculated using energy units instead of photon counts.

In conclusion, *in the presence of a background signal*, the required SNR for a given sensitivity target on the quantitites P and β becomes, respectively,

$$({\rm SNR})_P = \frac{k_{\rm bg}}{\sigma_P} \sqrt{P^2 + \frac{\epsilon_I^2}{\epsilon_{Q,U}^2}} \ , \tag{7.15}$$

$$(\mathrm{SNR})_\beta = \frac{1}{2}\,\frac{\epsilon_I}{\epsilon_{Q,U}}\,\frac{1}{P}\,\frac{k_{\mathrm{bg}}}{\sigma_\beta}\,. \tag{7.16}$$

A.2 Supplementary figures

Figures 7.1, 7.2, and 7.3 correspond to the remaining eight CR simulations indicated in Section 3.2, with captions identical to those in Figures 3.1, 3.3, and 3.4, respectively.

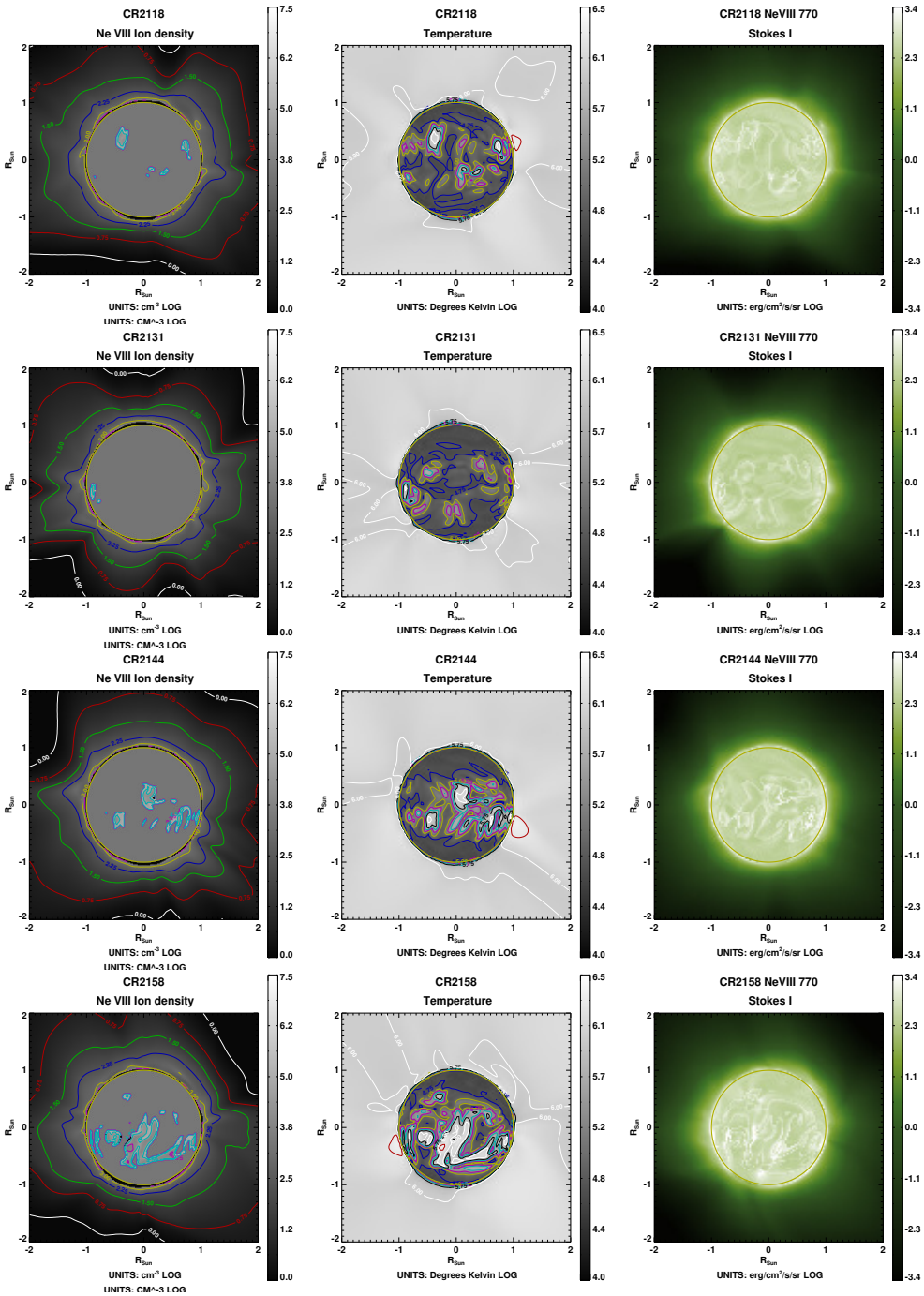

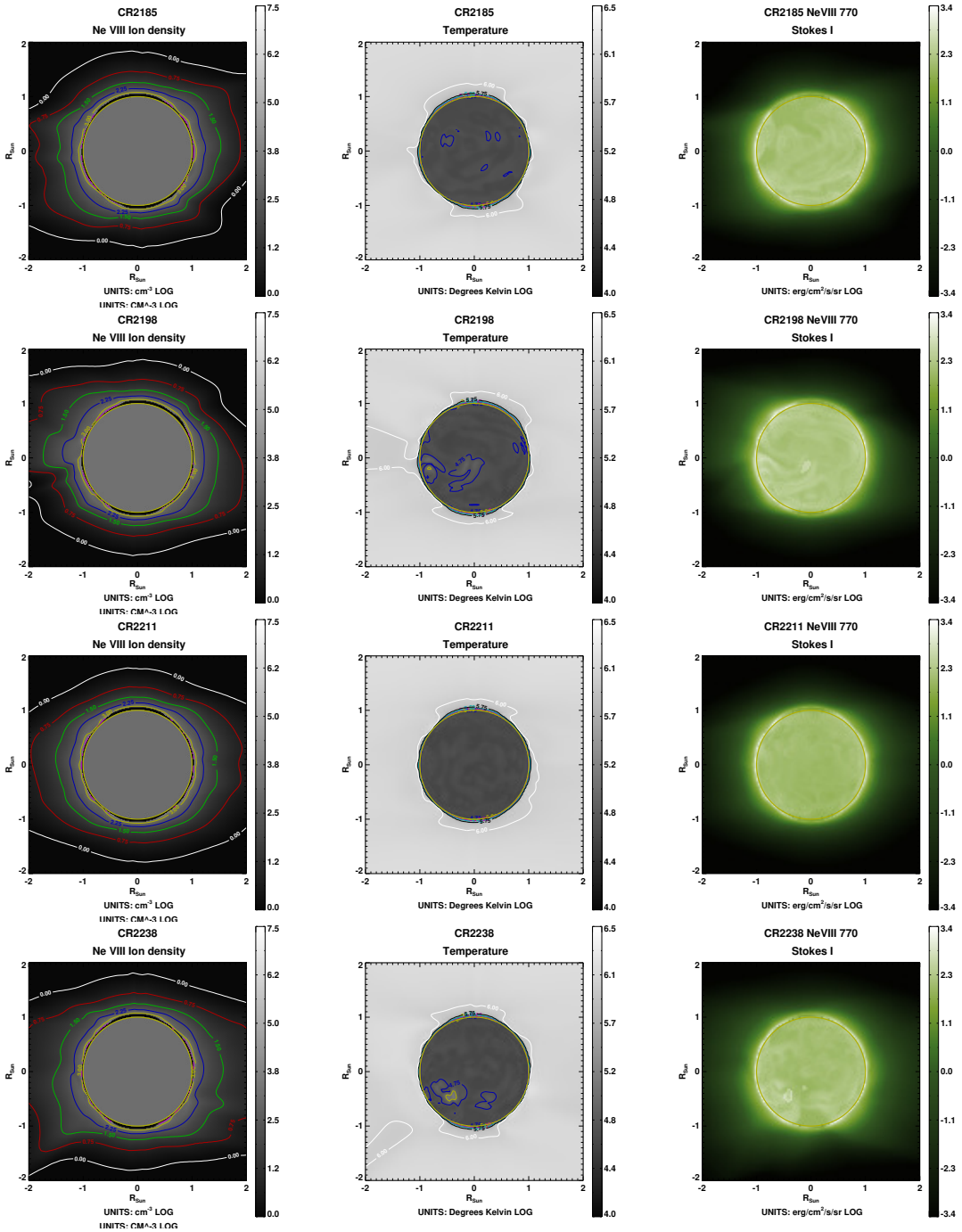

Figure 7.1: Same as Figure 3.1, but for the remaining CR simulations.

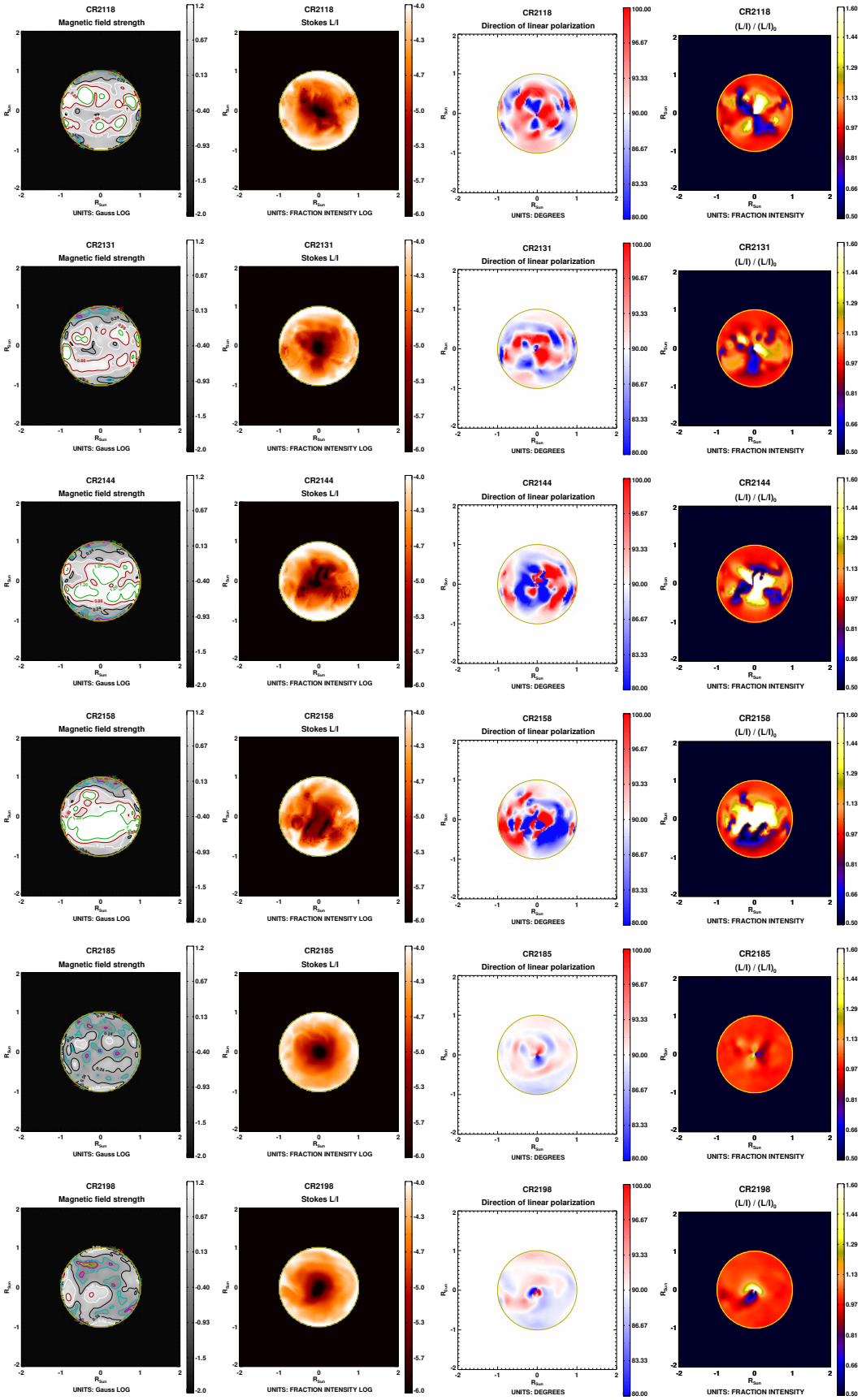
CR2118
Magnetic field strength
UNITS: Gauss LOG
CR2118
Stokes L/I
UNITS: FRACTION INTENSITY LOG
CR2118
Direction of linear polarization
UNITS: DEGREES
CR2118
(L/I) / (L/I)0
UNITS: FRACTION INTENSITY
CR2131
Magnetic field strength
UNITS: Gauss LOG
CR2131
Stokes L/I
UNITS: FRACTION INTENSITY LOG
CR2131
Direction of linear polarization
UNITS: DEGREES
CR2131
(L/I) / (L/I)0
UNITS: FRACTION INTENSITY
CR2144
Magnetic field strength
UNITS: Gauss LOG
CR2144
Stokes L/I
UNITS: FRACTION INTENSITY LOG
CR2144
Direction of linear polarization
UNITS: DEGREES
CR2144
(L/I) / (L/I)0
UNITS: FRACTION INTENSITY
CR2158
Magnetic field strength
UNITS: Gauss LOG
CR2158
Stokes L/I
UNITS: FRACTION INTENSITY LOG
CR2158
Direction of linear polarization
UNITS: DEGREES
CR2158
(L/I) / (L/I)0
UNITS: FRACTION INTENSITY
CR2185
Magnetic field strength
UNITS: Gauss LOG
CR2185
Stokes L/I
UNITS: FRACTION INTENSITY LOG
CR2185
Direction of linear polarization
UNITS: DEGREES
CR2185
(L/I) / (L/I)0
UNITS: FRACTION INTENSITY
CR2198
Magnetic field strength
UNITS: Gauss LOG
CR2198
Stokes L/I
UNITS: FRACTION INTENSITY LOG
CR2198
Direction of linear polarization
UNITS: DEGREES
CR2198
(L/I) / (L/I)0
UNITS: FRACTION INTENSITY

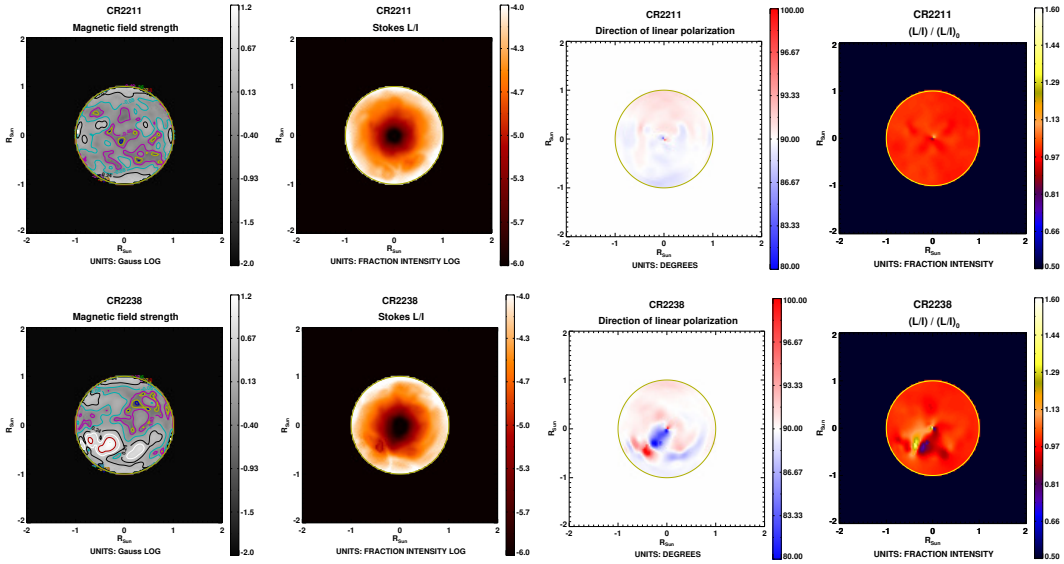

Figure 7.2: Same as Figure 3.3 but for the remaining CR simulations.

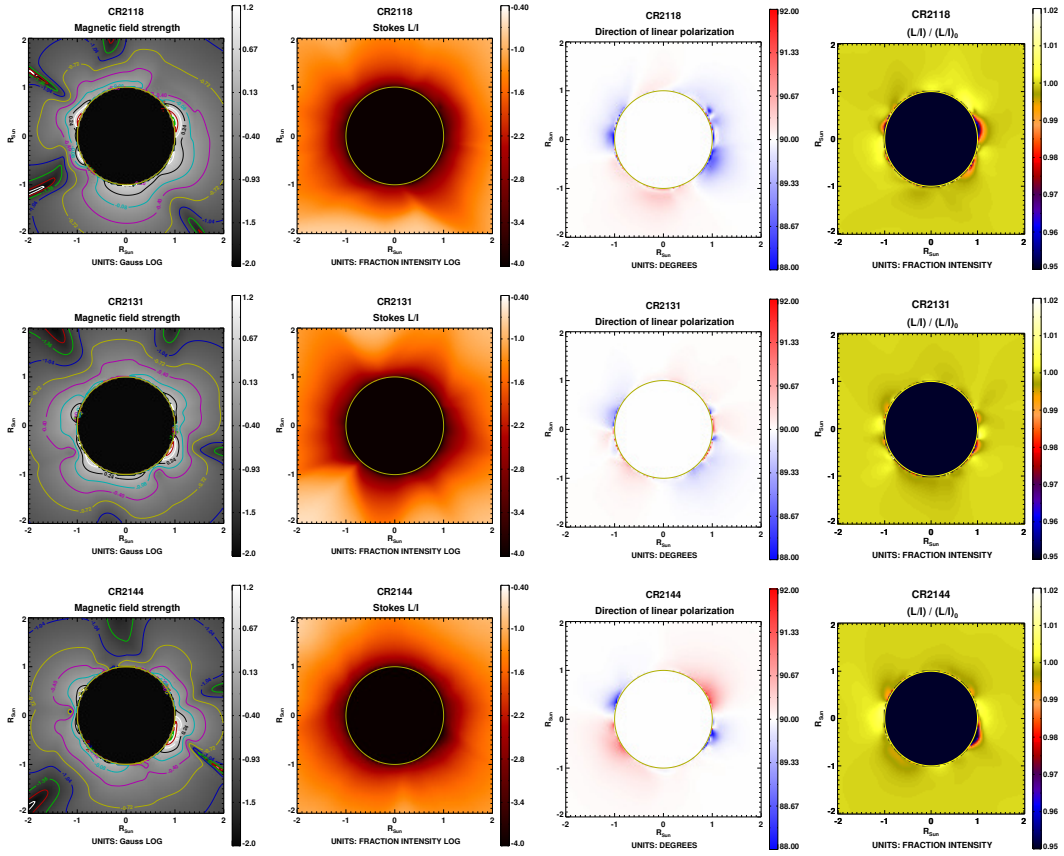

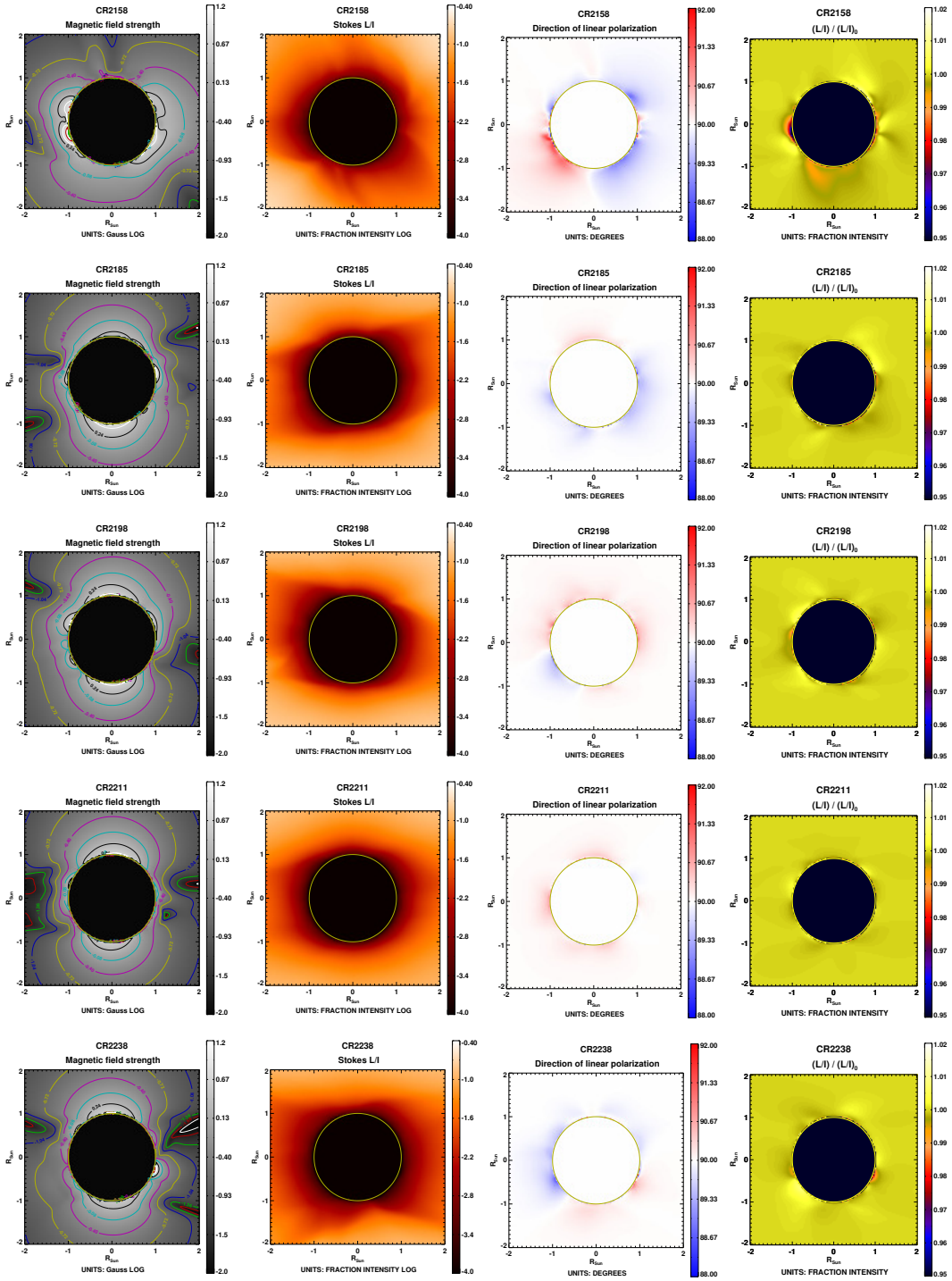

Figure 7.3: Same as Figure 3.4 but for the remaining CR simulations.

B Design of an EUV spectropolarimeter

B.1 Calculation of optical parameters

In the design of SPOLEO, we consider a telescope aperture of diameter (d_{tel}) 50 cm which constitutes a parabolic mirror having a focal length (f_{tel}) of 1302.77 mm and an off-axis distance (called decenter in Y) of 330 mm. So, its off-axis angle can be calculated as

$$\theta_{tel} = \frac{decenter}{f_{tel}} = 14.21^{\circ} \ . \tag{7.17}$$

A slit is placed at the focal plane of the telescope where the plate scale can be derived as

$$s = \frac{206265}{f_{tel}} = 158.33 \ arcsec/mm \ . \tag{7.18}$$

Similarly, the off-axis angle of the collimating parabolic mirror, with Y-direction decenter of 63 mm and focal length (f_{coll}) of 172.25 mm, can be calculated as 20.09°.

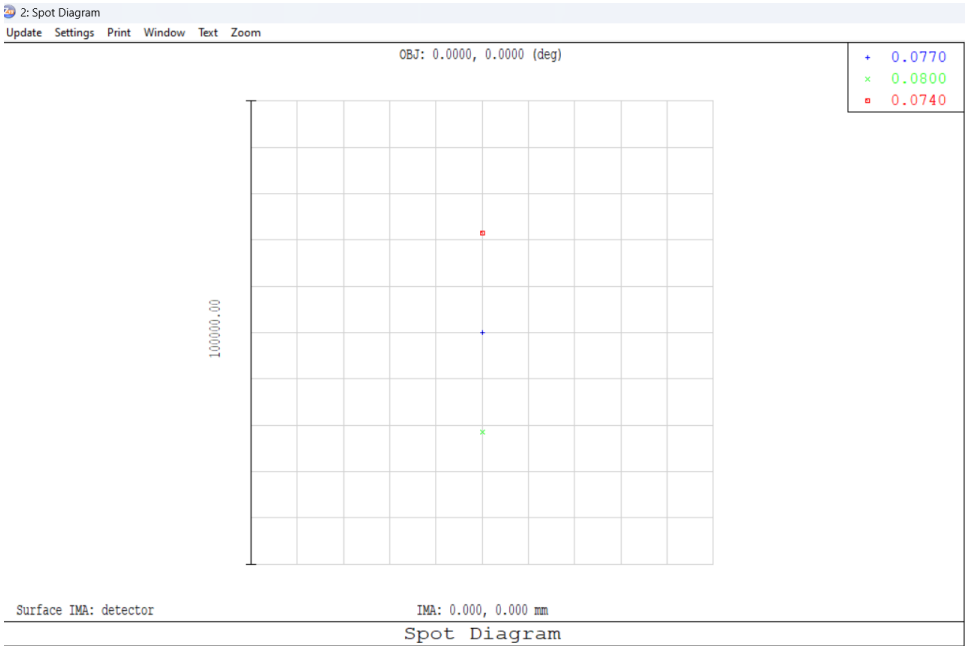

Figure 7.4: Figure illustrating linear dispersion between the wavelengths of 740 Å and 800 Å.

We have chosen a concave grating of radius (R_{cam}) 3509.52 mm and a groove density (g_d) of 4000 lines/mm. The grating also acts as an imaging camera. Given the angle of incidence (i) of 18.52° at a wavelength (λ_c) of 770 Å, the focal length of grating can be computed as

$$f_{cam} = \frac{R_{cam}}{1 + \cos i} = 1803.28 \ mm \ . \tag{7.19}$$

Therefore, the magnification factor at the detector plane due to the entire optical system is given by

$$M = \frac{f_{cam}}{f_{coll}} = 10.47 \ . \tag{7.20}$$

The angle of diffraction for the grating in first diffraction order ($m = 1$) can be derived using the grating equation as

$$d = \sin^{-1}\left(\frac{m \times \lambda_c}{1/g_d} - \sin i\right) = -0.55^{\circ} \ . \tag{7.21}$$

At the image/detector plane which corresponds to the last surface in the Lens data editor of ZEMAX, the linear dispersion due to the grating is calculated by measuring the separation between two adjacent spectral wavelengths at the Spot diagram, as shown in Figure 7.4. To compute the linear dispersion, we must choose multiple wavelengths in the Settings tab of the Spot diagram. For example, if we observe the physical separation between the wavelengths 740 Å and 800 Å, it is around 43080 μm. So, the linear dispersion can be calculated as

$$\beta = \frac{43080}{(800 - 740)} = 718 \ \mu m/\text{Å} \ . \tag{7.22}$$

The slit dimensions are computed so as to allow the required spatial sampling of 32″/pixel, which is a pre-requisite for the spectropolarimetric observations of the solar corona as reported in our recent study (Khan *et al.*, 2024). Therefore, we began with a slit width (s_w), equal to 6.32 μm corresponding to around 1″, at which the fraction of enclosed energy (in ZEMAX) reaches maximum. The spectral slit width in the dispersion direction, which is also referred to as the FWHM of the LSF, is derived as

$$s_{sw} = \frac{s_w \times M \times \cos i}{\beta \times \cos d} = 0.09 \ \text{Å} \ , \tag{7.23}$$

which covers a physical separation of around 65 μm (calculated using the linear dispersion of 718 μm/Å) on the detector plane. Next, we can calculate the plate scale at the detector plane by choosing different field angles in the Settings tab of the Spot diagram. For example, we have inserted field angles of (0°,0°) and (0°,1°) in the Field tab of ZEMAX, which covers a physical separation of 223.2 mm on the detector plane. Then the plate scale at the detector plane can be derived as

$$s_d = \frac{1 \times 3600}{223.2} = 16.12 \ arcsec/mm \ . \tag{7.24}$$

Now we consider a 1024 × 1280 detector with each pixel pitch (p) of 15 μm. Hence, the image scale at the detector plane is around 0.24″/pixel. This implies in order to obtain the required spatial sampling of 32″/pixel, we need to apply the pixels-binning technique along the spatial extent of the detector. Moreover, a longer slit

corresponding to 32″/pixel need to be selected which will also facilitate the acquisition of the desired levels of polarization sensitivity. Hence, the spatial length of the slit on the detector can be derived as

$$s_l = \frac{32 \times p}{0.24} = 2\ mm\ . \tag{7.25}$$

B.2 Calculation of Ne VIII photon flux

In the no-binning case, considering a slit width of 1″ and length of 0.24″, we have calculated the expected photon fluxes at Ne VIII 770 Å during the two extreme phases of solar cycle 23 (presented in Table 7.1).

Table 7.1: Ne VIII 770 Å photon flux during solar maxima and minima phase

	Solar max	**Solar min**	**Units**
Average disk	4290	61.29	$ph\ cm^{-2}s^{-1}arcsec^{-2}$
50 cm telescope	8.42×10^6	0.12×10^6	$ph\ s^{-1}arcsec^{-2}$
System (4.92%)	41.42×10^4	0.59×10^4	$ph\ s^{-1}arcsec^{-2}$
Spatial slit area	99408	1416	$ph\ s^{-1}$
SNR at $1s$	315	38	–

During the maxima phase of SC23, we have considered an average QS flux of 4290 $ph\ cm^{-2}s^{-1}arcsec^{-2}$ at Ne VIII 770 Å obtained from Sarro and Berihuete (2011). The system efficiency, after design optimization of SPOLEO, is 4.92%. With an aperture diameter of 50 cm, the telescope area can be calculated as

$$A_{tel} = \pi\Big(\frac{d_{tel}}{2}\Big)^2 \sim 1963\ cm^2\ . \tag{7.26}$$

The area of the slit is computed as 0.24 $arcsec^2$. Therefore, the total number of Ne VIII photons collected per second per pixel, after passing through the entire system, can be derived as

$$f_{max} = 4290 \times 1963 \times 0.0492 \times 0.24 \sim 99408\ photons\ . \tag{7.27}$$

Assuming the photon count $N = f_{max}$ satisfies the Poisson-statistics condition $\sigma_N \approx \sqrt{N}$, the signal-to-noise ratio (SNR) can be calculated as

$$SNR = \frac{f_{max}}{\sqrt{f_{max}}} \sim 315\ . \tag{7.28}$$

If we perform spatial binning of 133 pixels, resulting in a spatial sampling of 32″/pixel, then we can derive the SNR to be approximately 3632. Evidently, n-pixel spatial binning increases the SNR by a factor of $\sqrt{n}$. Following the same procedure, we can calculate the corresponding SNR during the minima phase of SC23.